University of Leicester

INTERACTIONS BETWEEN FINE PARTICLES

Thesis submitted to the Department of Engineering, University of Leicester for the degree of Doctor of Philosophy

by Fan Li

October 2008

University *of* Leicester

DEPARTMENT OF ENGINEERING

INTERACTIONS BETWEEN FINE

PARTICLES

by

Fan Li

Thesis submitted to the Department of Engineering, University of Leicester
for the degree of Doctor of Philosophy

October 2008

INTERACTIONS BETWEEN FINE PARTICLES

Thesis submitted for the degree of

Doctor of Philosophy

at the University of Leicester

by

Fan Li

Department of Engineering

University of Leicester

October 2008

ABSTRACT

Computer simulation using the Discrete Element Method (DEM) has emerged as a powerful tool in studying the behaviour of particulate systems during powder flow and compaction. Contact law between particles is the most important input to the Discrete Element simulation. However, most of the present simulations employ over-simplistic contact laws which cannot capture the real behaviour of particulate systems. For example, plastic yielding, material brittleness, sophisticated particle geometry, surface roughness, and particle adhesion are all vitally important factors affecting the behaviour of particle interactions, but have been largely ignored in most of the DEM simulations. This is because it is very difficult to consider these factors in an analytical contact law which has been the characteristic approach in DEM simulations. This thesis presents a strategy for obtaining the contact laws numerically and a comprehensive study of all these factors using the numerical approach.

A numerical method, named as the Material Point Method (MPM) in the literature, is selected and shown to be ideal to study the particle interactions. The method is further developed in this work in order to take into account all the factors listed above. For example, to study the brittle failure during particle impact, Weibull's theory is incorporated into the material point method; to study the effect of particle adhesion, inter-atomic forces are borrowed from the Molecular Dynamic model and incorporated into the method. These developments themselves represent a major progress in the numerical technique, enabling the method to be applied to a much wider range of problems. The focus of the thesis is however on the contact laws between extremely fine particles. Using the numerical technique as a tool, the entire existing theoretical framework for particle contact is re-examined. It is shown that, whilst the analytical framework is difficult to capture the real particle behaviour, numerical contact laws should be used in its place.

Key words: contact law; material point method; fine particles; discrete element method

ACKNOWLEDGEMENTS

CONTENTS

LIST OF SYMBOLS

a, a_0, a_1	radii of contact area
a'	radius of contact area where the maximum tensile pressure on the surface applies
a_y	radius of contact area at the onset of plastic deformation, y denotes the onset of plasticity
$\bar{a}$	normalized radius of contact area
$\hat{a}_m$	half length of the longest microcrack
$\bar{\hat{a}}$	average length of all microcracks
$\mathbf{b}$	body force
B	Spatial derivative of shape function N
c	radius of enhanced contact area in Maguis theory, where non-zero adhesive surface traction applies
C_L	longitudinal wave speed
$\mathbf{C}$	constitutive law tensor
D	diameter of a spherical particle
$\mathbf{D}$	rate of deformation tensor
e	coefficient of restitution
$\tilde{e}$	atomistic constant representing the minimum of the Lennard-Jones potential
E	Young's modulus
E^*	effective Young's modulus $E^* = E/(1-v^2)$
$\tilde{E}_0$	initial kinetic energy of a particle
$\mathbf{f}_{L-J}$	Lennard-Jones inter-atomic force vector
$\mathbf{f}_{ij}$	inter-atomic force vector between the ith atom and the jth atom
$\mathbf{f}^{\text{int}}$, $\mathbf{f}^{\text{ext}}$	nodal force vectors
$\tilde{\mathbf{f}}$	total force applied on a material
F	contact force/normal contact force
F^c	critical contact force
F^*	maximum contact force in Hertz theory

F_y contact force at the onset of plastic deformation, y denotes the onset of plasticity

$\bar{F}$ normalized contact force

$\mathbf{F}$ force vector

h gap size between two surfaces

$\hat{h}_{ij}$ vertical distance between the i th atom and the j th atom

H plastic strain hardening parameter

H^1 Hilbert space

i, j, k, l simple indices (indices of coordinate system in FEM and MPM; indices of atoms in MD; indices of particles in DEM)

I index of nodal values

I_{ijkl} index notation for the identity tensor $I_{ijkl} = (1/2)(\hat{\delta}_{ik}\hat{\delta}_{jl} + \hat{\delta}_{il}\hat{\delta}_{jk})$

$\bar{I}$ moment of inertia

$\mathbf{I}$ identity tensor

$j_0(\tilde{x})$, $j_1(\tilde{x})$ spherical Bessel functions of order zero and one

J Jacobian determinant of deformation gradient

K_{IC} fracture toughness of the first kind

m mass scalar

m_I lumped mass matrix or consistent mass matrix, I denotes the nodal index

$\tilde{m}$ Weibull's modulus

$\mathbf{m}$ mass matrix

M_p mass of the p th material point, p denotes material points

$\mathbf{n}$ unit surface normal vector

$\hat{\mathbf{n}}$ unit directional vector in the radial return mapping algorithm

N shape function

Nm total number of atoms

N_p total number of material points, p denotes material points

$p(r)$ pressures on the surface, at an arbitrary radial coordinate r

$\tilde{\mathbf{p}}$ linear momentum of a material body

P_m mean contact pressure

P_0^e, P_0, P_1 the maximum value of a certain kind of pressure distribution on the surface of a particle

$\bar{P}_s$ Weibull's survival possibility

$\mathbf{Q}$ incremental rotation tensor

r radial coordinate

R radius of a spherical particle

$\tilde{R}$ curvature of a curved surface

$\hat{\mathbf{R}}$ radial directional vector of a spherical particle

s, s_{ij} inter-atomic distance; inter-atomic distance connecting the i th atom and the j th atom

$\mathbf{s}$, $\mathbf{s}_{ij}$ inter-atomic vector connecting two atoms; inter-atomic vector connecting the i th atom and the j th atom

t arbitrary time

Δt incremental time; length of time step in numerical time integrations

$\bar{t}$ normalized time

T^* total contact time in Hertz theory

T_0^* normalised total contact time during elastoplastic impact

u unidirectional displacement

$\bar{u}$ normal displacement on the surface

$\mathbf{u}$ displacement vector

U inter-atomic potential function

U_{L-J} inter-atomic potential of the Lennard-Jones type

v unidirectional velocity

$\dot{v}$ unidirectional acceleration, dot denotes time derivative

Δv arbitrary admissible test function

$\mathbf{v}$ velocity vector

$\dot{\mathbf{v}}$ acceleration vector, dot denotes time derivative

V_0 initial normal velocity of a particle

V_y impact velocity required for the onset of plastic deformation, y denotes the onset of plasticity

V_{material} volume of a material body

V_{ref}	standard sample volume in Weibull's law
$\bar{V}_y$	modified velocity related to the maximum contact pressure P_0
$\mathbf{V}$	velocity vector of a particle
$\mathbf{V}_p$	velocity vector of the p th material point
W_{fr}	energy required producing unit length of crack
$\mathbf{W}$	spin tensor
x, y, z	Cartesian coordinate indices
$\mathbf{x}$	vector of any spatial coordinate system
$\mathbf{X}_p$	vector of any spatial coordinate system of the p th material point
Y	unidirectional yield strength (yield stress)
γ	specific surface energy (surface energy per unit area)
δ	particle displacement/normal displacement
δ_y	particle displacement at the onset of plastic deformation, y denotes the onset of plasticity
δ^*	maximum particle displacement in Hertz theory
$\hat{\delta}$	Kronecker delta
$\tilde{\delta}$	Dirac delta function
$\bar{\delta}$	normalized particle displacement
$\boldsymbol{\delta}$	particle displacement vector
$\tilde{\varepsilon}$	unidirectional strain
ε^*	crack length parameter
ε_0	equilibrium inter-atomic distance
ε	zero adhesion force distance between two contacting surfaces
ε_1	zero adhesion force distance between two contacting infinite planar surfaces
$\boldsymbol{\varepsilon}$	strain tensor
$\dot{\boldsymbol{\varepsilon}}$	strain rate tensor, dot denotes time derivative
λ	Lamé constant
$\bar{\lambda}$	Maugis parameter
μ	Lamé constant
$\bar{\mu}$	Tabor's parameter

v	Poisson's ratio
κ	energy dissipation measurement
$\Delta\theta$	incremental rotation
ω	angular velocity
$\dot{\omega}$	angular acceleration, dot denotes time derivative
$\omega^{\text{vibration}}$	angular frequency during free vibration
ρ	density scalar
σ_0	a representative value of adhesive surface traction
σ_a	adhesive surface traction (normal direction)
$\tilde{\sigma}$	unidirectional stress
$\sigma_{[TS]}$	tensile strength
$\sigma_{[C]}$	compressive strength
σ_{ref}	standard unidirectional stress in Weibull's theory
$\boldsymbol{\sigma}$	Cauchy stress vector
$\dot{\boldsymbol{\sigma}}$	stress rate tensor
$\boldsymbol{\sigma}^{\nabla J}$	Jaumann stress rate
τ	unidirectional surface traction
$\boldsymbol{\tau}$	surface traction vector
ζ	a random value representing the strength variability of brittle materials
Γ	surface of a material body
Γ_C	contact boundary
Ω	domain of a material body

LIST OF FIGURES

LIST OF TABLES

CHAPTER 1

INTRODUCTION

The theme of this thesis is to study the interaction between extremely fine particles using modern numerical techniques. This chapter provides the general background of the problem and outlines the existing theories which are relevant to this study.

1.1 PARTICULATE SYSTEMS

Fine particles, other than defined in physics as dots with degrees-of-freedom, merely holding space and positions, are practically of many complicated features. The behaviour of particles is relevant to modern chemical/drug/powder-metallurgy industries. These industries have to work with various kinds of properties of their particles. For example, the industry of powder-metallurgy is an area that the properties of particles play an important role (e.g. Rajiv *et al*., 2006). The technique of powder-metallurgy is to convert an assembly of particles, i.e. powders into an integrated component with desired shape. This technique is now used extensively in the fabrication of ceramic and metal parts. Concisely speaking, there are several processing steps to convert powders into a solid part, including powder production, transfer, mixing, compaction, sintering, and etc. All these processing steps are utilizing the properties of particles. Specifically, the powders can be produced from either solidification of melted materials or milling of cold materials, where large particles are crushed into finer particles. During powder transfer and mixing, the flowability of particles makes it easy to control the shape and properties of the parts. Compared to conventional fabrication methods such as machining or casting, this appealing flowability of powders enables complex part shapes with less waste of materials. The particles are deformed under external pressure during the compaction process. The deformations of individual particles create stresses inside while the particulate systems can be densified. One of the most appealing features of the

powder-metallurgy is that, due to the extremely large surface area of the powders, the particles can be bonded together into a whole component by solid state diffusions between particles at temperatures far below the melting temperature. This sintering process enables the manufacture of parts from difficult-to-melt materials. Other examples of properties of particles include, electrostatic controllable, such as in the depositing of carbon powders in the printing and photocopying industry; the ability of forming liquid dispersion such as colloid production in the industry of pastes and gels.

Generally speaking, most people who are dealing with particles are actually dealing with a whole particulate system. Normally formed by highly self-similar individual particles with various properties, one whole particulate system behaves either discretely (e.g. particle flow) or continuously (e.g. compacted powders). It is important to control the final output of the processing of the particulate systems (e.g. the quality of the parts after sintering). However, a whole particulate system can be so complex that the desired output is sometimes hard to obtain. For example, some well known problems in the metallurgy industry include the geometry inaccuracy and shape distortion, the density inhomogeneity, and the inter-particle cracking or inner-particle cracking when subjected to excessive external force. In order to solve such problems and improve the final output of the product, a full understanding of the particulate systems is an essential requirement. In fact, in the recent years, the demand for the modelling of the particulate systems has been increasing intensively.

Unfortunately, one whole particulate system is too complicate to model by conventional methods. On the one hand, an entire particulate system is able to flow freely, therefore cannot be treated as a continuous solid. On the other hand, the particulate system consists of individual deformable particles, which have to be treated as continuous solids. A multi-scale approach has been used with the help by the expanding use of modern computers and numerical techniques. Firstly, the properties of an individual particle are comprehensively modelled. Secondly, all particles of a particulate system are abstracted into space occupying dots with the dominant property. The whole particulate system is simulated by governing the

particles with the interaction rules obtained in the first step. In the past decades, the Discrete Element Method (DEM) has been used to simulate the particulate systems. First applied by Cundall (1971) to study granular materials such as rock, the DEM is becoming more and more popular in geophysics. Recently, the DEM is proved to be useful in simulating the other particulate systems, especially for the particle flow (e.g. Sitharam, 2000). The main idea of DEM is to assume that the interaction between two particles is the dominant mechanism in a particulate system. The particle motion can be simulated by solving the equations of motion based on the knowledge of the interactions between a single pair of particles.

1.2 THE DISCRETE ELEMENT METHOD

In the Discrete Element Method (DEM), typically, all particles in the particulate system are simplified to be identical spheres (space occupying dots). An example of two dimensional DEM is shown in Fig. 1.1(a). Two particles only interact when they are in contact. When two particles are in contact and further approach each other, they are allowed to have overlapping, the thickness of which is equal to the relative displacement between the two particles. In DEM, the force acting on the i th particle $\mathbf{F}_i$ is determined completely by the relative displacement between the two particles $\boldsymbol{\delta}_{ij}$ such that

$$\mathbf{F}_i = \sum_{j \neq i} \mathbf{F}_{ij}(\boldsymbol{\delta}_{ij}) \,, \tag{1.1}$$

where j denotes the j th particle. The motions of the particles at time t are obtained by solving the equations of motion:

$$m_i \dot{\mathbf{v}}_i = \mathbf{F}_i \,, \tag{1.2}$$

$$\mathbf{v}_i^{t+\Delta t} = \mathbf{v}_i^t + \dot{\mathbf{v}}_i \Delta t \,, \tag{1.3}$$

and

$$\boldsymbol{\delta}_i^{t+\Delta t} = \boldsymbol{\delta}_i^t + \mathbf{v}_i^{t+\Delta t}\Delta t \,, \tag{1.4}$$

where m_i is the mass of the i th particle, Δt is the length of a short time interval (incremental time), $\dot{\mathbf{v}}_i$, $\mathbf{v}_i$, and $\boldsymbol{\delta}_i$ are the acceleration, velocity, displacement of the i th particle respectively. We use the notation that the bold letters denote vectors or tensors, and dot denotes the time derivative. The displacement, velocity, acceleration and force are written in bold because they are vectors consisting of a normal component and a tangential component that
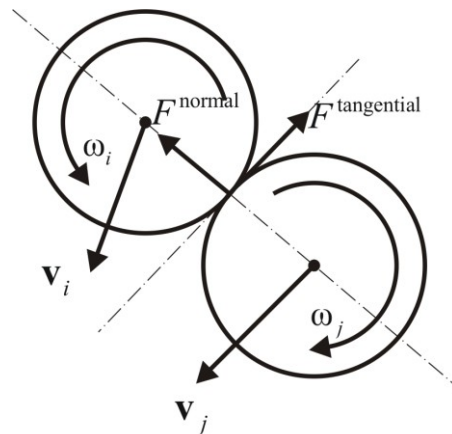
(a)
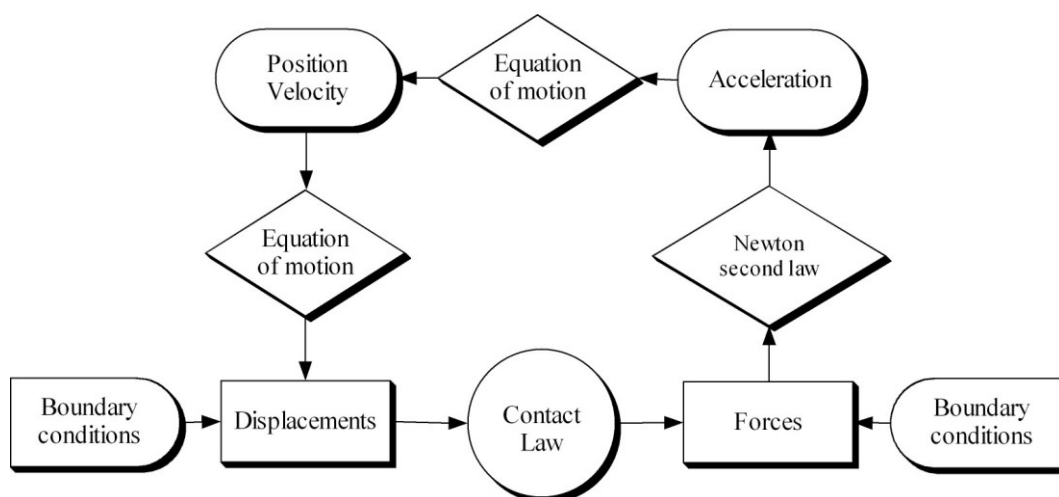
(b)

Fig. 1.1 DEM simulations. (a) Illustration of a typical DEM particle pairs. (b) Typical numerical scheme of a DEM simulation.

$$\boldsymbol{\delta} = \begin{bmatrix} \delta^{\text{normal}} \\ \delta^{\text{tangential}} \end{bmatrix}, \ \mathbf{v} = \begin{bmatrix} v^{\text{normal}} \\ v^{\text{tangential}} \end{bmatrix}, \ \dot{\mathbf{v}} = \begin{bmatrix} \dot{v}^{\text{normal}} \\ \dot{v}^{\text{tangential}} \end{bmatrix}, \ \text{and} \ \mathbf{F} = \begin{bmatrix} F^{\text{normal}} \\ F^{\text{tangential}} \end{bmatrix}. \tag{1.5}$$

If rotation is considered in DEM, a set of equations of motion similar to Eqs. (1.2)-(1.4) can be obtained such that

$$\dot{\omega}_i = \frac{F_i^{\text{tangential}} \cdot R}{\overline{I}_i}, \tag{1.6}$$

$$\omega_i^{t+\Delta t} = \omega_i^t + \dot{\omega}_i \Delta t, \tag{1.7}$$

$$\Delta \theta_i^{t+\Delta t} = \omega_i^{t+\Delta t} \Delta t. \tag{1.8}$$

A modification to Eq. (1.1) is needed such that

$$F_i^{\text{normal}} = \sum_{j \neq i} F_{ij}^{\text{normal}}(\boldsymbol{\delta}_{ij}), \tag{1.9}$$

$$F_i^{\text{tangential}} = \sum_{j \neq i} F_{ij}^{\text{tangential}}(\boldsymbol{\delta}_{ij}, \Delta \theta_i). \tag{1.10}$$

In Eqs. (1.6)-(1.8) $\overline{I}_i$ is the moment of the inertia of the particle, $\dot{\omega}_i$, ω_i, and $\Delta \theta_i$ are the angular acceleration, angular velocity, and the incremental rotation respectively. Obtaining the acceleration $\dot{\mathbf{v}}_i$ and $\dot{\omega}_i$ will produce further updating of the relative displacement $\boldsymbol{\delta}_i$ and incremental rotation $\Delta \theta_i$. By iterating Eqs. (1.1)-(1.4), and Eqs. (1.6)-(1.10) on all particles in a particulate system, the movements of all particles are obtained . The typical numerical scheme of a DEM simulation is shown in Fig. 1.1(b).

1.3 CONTACT BETWEEN A PAIR OF PARTICLES

Equation (1.1), or more rigorously speaking, Eqs. (1.9) and (1.10), are known as the contact law, where Eq. (1.9) is normally regarded as the normal contact law while Eq. (1.10) is normally regarded as the tangential contact law. Figure 1.1(b) clearly shows that the contact law is the core of the DEM simulation. The accuracy of the contact law will determine the accuracy of the whole DEM solutions.

A contact law is a relationship between the contact force $\mathbf{F}$ and relative displacement $\boldsymbol{\delta}$ between two particles. The normal contact law is of the most interest because: (a) the tangential contact law can be related to the normal contact law; (b) the normal contact law varies a lot from one kind of particle to another. Throughout this thesis, we are focusing on the normal contact law and therefore do not distinguish F from F^{normal}, and δ from δ^{normal}.

Contact mechanics, such as the method developed by Hertz in the 1881 (see Johnson, 1985 for example), has provided a natural analytical framework for obtaining the contact laws. As shown in Fig. 1.2, in the analyses of contact mechanics, a particle is generally assumed to be a sphere with a radius R. The contact between a pair of identical particles can be simplified as a spherical particle contacting against a rigid wall. According to the Hertz theory, the spherical particle is assumed to be completely elastic, with a Young's modulus E and a Poisson's ratio v. The deformation of the particle is small therefore the profile of the particle near the contact area can be simplified to be a parabolic function such that

$$\delta = \frac{a^2}{R},$$ (1.11)

where a is the radius of the contact area δ is the approach displacement in the normal direction of the contact.

As shown in Fig. 1.2, the normal displacement $\bar{u}_z$ at an arbitrary position r within the contact area must follow the constraint that

$$\bar{u}_z = \delta - r^2/R .$$ (1.12)

An important finding by Hertz is that the pressure distribution within the contact area follows

$$p_{\text{Hertz}} = P_0^e \left[1 - (r/a)^2 \right]^{1/2},$$ (1.13)

which satisfies Eq. (1.12). P_0^e is the value of the elastic pressure at the centre of the contact area. The normal displacement at an arbitrary position within the contact area can be obtained from Eq. (1.13) using the elastic theory for half space as
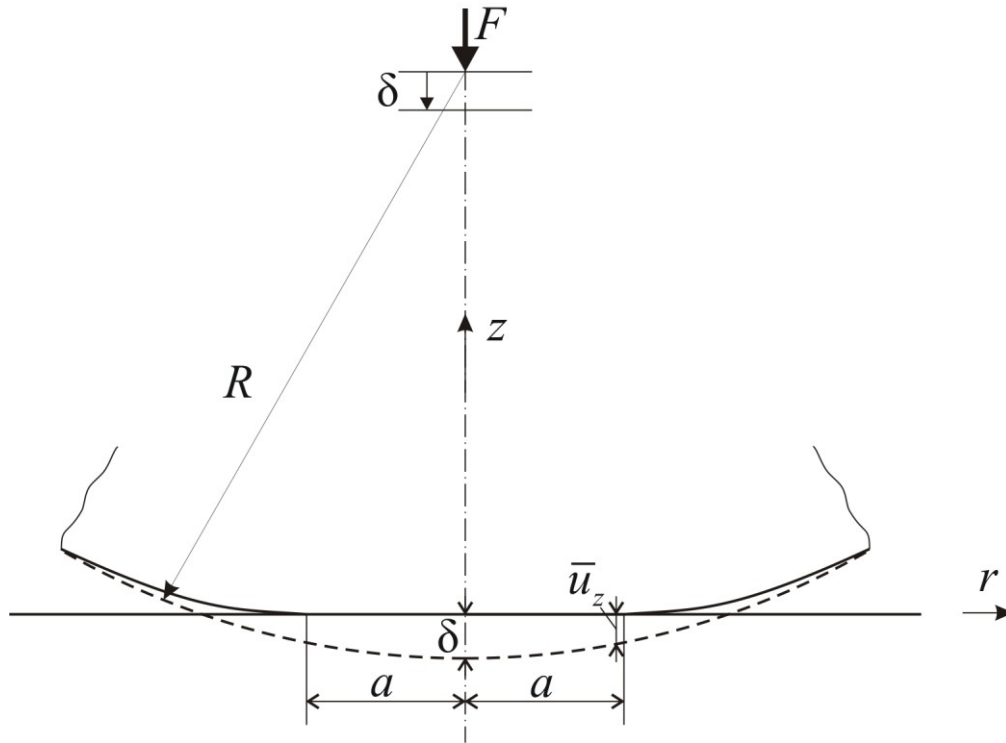
Fig. 1.2 A spherical particle contacting with the rigid wall, the Hertz theory.

$$\bar{u}_z = \frac{\pi P_0^e}{4aE^*}(2a^2 - r^2) = \delta - r^2 / R, \tag{1.14}$$

where E^* is the effective elastic modulus that

$$E^* = E /(1 - v^2). \tag{1.15}$$

By letting $r = 0$ in Eq. (1.14) and using Eq. (1.11), the radius of the contact area can be solved as

$$a = \pi P_0^e R / 2E^* .$$ (1.16)

On the other hand, the contact force is the integration of the pressure over the contact area given by

$$F_{\text{Hertz}} = \int_0^a p(r) 2\pi r dr = \frac{2}{3} P_0^e \pi a^2 .$$ (1.17)

The contact force can be therefore obtained by eliminating P_0^e from Eq. (1.16) and Eq. (1.17) as that

$$F_{\text{Hertz}} = \frac{4a^3 E^*}{3R} .$$ (1.18)

By eliminating the radius of the contact area a from Eq. (1.11) and Eq. (1.18), the Hertz contact law is obtained as

$$F_{\text{Hertz}} = \frac{4}{3} E^* \delta^{2/3} R^{1/2} .$$ (1.19)

Most of the current DEM solutions use Hertz theory. However the over-simplified contact law is potentially inadequate when plasticity, large deformation, material heterogeneity or non-spherical geometry is involved. These situations are quite common in practical particulate systems. Extensive research and discussions of such issues are presented in CHAPTER 3.

There are also other kinds of interactions between particles besides the contact mechanics. For example, brittle particles tend to fail rather than deform; small, smooth particles tend to stick together by tensile force. In order to simulate the particulate systems accurately, interactions between particles have to be considered as accurately as possible. Two important interactions between a pair of particles will be introduced in the next section.

1.4 PARTICLE INTERACTIONS BESIDES CONTACT LAWS

1.4.1 The failure of brittle particles

Many practical particulate systems are consisted of brittle particles. For example, one field in which the DEM has been applied frequently is the processing of rock and minerals, which are rather brittle materials. Furthermore brittle powders, such as glass and ceramic powders are widely used in material and chemical processing. Although the above powder materials have various different material properties, they share a common feature, which is the relative low fracture toughness of these brittle powders. This important feature affects, sometimes controls, the processing of the powders. Therefore, the failure behaviour is an important property for brittle particles. When simulating the behaviour of particulate systems, it is important to bear in mind that the particles may break even when the deformation is still small.

Stress analyses are required in dealing with brittle failures. Classical fracture mechanics always assumes that there exist microcracks in, or on the surface of, brittle materials. As shown in Fig. 1.3, the crack tips are where the stress field is singular and further crack growth occurs. It is well known that, the crack generation and growth require energy in forming new surfaces. In metals, large amount of energy is also absorbed by plastic deformation and it is difficult for a crack to grow. However, in brittle materials, there are very few mechanisms to stop the cracks from growing, leading to low fracture toughness. It was illustrated by Ashby and Jones (1986) that the main mechanism of causing brittle failure is the tensile stress. As shown in Fig. 1.3(a), under a tensile stress, a crack can propagate unstably and the tensile strength of a brittle material depends on the length of the longest microcrack such that

$$\sigma_{[TS]} = \frac{K_{IC}}{\sqrt{\pi \hat{a}_m}} \quad , \tag{1.20}$$

where K_{IC} is the fracture toughness and $\hat{a}_m$ is the half length of the longest microcrack. In contrast, as shown Fig. 1.3(b), under compression, the cracks will propagate in a stable manner and the compressive strength is given by

$$\sigma_{[C]} = [C]\frac{K_{IC}}{\sqrt{\pi\bar{\bar{a}}}},$$ (1.21)

where $[C]$ is a constant of about 15, and $\bar{\bar{a}}$ is the average length of the microcracks. Obviously, the compressive strength given by Eq. (1.21) is much larger than the tensile strength given by Eq. (1.20). In a particulate system, no particle is in a uniform stress state. The tensile stress inside a particle is believed to be the dominant cause of its brittle failure.

(a)

(b)
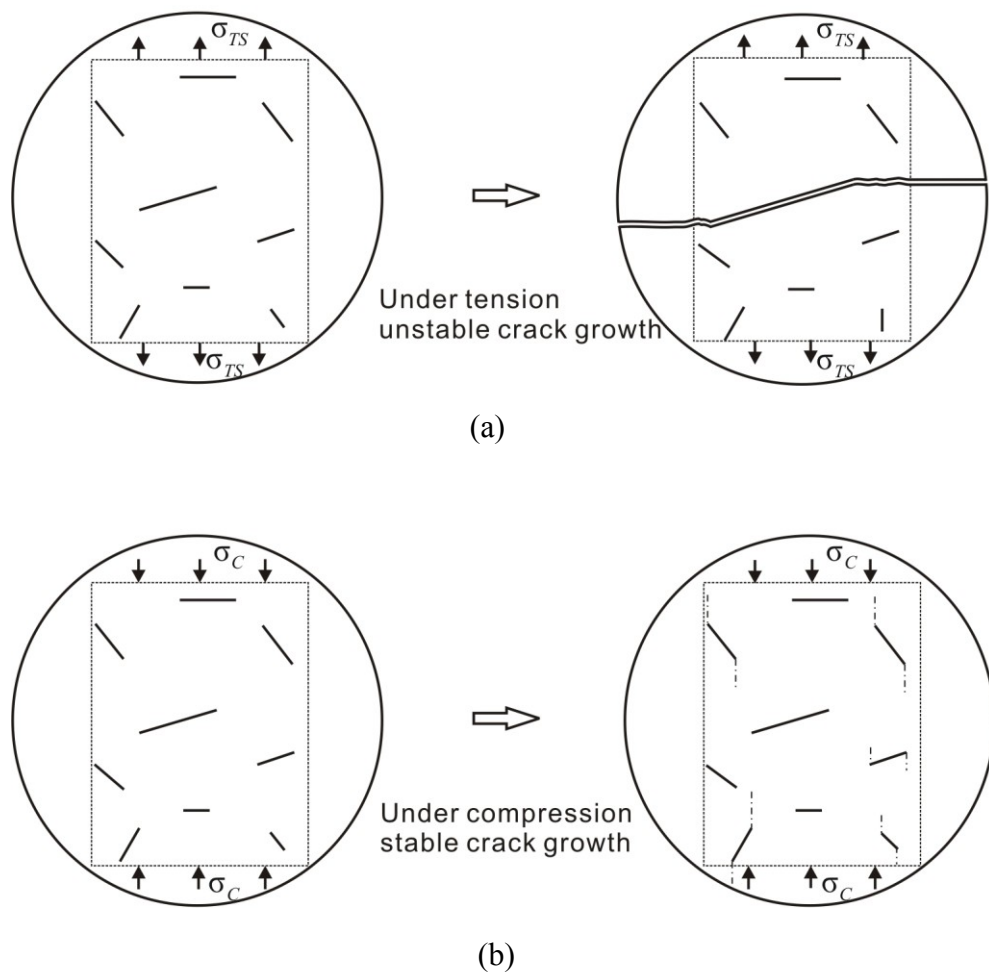
Fig. 1.3 The growth of microcrack inside a particle under uniform stress state. (a) In tensile stress the largest microcrack grows unstably. (b) In compressive stress, many microcracks propagate stably.

Another important issue due to the existing of microcracks is the strength variability of brittle particles. The microcracks are randomly distributed inside a brittle material. For example, comparing two spherical particles of the same volume and made of the same material, the first particle may contain a larger microcrack than the second one does. Due to Eq. (1.20), the first particle is therefore relatively easier to break and of lower strength. Generally, the strength varies significantly between individual particles, and different places in a single particle. This variability is often represented by a statistic strength model, such as Weibull's law (e.g. Ashby and Jones, 1986), which is described below.

Given a number of samples of the same standard volume V_{ref}, of the same brittle material, no sample will fail under zero stress. As the stress level increases, more and more samples fail and the survival probability of a standard volume sample is given by

$$\bar{P}_s(V_{\mathrm{ref}}) = \exp\left\{-\left(\frac{\sigma}{\sigma_{\mathrm{ref}}}\right)^{\tilde{m}}\right\}, \tag{1.22}$$

where σ is the uniaxial applied stress, σ_{ref} is a reference stress at $\bar{P}_s(V_{\mathrm{ref}}) = \exp[-1]$, and $\tilde{m}$ is referred to as the Weibull's modulus. As shown in Fig. 1.4, the Weibull's modulus $\tilde{m}$ reflects how rapidly the survival probability decreases as the applied stress increases.

Statistically, if a specimen has a larger volume, it is more likely for the specimen to contain a larger microcrack. Given the fact that a large specimen can be regarded as an assembly of several small specimens, the survival probability of a large material body can be calculated as

$$\bar{P}_s(V_{\mathrm{material}}) = (\bar{P}_s(V_{\mathrm{ref}}))^{V_{\mathrm{material}}/V_{\mathrm{ref}}}. \tag{1.23}$$
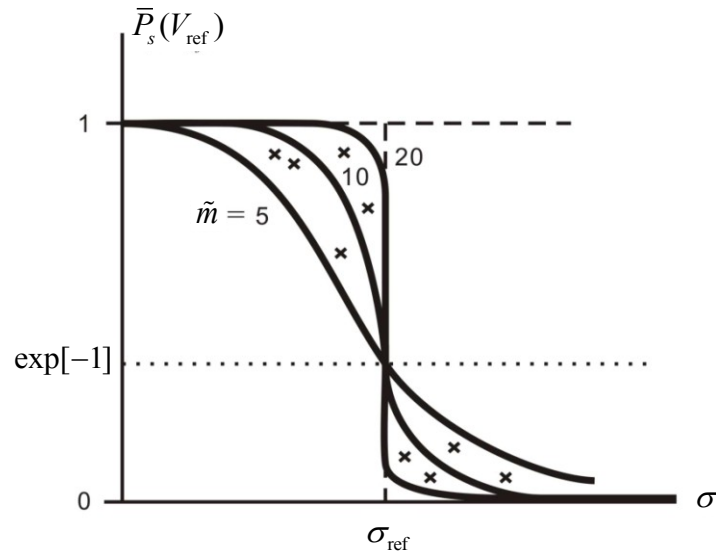
Fig. 1.4 The Weibull's distribution, the survival probability for different Weibull's modulus $\tilde{m}$.

in which V_{material} is the volume of the large material body. The Weibull's statistic law is very useful and will be implemented to model the strength variability of brittle particles in CHAPTER 4.

1.4.2 Adhesion between particles

It is well known that the flowability of a particulate system decreases significantly as the size of the particles gets smaller. The particles can become so 'sticky' that it is very difficult to separate them. The force which adheres particles together is referred to as the adhesion force. The adhesion force is an integration of adhesive surface traction, defined as adhesion force per unit area. The adhesion force arises from the surface energy released by the disappearing of the surface as two particles form a contact neck between them. The energy per unit area that can be released by a material surface is generally called specific surface energy. Particle adhesion has already been studied for decades. In the final years of the last century when the Atom Force Microscope (AFM) first became available (e.g. Kendall, 2001), the ability of

measuring the local properties of materials triggered further interest in the adhesive contact between solids. It is now well accepted that the surface energy is generated by the potential energy of atoms near the surface of a material. As shown in Fig. 1.5, the famous Lennard-Jones (L-J) potential (e.g. Rapaport, 1995) is a typical potential between atoms. In the L-J potential, atoms are simplified to be mechanical dots with mass. The L-J potential is believed to act between each pair of atoms and depend only on the distance between the two atoms such that

$$U_{L-J}(s) = 4\tilde{e}\left[\left(\frac{\varepsilon_0}{s}\right)^{12} - \left(\frac{\varepsilon_0}{s}\right)^6\right],\tag{1.24}$$

where ε_0 is the distance when the L-J potential is zero, s is the distance between two atoms, and $\tilde{e}$ is a constant representing the minimum of the potential well. The inter-atomic force is the distance derivative of the inter-atomic potential given by

$$\mathbf{f}_{L-J}(s) = \frac{48\tilde{e}}{\varepsilon_0^2}\left[\left(\frac{\varepsilon_0}{s}\right)^{14} - \frac{1}{2}\left(\frac{\varepsilon_0}{s}\right)^8\right]\mathbf{s}.\tag{1.25}$$

where $\mathbf{s}$ is the vector connecting the two atoms under consideration.
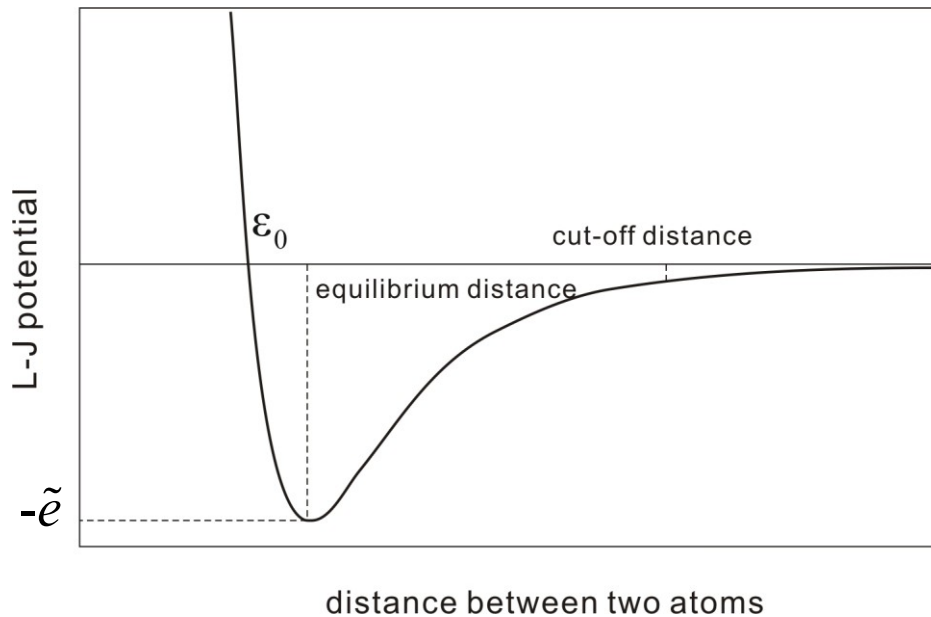
Fig. 1.5 Lennard-Jones potential depending on the distance between two atoms.

As one can see from Fig. 1.5, The equilibrium inter-atomic distance is the distance when the L-J potential reaches its minimum $-\tilde{e}$, i.e. when $s = 2^{1/6}\varepsilon_0$. If the distance between two atoms is equal to the equilibrium distance, the force between the two atoms is zero. If the inter-atomic distance is larger than the equilibrium distance, the inter-atomic force is negative, indicating that there is a force between two atoms which draws the two atoms close. If the distance between two atoms is smaller than the equilibrium distance, the inter-atomic force is positive, which means there is a strong repulsion between atoms preventing the two atoms to approach each other. A cut-off distance of the L-J potential is usually used. If the distance between the atoms is larger than the cut-off distance, the inter-atomic potential is very small and ignorable. A typical cut-off distance value is $2.5\varepsilon_0$. The inter-atomic potential will be discussed extensively in CHAPTER 5.

As early as in the 1930s, Bradley (1932) published his understanding about the adhesion between rigid spherical particles. Bradley (1932) assumed that the adhesion force always tries to pull two surfaces together to an equilibrium position. Similar to Eq. (1.11) the profile of the particle is assumed to be parabolic. For a particle of radius R, the gap between a particle and a rigid wall in Fig. 1.6 can be represented by

$$h = \frac{r^2}{R} \ .$$
(1.26)

where r is the same with that used in Eq. (1.12), i.e. radial distance in the contact plane. The adhesive surface traction σ_a is assumed to depend on the distance between the two contacting surfaces (generally decreasing as the distance increases), i.e. we have

$$\sigma_a = \sigma_a(h) \ .$$
(1.27)

Regarding to the surface energy when studying the contact between two identical particles, a simplification can be always made. Since the contact between two identical particles can be represented by the contact between one particle and a rigid

wall, the rigid wall is assumed to have zero surface energy, and the interface energy between the particle and the rigid wall is also assumed to be zero.

When a rigid particle comes into contact with a rigid wall as shown in Fig. 1.6, the specific surface energy γ is assumed to be a material constant which is the integration of the adhesive surface traction over the gap

$$\gamma = \int_0^\infty \sigma_a(h)dh \,. \tag{1.28}$$
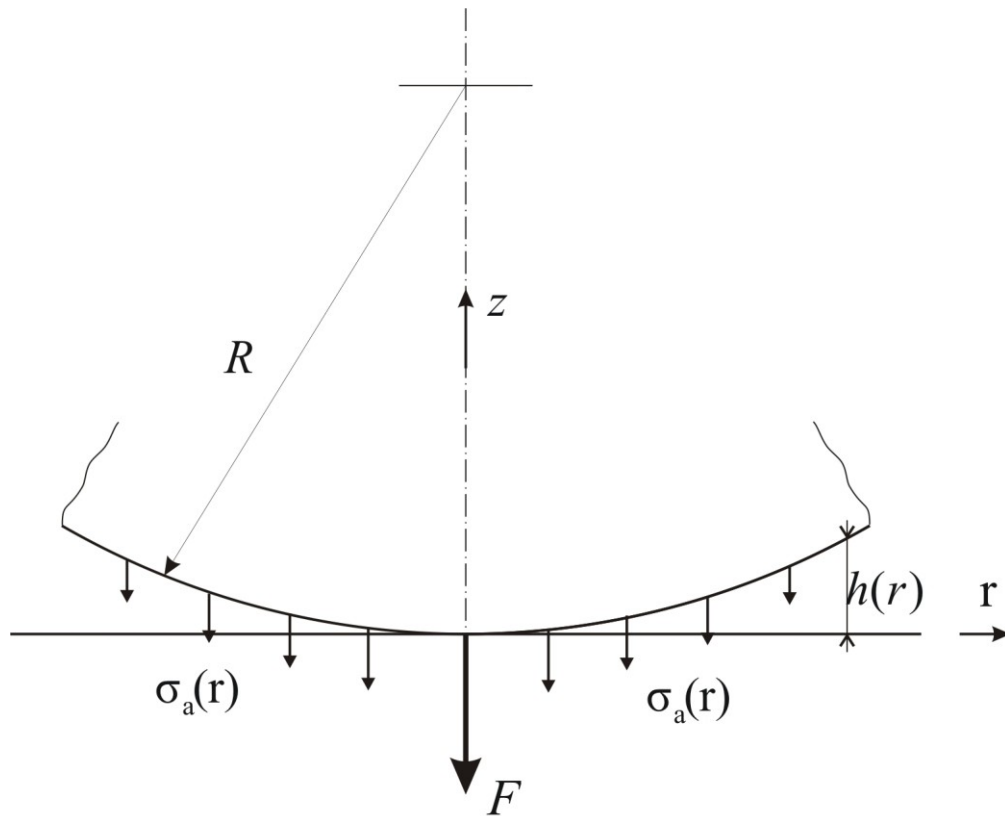
Fig. 1.6 The illustration of the effect of adhesion and the solution of adhesion force.

The total adhesion force is the integration of the adhesive surface traction over the whole surface area such that

$$F_{\text{Bradley}} = \int_0^R 2\pi r \sigma_a(h)dr \,. \tag{1.29}$$

By using Eqs. (1.26) and (1.28) in Eq (1.29) and noticing that $(R-h)dh = rdr$ and $h \ll R$, we have

$$F_{\text{Bradley}} = \int_0^R 2\pi r \sigma_a(h)dr = 2\int_0^\infty \pi R \sigma_a(h)dh = 2\pi R\gamma .$$ (1.30)

Bradley (1932) assumed the particle is rigid and therefore the adhesion force can be obtained in the straightforward manner. The problem becomes more complicated if the mechanical properties of the solid particles are taken into account. For example, nano-sized particles may deform remarkably by the adhesion force during contact. Many theories about elastic adhesive contact between spherical particles have been proposed. The simplest theory was the one proposed by Derjaguin *et al.* (1975), known as the DMT theory. A strong assumption in the DMT theory is that the surface energy does not affect the elastic deformation of the contacting particles so that the Hertz contact force and the Bradley adhesion force are simply added together to give

$$F_{\text{DMT}} = F_{\text{Hertz}} - 2\pi\gamma R$$ (1.31)

As one can see from Eq. (1.31), the DMT theory predicts a maximum tensile force when the particle is just at the point contact. The maximum tensile force is regarded as the pull-off force, representing the force required to separate the particle from the rigid wall which is given by

$$F_{\text{DMT}}^c = -2\pi\gamma R .$$ (1.32)

The particle deformation follows the solution of Hertz theory given by Eq. (1.19). Therefore, the adhesion interaction can be combined with the contact mechanics to represent the relationship between the force and the displacement. The adhesive interaction between deformable particles can be also identified as contact law and referred to as adhesive contact law between particles. One problem about the relative displacement between particles arises if the adhesion is taken into account. For contact mechanics neglecting adhesion, the relative displacement is the approaching distance between the centre of the particle and the wall, which is equal to the

compressive deformation of the particle in the normal direction to the contact. If adhesion is taken into account, the tensile force firstly attracts the particle when it comes into the cut-off distance. The approaching distance between the centre of the particle and the wall is no longer equal to the compressive deformation because the deformation of the particle can be elongation (negative compression) due to the tensile adhesion force between the particle and the wall. In this thesis, we follow the convention that the compressive deformation of a particle is used as relative displacement because it is more analytically explicit.

One important conclusion may be drawn if we compare the adhesion force given by Eq. (1.32) with the elastic contact force given by Eq. (1.19). The mechanical force F_{Hertz} is proportional to the square of the particle size, R^2, while the force required to separate the particle, F_{DMT}^c, is proportional to the particle size, R. A size effect can be expected since the two forces vary differently with the particle size. One may also expect that the effect of surface energy becomes more significant as the particle size decreases. The size effect is an important issue when simulating the behaviour of particulate systems. More details about the size effect as well as the effect of other factors like the surface roughness and the mechanical properties on the adhesive contact law are discussed in CHAPTER 5.

1.5 NUMERICAL APPROACH TO THE PARTICLE INTERACTIONS

1.5.1 Continuum approach 一 the Finite Element Method (FEM)

To simulate a particulate system efficiently, the Discrete Element Method (DEM) prefers to use analytical contact laws, with the form of Eq. (1.19). As the demand for accuracy in the simulation is increasing, more and more DEMs are able to readily implement a numerical contact law, i.e. the force-displacement curve, as their input. The Finite Element Method (FEM) is usually used as an accurate and robust tool to solve the problem of particle interactions (e.g. Belytschko *et al*., 2000). The FEM is a numerical technique for finding approximate solutions of partial differential equations

(PDE). Since the particle impact is a dynamic process, the PDE describing the deformation of the material can be derived as following. As shown in Fig. 1.7, a material body with the initial domain Ω_0, boundary Γ_0, initial position $\mathbf{x}_0$, initial velocity $\mathbf{v}_0$, deforms with the displacement field $\mathbf{u}$. At any time t, a material body occupies a domain Ω with a surface area Γ. The total force applied on the material is given by
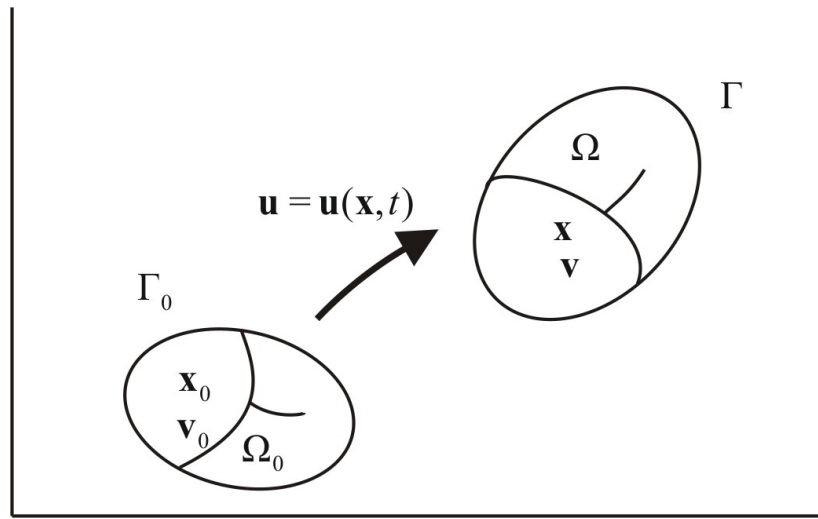
Fig. 1.7 Configurations of a deformed material body. The domain of the material body is Ω, with boundary Γ, position $\mathbf{x}$ and velocity $\mathbf{v}$ at an arbitrary time instant.

$$\tilde{\mathbf{f}}(t) = \int_\Omega \rho \mathbf{b}(\mathbf{x},t)d\Omega + \int_\Gamma \boldsymbol{\tau}(\mathbf{x},t)d\Gamma, \tag{1.33}$$

where $\tilde{\mathbf{f}}$ is the force, ρ is the density, $\mathbf{b}$ is the body force, $\mathbf{x}$ is the position representing any point in the material, and $\boldsymbol{\tau}$ is the surface traction. The linear momentum of the material body $\tilde{\mathbf{p}}(t)$ can be represented by the velocity of the material $\mathbf{v}(\mathbf{x},t)$ through

$$\tilde{\mathbf{p}}(t) = \int_\Omega \rho \mathbf{v}(\mathbf{x},t)d\Omega. \tag{1.34}$$

By momentum conservation, we have

$$\frac{d\tilde{\mathbf{p}}}{dt} = \tilde{\mathbf{f}} \Rightarrow \frac{d}{dt}\int_{\Omega}\rho\mathbf{v}(\mathbf{x},t)d\Omega = \int_{\Omega}\rho\mathbf{b}(\mathbf{x},t)d\Omega + \int_{\Gamma}\boldsymbol{\tau}(\mathbf{x},t)d\Gamma \ . \tag{1.35}$$

Using the material time derivative (Reynold's theorem, see APPENDIX I), the time derivative in Eq. (1.35) is

$$\frac{d}{dt}\int_{\Omega}\rho\mathbf{v}(\mathbf{x},t)d\Omega = \int_{\Omega}\left(\frac{d(\rho\mathbf{v}(\mathbf{x},t))}{dt} + \rho\mathbf{v}(\mathbf{x},t)\nabla\cdot(\mathbf{v}(\mathbf{x},t))\right)d\Omega$$

$$= \int_{\Omega}\left[\rho\frac{d(\mathbf{v}(\mathbf{x},t))}{dt} + \mathbf{v}(\mathbf{x},t)\left(\frac{d\rho}{dt} + \rho\nabla\cdot(\mathbf{v}(\mathbf{x},t))\right)\right]d\Omega , \tag{1.36}$$

in which

$$\frac{d\rho}{dt} + \rho\nabla\cdot(\mathbf{v}(\mathbf{x},t)) = 0 \tag{1.37}$$

is a statement of mass conservation. From Eqs. (1.35)-(1.37), we obtain

$$\int_{\Omega}\rho\mathbf{b}(\mathbf{x},t)d\Omega + \int_{\Gamma}\boldsymbol{\tau}(\mathbf{x},t)d\Gamma = \int_{\Omega}\rho\frac{d(\mathbf{v}(\mathbf{x},t))}{dt}d\Omega \ . \tag{1.38}$$

The gauss theorem dictates that

$$\int_{\Gamma}\boldsymbol{\tau}d\Gamma = \int_{\Gamma}\mathbf{n}\cdot\boldsymbol{\sigma}d\Gamma = \int_{\Omega}\nabla\cdot\boldsymbol{\sigma}d\Omega \tag{1.39}$$

where $\boldsymbol{\sigma}$ is the Cauchy stress tensor and $\mathbf{n}$ is the unit surface normal. Equation (1.38) then becomes

$$\int_{\Omega}\rho\mathbf{b}(\mathbf{x},t)d\Omega + \int_{\Omega}\nabla\cdot\boldsymbol{\sigma}(\mathbf{x},t)d\Omega = \int_{\Omega}\rho\frac{d(\mathbf{v}(\mathbf{x},t))}{dt}d\Omega \tag{1.40}$$

or

$$\rho\mathbf{b} + \nabla\cdot\boldsymbol{\sigma} = \rho\dot{\mathbf{v}} , \tag{1.41}$$

Equation (1.39) is subject to the boundary condition that

$$\mathbf{n} \cdot \boldsymbol{\sigma}(\mathbf{x}, t) = \boldsymbol{\tau}(\mathbf{x}, t), \text{ on } \Gamma. \tag{1.42}$$

Equation (1.41) cannot be conveniently solved numerically since it requires spatial derivative of the stress field, and is normally referred to as the strong form. A weak form can be obtained using the virtual power principle. Given a displacement admissible virtual velocity $\Delta \mathbf{v}$ in an admissible space

$$\Delta v_i(\mathbf{x}) \in \Psi_0, \quad \Psi_0 = \left\{ \Delta v_i \mid \Delta v_i \in H^1(\Omega), \ \Delta v_i = 0 \text{ on } \Gamma \right\}. \tag{1.43}$$

$H^1(\Omega)$ denotes the Hilbert space of functions being square integrable with their derivatives. The strong form (Eq. (1.41)) becomes

$$\int_\Omega \Delta \mathbf{v}(\rho \mathbf{b} + \nabla \cdot \boldsymbol{\sigma} - \rho \dot{\mathbf{v}}) d\Omega = 0 \tag{1.44}$$

or

$$\int_\Omega \Delta v_i \frac{\partial \sigma_{ji}}{\partial x_j} d\Omega = \int_\Omega (-\Delta v_i \rho b_i + \Delta v_i \rho \dot{v}_i) d\Omega, \tag{1.45}$$

where i, j denote the components of the vectors. Although i, j also denote the indices of the particles in section 1.1, there is no need to distinguish them since the physical meaning is rather clear. The left hand side of Eq. (1.45) can be rewritten as

$$\int_\Omega \Delta v_i \frac{\partial \sigma_{ji}}{\partial x_j} d\Omega = \int_\Omega \left[\frac{\partial}{\partial x_j} (\Delta v_i \sigma_{ji}) \right] d\Omega - \int_\Omega \left(\frac{\partial \Delta v_i}{\partial x_j} \sigma_{ji} \right) d\Omega. \tag{1.46}$$

By applying the Gauss theorem on the first term of the right hand side of Eq. (1.46), we obtain

$$\int_\Omega \Delta v_i \frac{\partial \sigma_{ji}}{\partial x_j} d\Omega = \int_\Gamma \Delta v_i \tau_i d\Gamma - \int_\Omega \left(\frac{\partial \Delta v_i}{\partial x_j} \sigma_{ji} \right) d\Omega. \tag{1.47}$$

Substitute Eq. (1.47) into Eq. (1.45), the weak form of the governing equation is obtained:

$$\int_{\Omega}\left(\frac{\partial\Delta v_i}{\partial x_j}\sigma_{ji}\right)d\Omega - \int_{\Gamma}\Delta v_i\tau_i d\Gamma - \int_{\Omega}\Delta v_i\rho b_i d\Omega + \int_{\Omega}\Delta v_i\rho\dot{v}_i d\Omega = 0.\tag{1.48}$$

The weak form Eq. (1.48) does not require the continuity of the stress field, and can be therefore readily used for the FE discretization. The weak form Eq. (1.48) can be solved in a Lagrangian frame on a finite element mesh. Finite elements are used to represent the deformation of the material body, through the so called shape functions such that

$$v(\mathbf{x},t) = N_I(\mathbf{x})v_I(t),\quad \frac{dv(\mathbf{x},t)}{dt} = N_I(\mathbf{x})\frac{dv_I(t)}{dt},\quad \text{and}\quad \frac{dv(\mathbf{x},t)}{d\mathbf{x}} = \frac{dN_I(\mathbf{x})}{d\mathbf{x}}v_I(t),\tag{1.49}$$

where v is an arbitrary velocity, $N_I(\mathbf{x})$ is the shape function, $v_I(t)$ is the value of v at the nodes of elements and I is the nodal index. Figure 1.8 shows a triangular three-noded element used in 2-dimensional FEM.
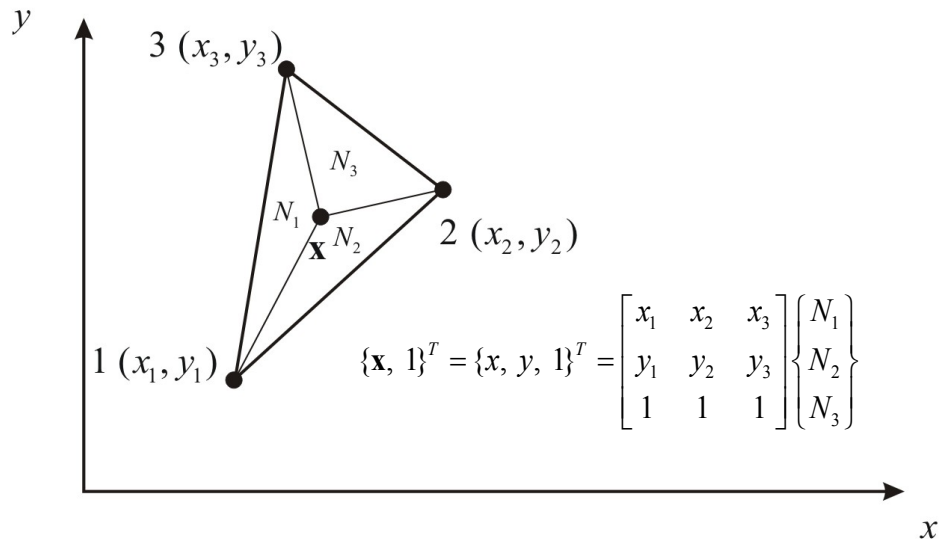
Fig. 1.8 Shape function of a Cauchy triangular element and the spatial discretization of an arbitrary point inside the element.

Applying Eq. (1.49) in Eq. (1.48), the discretization of the weak form is obtained as

$$\int_\Omega \Delta v_{iI} N_I(x_i) \rho \dot{v}_{iI} N_I(x_i) d\Omega$$

$$= \int_\Gamma \Delta v_{iI} N_I(x_i) \tau_i d\Gamma + \int_\Omega \Delta v_{iI} N_I(x_i) \rho b_i d\Omega - \int_\Omega \left(\Delta v_{iI} \frac{\partial N_I(x_i)}{\partial x_j} \sigma_{ji} \right) d\Omega. \tag{1.50}$$

Eliminating Δv_{iI} from Eq. (1.50) results in

$$\int_\Omega N_I(x_i) \rho \dot{v}_{iI} N_I(x_i) d\Omega$$

$$= \int_\Gamma N_I(x_i) \tau_i d\Gamma + \int_\Omega N_I(x_i) \rho b_i d\Omega - \int_\Omega \left(\frac{\partial N_I(x_i)}{\partial x_j} \sigma_{ji} \right) d\Omega \tag{1.51}$$

or

$$\mathbf{m}\dot{\mathbf{v}} = \mathbf{f}^{\text{ext}} - \mathbf{f}^{\text{int}}, \tag{1.52}$$

where

$$\mathbf{m} = \int_\Omega \rho N_I^T N_I d\Omega \tag{1.53}$$

$$\mathbf{f}^{\text{int}} = \int_\Omega \frac{\partial N_I(x_i)}{\partial x_j} \boldsymbol{\sigma} d\Omega = \int_\Omega B_{Ij} \boldsymbol{\sigma} d\Omega \tag{1.54}$$

and

$$\mathbf{f}^{\text{ext}} = \int_\Gamma N_I(x_i) \tau_i d\Gamma + \int_\Omega N_I(x_i) \rho b_i d\Omega. \tag{1.55}$$

In FEM, a material body is represented by a collection of finite elements. At each time step, the displacements of the nodes are obtained by solving Eq. (1.52) and the equations of motion, giving deformation of the material. The stress can be calculated from the strain inside each element and the constitutive law reflecting the property of the material. Hooke's law is the simplest form of the constitutive law given by

$$\boldsymbol{\sigma} = \mathbf{C} : \boldsymbol{\varepsilon} \tag{1.56}$$

or in a rate form

$$\dot{\boldsymbol{\sigma}} = \mathbf{C} : \mathbf{D}, \tag{1.57}$$

where $\boldsymbol{\varepsilon}$ is the strain tensor, $\mathbf{D}$ is the tensor of the rate of deformation, and $\mathbf{C}$ is the tensor of material property given by

$$\mathbf{C} = \lambda \mathbf{I} \otimes \mathbf{I} + 2\mu \mathbf{I}, \text{ where } I_{ijkl} = \frac{1}{2}(\hat{\delta}_{ik}\hat{\delta}_{jl} + \hat{\delta}_{il}\hat{\delta}_{jk}), \tag{1.58}$$

and

$$\lambda = \frac{\upsilon E}{(1+\upsilon)(1-2\upsilon)}, \ \mu = \frac{E}{2(1+\upsilon)} \tag{1.59}$$

are Lamé constants. Here $\hat{\delta}_{ij}$ is the Kronecker delta ($\hat{\delta}_{ij} = 1$ if $i = j$, and $\hat{\delta}_{ij} = 0$ if $i \neq j$). The strain can be calculated directly from the deformation gradient

$$\boldsymbol{\varepsilon} = \partial \mathbf{u} / \partial \mathbf{x}, \text{ or } \varepsilon_{ij} = \frac{1}{2}(\frac{\partial u_i}{\partial x_j} + \frac{\partial u_j}{\partial x_i}), \tag{1.60}$$

and the rate of deformation can be calculated from the velocity gradient by

$$\mathbf{D} = \partial \mathbf{v} / \partial \mathbf{x}, \text{ or } D_{ij} = \frac{1}{2}(\frac{\partial v_i}{\partial x_j} + \frac{\partial v_j}{\partial x_i}). \tag{1.61}$$

It can be seen from Eqs. (1.60) and (1.61) that $\boldsymbol{\varepsilon}$ and $\mathbf{D}$ are symmetric tensors. Generally, there exist $\partial u_i / \partial x_j = \partial u_j / \partial x_i$, and $\partial v_i / \partial x_j = \partial v_j / \partial x_i$. However, if the deformation is large, we can have $\partial u_i / \partial x_j \neq \partial u_j / \partial x_i$, and $\partial v_i / \partial x_j \neq \partial v_j / \partial x_i$ in Eqs. (1.60) and (1.61), when $i \neq j$, and the rotation has to be taken into account. As shown by Belytschko *et al.* (2000), the rotation in large deformation makes Eq. (1.56) or Eq. (1.57) inappropriate as a measure of the material deformation. Figure 1.9 shows an extreme situation where a bar under an initial stress rotates about its one end. From

the position shown in Fig. 1.9(a) to that shown in Fig. 1.9(b), the stress in the x direction has changed from σ° to 0, while the stress in the y direction has change from 0 to σ°. However, the bar simply experienced a rigid body motion and the strain is still zero, showing that something represented by Eq. (1.56) or Eq. (1.57) are inappropriate if large deformation is involved.
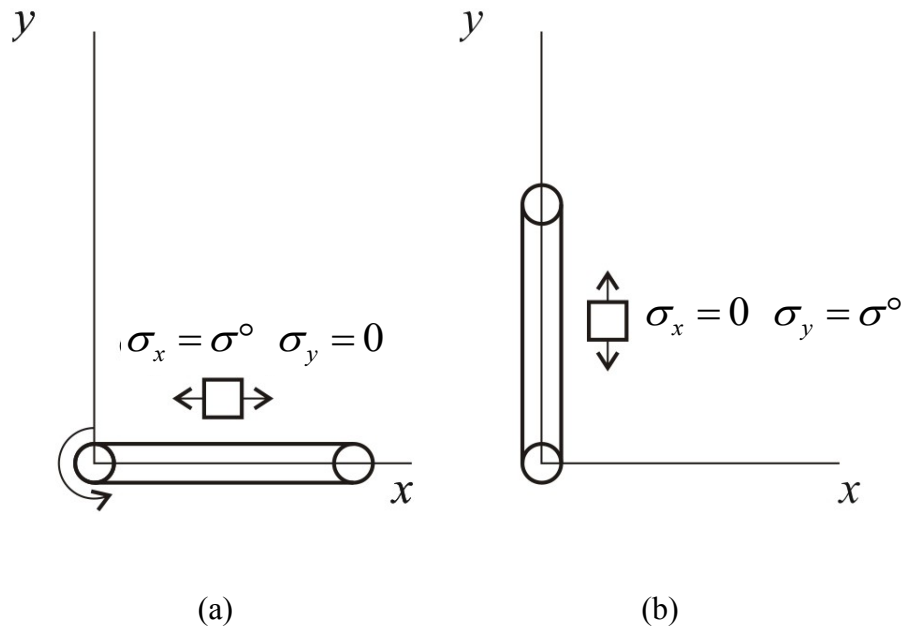
Fig. 1.9 Rotation of a bar, representing an extreme situation that the change of stress state but no change of deformation when rotation plays a role.

The objective stress rates are therefore introduced. The Jaumann rate is used throughout this thesis, which is defined by

$$\boldsymbol{\sigma}^{\nabla J} = \dot{\boldsymbol{\sigma}} - \mathbf{W} \cdot \boldsymbol{\sigma} - \boldsymbol{\sigma} \cdot \mathbf{W}^T, \tag{1.62}$$

where $\mathbf{W}$ is the spin tensor given by

$$W_{ij} = \frac{1}{2} \left(\frac{\partial v_i}{\partial x_j} - \frac{\partial v_j}{\partial x_i} \right). \tag{1.63}$$

The elastic constitutive law given by Eq. (1.56) is no longer valid. The rate form of Eq. (1.57) becomes

$$\boldsymbol{\sigma}^{\nabla J} = \mathbf{C} : \mathbf{D} \tag{1.64}$$

The stress rate can be calculated using

$$\dot{\boldsymbol{\sigma}} = \mathbf{C} : \mathbf{D} + \mathbf{W} \cdot \boldsymbol{\sigma} + \boldsymbol{\sigma} \cdot \mathbf{W}^T . \tag{1.65}$$

Other constitutive laws such as plastic flow rule are described in CHAPTER 3. The FEM is widely used to obtain contact laws (e.g. Li. *et al.*, 2000) and will be extensively discussed in CHAPTER 3. The FEM is also used to simulate the failure of brittle materials (e.g. Camacho and Ortiz, 1996). This topic will be discussed in CHAPTER 4.

1.5.2 Discrete approach－Molecular Dynamics (MD)

Molecular Dynamics is now an established approach to model material behaviours at the atomic scale. As mentioned in section 1.3.2, at the atomic level the motion of atoms in a material is governed by the inter-atomic potentials such as the Lennard-Jones potential function shown in Eq. (1.24). The Lennard-Jones type inter-atomic force acting between two atoms is given by Eq. (1.25). Atoms are abstracted into mathematical dots with mass. The equations of motion are given by

$$m_i \dot{\mathbf{v}}_i = (\mathbf{f}_{L-J})_i = \sum_{\substack{i=1 \\ i \neq j}}^{Nm} (\mathbf{f}_{L-J})_{ij} \tag{1.66}$$

where m_i and $\dot{\mathbf{v}}_i$ are the mass and acceleration of the i th atom, Nm is the total number of atoms. The displacement $\mathbf{u}_i$ and the velocity $\mathbf{v}_i$ of the i th atom can be therefore updated using the Verlet leapfrog time integration scheme (see e.g. Rapaport , 1995) that

$$\mathbf{v}_i^{t+1/2\Delta t} = \mathbf{v}_i^{t-1/2\Delta t} + \Delta t \dot{\mathbf{v}}_i \tag{1.67}$$

$$\mathbf{u}_i^{t+\Delta t} = \mathbf{u}_i^t + \Delta t \mathbf{v}_i^{t+1/2\Delta t} ,$$ (1.68)

where

$$\mathbf{v}_i^{t+1/2\Delta t} = \mathbf{v}_i^t + (\frac{1}{2}\Delta t)\dot{\mathbf{v}}_i .$$ (1.69)

The leapfrog scheme shown in Eqs. (1.67)-(1.69) requires the velocity calculated at the middle of each time step while the displacement calculated at the full time step. This scheme is proved to be efficient in reducing the numerical error due to the time integration. At each time step, the distance dependent inter-atomic force is recalculated from Eq. (1.25) to enable the iteration. The numerical procedure of MD simulation is very similar to that for the DEM simulation introduced in section 1.1. The only difference in the iteration loop is that the DEM contact law is derived from the potential functions such as the L-J potential function in MD. In DEM, only particles in contact are considered to interact with each other. In MD, all the atoms within a cut-off distance interact with each other. Calculating all the distances between all atom pairs demands high computational capability. A general technique is to divide the domain into square cells, the side length of which is slightly larger than the cut-off distance. Therefore, only atom pairs belonging to the present cell and the neighbour cells have to be considered. Details of this subcell method and other numerical techniques in MD can be found in the publication by Rapaport (1995). Various material properties including surface energies have been successfully simulated using MD, giving some significant insight about the atomistic world. MD has also been used to simulate the interactions between particles, especially to study the effect of surface energy (e.g. Kendall *et al.*, 2004). However, the MD simulation requires very small time steps to maintain the numerical stability. A typical value of the time step is 10^{-14} s. Limited by the current computational capability, all present MD simulations are restricted to very small material size (<100 nm) and very short deformation period (typically $<10^{-11}$ s). A popular approach is to combine the MD with the FEM to develop a multi-scale model. The general idea is to use FEM to simulate the large part of the material while MD is used where details are required. Various techniques have been proposed to couple the two methods which have large

spatial and temporal differences. Details of the MD-FEM combination are to be discussed in CHAPTER 5.

1.6 RESEARCH ISSUES IN MODELLING PARTICLE INTERACTIONS

The purpose of this thesis is to provide a comprehensive understanding about interactions between fine particles taking advantage of the recent development in numerical techniques. This will lay a solid foundation for computer simulation of particulate systems using the DEM. The particle interaction in real systems is much more complicated than what the existing contact laws suggest. The central idea here is to use numerical method, instead of the analytical approach, to obtain the contact laws. As mentioned above, the most important issues when considering particle interactions between particles are:

1. The contact laws between particles.
2. The failure of brittle particles.
3. The effect of surface energy on contact laws.

Firstly, most DEM simulations currently use over-simplified contact laws, such as Hertz contact law, which are inadequate for realistic particulate systems. Plasticity, large deformation, non-spherical geometry and material heterogeneity are some of the issues that require urgent attention. For soft particles, large deformation and plasticity occur even at low impact velocities. There has been very little work on particles that possess strain hardening or softening during impact although some simple analytical results exist (Li *et al*., 2000; Adams *et al*., 2004; Storakers, 1997). However, conventional finite element analysis often fails to converge due to numerical problems. Therefore, a new accurate and robust numerical method is required when solving problems involving plasticity, large deformation, strain hardening/softening, irregular particle shape, and heterogeneous materials.

Secondly, for brittle particles the particle break is inevitable and has a profound effect on the behaviour of the particulate systems. A popular treatment of brittle failure in DEM is to bond a collection of small particles together to represent a large particle, which could break into small ones (Potapov and Campbell, 1994; Kadono and Arakawa, 2002; Cheong and Reynolds, 2004). Such treatment is inconsistent with fracture mechanics because no stress analysis is involved in the DEM. On the other hand the conventional Finite Element Method (FEM) is ill-equipped to deal with multi-cracking. Although many attempts have been made to use FEM to model brittle failure (e.g. Xu and Needleman, 1994; Camacho and Ortiz, 1996), they are difficult to apply to practical problems because of the complexity in remeshing after crack occurs. Again a more reliable and simple numerical method is required to model the brittle failure of particles.

Thirdly, as the size of the particles gets smaller, the effect of surface energy becomes important. The present DEM can take this into account by using simple elastic analytical solutions such as the DMT model (Derjaguin *et al*., 1975). However, such analytical models are based on even more strong assumptions than that in the Hertz theory. According to experimental observations, (e.g. Johnson *et al*., 1971; Rimai *et al*., 2000), the effect of surface energy is much more complicated than that has been predicted analytically. Factors including plasticity, surface roughness and surface energy interplay with each other as the size of particles is small (e.g. German, 2003). Until now, there is very little understanding about the effect of surface energy for very fine particles. As mentioned above, the origin of surface energy is the inter-atomic potential. Therefore, a multi-scale model based on the macroscopic solid mechanics model and the atomistic Molecular Dynamics (MD) model is required in order to understand the interactions between very fine particles.

1.7 THE STRUCTURE OF THIS THESIS

This thesis is organized in the following structure. The present chapter outlines the motivation of the research, the theoretical background, as well as the important issues

that are studied in this thesis. Some fundamentals on numerical simulations are also introduced as a starting point for our new numerical method. The major numerical tool employed in this thesis, known as the Material Point Method (MPM), is to be introduced in CHAPTER 2. The implementation and the validation of the method are also extensively reported, giving confidence for the results presented in this thesis. In CHAPTER 3, the contact laws of particles are studied using this numerical method. The effects of large deformation, material plasticity and heterogeneity, as well as particles of irregular shapes, are comprehensively studied. It is shown in CHAPTER 3 that the existing contact laws are far from adequate and numerical simulations are necessary in obtaining contact laws. In CHAPTER 4, the failure of brittle particles is studied by extending the MPM to model multi-cracking. The new method is proved to be very simple and powerful when simulating brittle failure of particles. CHAPTER 5 attempts to further extend the MPM using the concepts from MD in order to study very fine particles. A new scheme of incorporating inter-atomic forces into MPM is developed which proves to be efficient and reliable. Some important issues such as the size effect, adhesive contact laws between fine particles, as well as the interplay between the surface energy, surface roughness and material plasticity are studied. The final chapter, CHAPTER 6 provides overall conclusions of the PhD research. Some remarks and comments, as well as the future work, are summarized in the concluding chapter.

CHAPTER 2

THE MATERIAL POINT METHOD

The Material Point Method is a numerical method developed from the Finite Element Method. This method is the major numerical tool employed in this thesis to study the interactions between fine particles. This chapter is to introduce Material Point Method and to show the advantages of this method.

2.1 REASONS OF SEEKING A NEW NUMERICAL METHOD

Contact laws in practical particulate systems are often too complicated to obtain analytically. Therefore a numerical approach is to be used as modern computers become more and more powerful. The numerical method has to be able to efficiently solve either a static contact problem or a dynamic impact problem. In this thesis, we always treat the particle interaction as a transient dynamic problem. The static contact law, which is also used in the DEM is treated as a special quasi-static case of the transient impact problem, with relatively low impact velocity. Therefore in the following discussions, we do not distinguish the contact problem from an impact problem.

In conventional FEM, there are several methods to simulate the contact problem. Some pioneer works were done by Hughes *et al*. (1974, 1976) in UC Berkeley. There developed numerical schemes of contact, such as the penalty method, which are widely used today in the contact element of commercial software. The basic ideas of contact mechanics are described below. As introduced in section 1.5.1, a dynamic FEM requires the updating of the nodal forces in order to calculate the deformation of the material. Force and displacement boundary conditions are required when contact takes place. Consider two bodies occupying domain Ω_I and Ω_{II} as shown in Fig. 2.1 in contact at a surface Γ_C. The contact surface Γ_C is a part of the solution to the

contact problem, i.e. it is unknown before the problem is solved. Two contact conditions have to be met:

(a) The two contacting bodies do not penetrate into each other i.e.

$$\Omega_I \bigcap \Omega_{II} = 0.$$ (2.1)
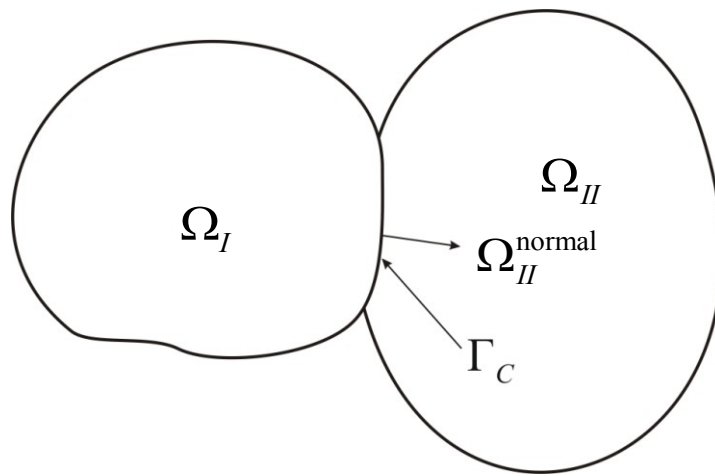
Fig. 2.1 The contacting of two material bodies, representing some general ideas of solving a contact problem.

(b) The normal traction on the contact surface Γ_C must be compressive, i.e.

$$\tau_I^{\text{normal}} \leq 0, \text{ on } \Gamma_C \text{ of } \Omega_I,$$ (2.2)

where τ_I^{normal} is the surface traction on the normal direction of the contact surface Γ_C of the material body Ω_I, as shown in Fig. 2.1. Equations (2.1) and (2.2) can be understood as displacement and force boundary conditions during contact. These two conditions have to be transformed into some other forms before being used in a

contact algorithm in FEM. Details can be found in the publication of Belytschko *et al.* (2000).

The penalty method can be used in order to meet the two conditions. A penalty force $\mathbf{f}_{\text{Pen}}$ is a virtual force applied on the two contacting bodies, enforcing the contact boundary conditions. A simple modification to Eq. (1.52) for contact problems in the conventional FEM is given by

$$
\begin{cases}
\mathbf{m}_I \dot{\mathbf{v}}_I = \mathbf{f}_I^{\text{ext}} - \mathbf{f}_I^{\text{int}} + \mathbf{f}_{\text{Pen}} \\
\mathbf{m}_{II} \dot{\mathbf{v}}_{II} = \mathbf{f}_{II}^{\text{ext}} - \mathbf{f}_{II}^{\text{int}} - \mathbf{f}_{\text{Pen}}
\end{cases}
\tag{2.3}
$$

in which *I* and *II* denote variables in Ω_I and Ω_{II}, respectively. At each time step, iterations are required to determine a suitable penalty force, making the contact problem rather time consuming to solve using the conventional FEM. Apart from the penalty method, there are also other methods of solving the contact problems using FEM, all of which require iterations. Precisely speaking, the FEM is originally derived to deal with continuous problems, while the contact problem is a problem involving discontinuities due to changes in the contact area. Therefore, there is no straightforward method of solving the contact problems using the conventional FEM.

Another problem of using the conventional FEM is mesh distortion and tangling. Conventional FEM in solid mechanics employs Lagrangian mesh, which deforms with the material. At large deformation, the mesh can be distorted severely and the accuracy of interpolation loses quickly. Sometimes mesh tangling happens in large deformation. This can be fatal for an FEM simulation because the tangled mesh will lead to an ill conditioned stiffness matrix. Remeshing techniques are invented to solve such problems at large deformation. However, remeshing requires both the accuracy in mapping variables from the old mesh to the new one and an adaptive algorithm to decide when to remesh. These complications have greatly restricted the application of the Finite Element Method on practical problems. Therefore, in order to model the interactions between particles, a simple but robust numerical method is necessary.

In recent years a number of generalized Finite Element Methods have been developed. An important breakthrough is to use the Eulerian mesh when solving large deformation problems, such as the Arbitrary Eulerian Lagrangian (ALE) mesh (Belytschko and Liu, 1985; Liu *et al.*, 1988), level set boundary tracking method (e.g. Hettich and Ramm, 2006) and etc. This thesis employs a recently developed method named as the Material Point Method (MPM).

2.2 FORMULATION OF THE MATERIAL POINT METHOD

2.2.1 Basic ideas

Material Point Method (MPM) was firstly introduced in fluid dynamics by Harlow (1964) known as the particle-in-cell (PIC) method. Later it was successfully applied to solid mechanics by Burgess *et al.* (1995) and Sulsky *et al.* (1994, 1995). The general formula and algorithm of MPM was systematically discussed in the publications by Wiezckowski *et al.* (1999) and Wiezckowski (2004). The MPM has been used to study impact problems (Sulsky and Schreyer, 1996; Li *et al.*, 2008), granular flows (Wiezckowski *et al.*, 1999; Bardenhagen and Brackbill, 1998, 2000; Bardenhagen, *et al.*, 2000) and material fractures (Sulsky and Schreyer, 2004; Li *et al.* 2008).

The basic idea of MPM is to represent a material body using discrete points named as material points. The mass of the material is concentrated onto these material points. The deformation of the material body is determined by a background mesh named as computational mesh. As shown in Fig. 2.2, the computational mesh has to cover the possible motion domain of the material body. All the state variables, such as velocity and stress, are traced on the material points and can be mapped onto the computational mesh. The computational mesh is used to determine the acceleration and stress rate. After the acceleration and stress rate are determined at a time step, the computational mesh can be discarded and a new computational mesh can be used at the next time step. The point method basically means that it does not have the problems of mesh tangling or distortion. Furthermore the use of a computational mesh

makes it straightforward to satisfy the contact boundary conditions (impenetrability and contact force). The MPM is therefore a convenient method to solve large deformation contact/impact problems. This chapter introduces the MPM in details. Some examples are also provided to show the accuracy and capability of the method.
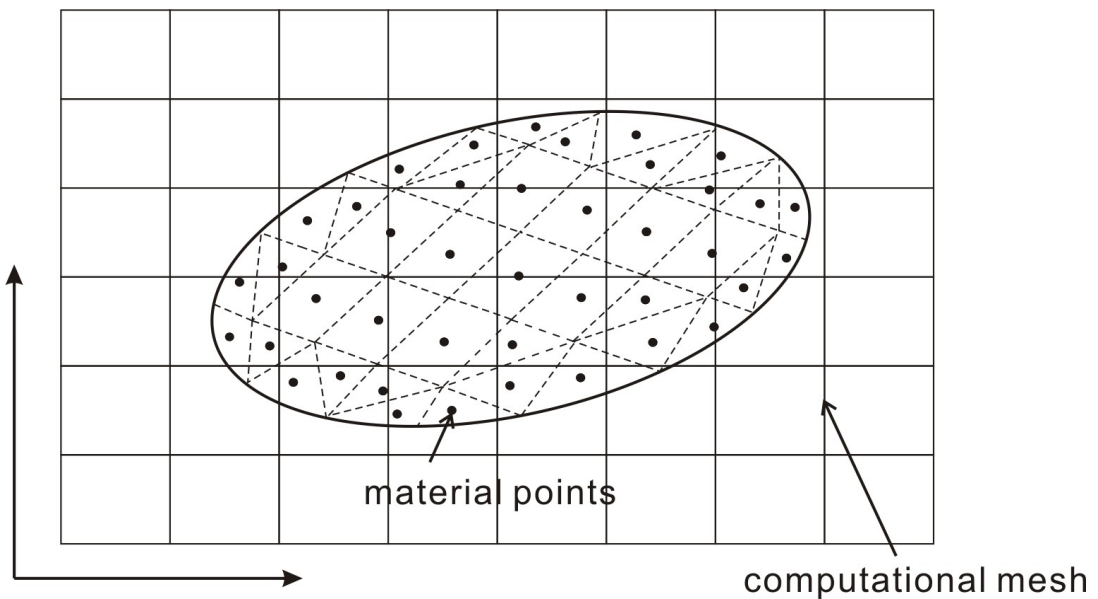
Fig. 2.2 The discretization in Material Point Method. A material body is first divided into small elements. The mass of each element is concentrated onto a material point. A background computational mesh is introduced to cover the whole domain of motion.

2.2.2 Governing equations

In the MPM, a solid body is discretized into a collection of material points by applying a density concentration function (Dirac delta function) $\tilde{\delta}$

$$\rho = \sum_{p=1}^{N_p} M_p \tilde{\delta}(\mathbf{x} - \mathbf{X}_p) \tag{2.4}$$

on the standard FE weak form, where

$$\tilde{\delta}(\mathbf{x}-\mathbf{X}_p) = \begin{cases} 1, & \text{if} \quad \mathbf{x} = \mathbf{X}_p \\ 0, & \text{if} \quad \mathbf{x} \neq \mathbf{X}_p \end{cases}. \tag{2.5}$$

The standard FE weak form, Eq. (1.48), is rewritten here in the following tensor notation on material domain Ω with boundary Γ

$$\int_\Omega \Delta\mathbf{v}\rho\dot{\mathbf{v}}d\Omega = -\int_\Omega \nabla(\Delta\mathbf{v})\boldsymbol{\sigma}d\Omega + \int_\Gamma \Delta\mathbf{v}\boldsymbol{\tau}d\Gamma + \int_\Omega \Delta\mathbf{v}\rho\mathbf{b}d\Omega \ . \tag{2.6}$$

In Eq. (2.4), ρ is the density, N_p the total number of material points, M_p the mass of a material point, $\tilde{\delta}$ the Dirac delta function, $\mathbf{x}$ the vector of spatial coordinate, and $\mathbf{X}_p$ the vector of the material point position (p in subscript denotes variables on material points). In Eq. (2.6), $\mathbf{v}$ is the velocity vector, $\Delta\mathbf{v}$ an arbitrary admissible test function of the velocity given by Eq. (1.43), $\dot{\mathbf{v}}$ the acceleration (dot denotes time derivative), $\boldsymbol{\sigma}$ the Cauchy stress tensor, $\boldsymbol{\tau}$ and $\mathbf{b}$ are the vectors of surface traction and body force, respectively. Using the property of Dirac delta function,

$$\int_\phi \tilde{\delta}(x - x_0)f(x)d\phi = f(x_0), \tag{2.7}$$

(where f is an arbitrary function) on Eq. (2.6) the discretized form of MPM is obtained as

$$\sum_{p=1}^{N_p} M_p \left\{ \dot{\mathbf{v}}(\mathbf{X}_p)\Delta\mathbf{v}(\mathbf{X}_p) + \rho_p^{-1}\boldsymbol{\sigma}\nabla[\Delta\mathbf{v}(\mathbf{X}_p)] \right\}$$

$$= \sum_{p=1}^{N_p} M_p \mathbf{b}(\mathbf{X}_p)\Delta\mathbf{v}(\mathbf{X}_p) + \int_\Gamma \Delta\mathbf{v}\boldsymbol{\tau}d\Gamma, \tag{2.8}$$

where ρ_p is the density of the material points and N_p is the number of material points. The second term on the left hand side of Eq. (2.8) includes a density variable ρ_p^{-1}, which is different from the conventional FEM. Next, a background computational mesh is used to determine the velocity of the material points. In MPM, Eulerian shape function $N_I(\mathbf{x})$ is used (I denotes the nodal index of the

computational mesh) such that, $\mathbf{v} = N_I(\mathbf{x})\mathbf{v}_I(t)$, and $\Delta\mathbf{v} = N_I(\mathbf{x})\Delta\mathbf{v}_I(t)$. Equation (2.8)
becomes

$$\sum_{p=1}^{N_p} M_p N_I^{\ T}(\mathbf{X}_p)N_I(\mathbf{X}_p)\dot{\mathbf{v}}_I$$

$$= -\sum_{p=1}^{N_p} M_p B_I^{\ T}(\mathbf{X}_p)\rho_p^{-1}\mathbf{\sigma}(\mathbf{X}_p) + \sum_{p=1}^{N_p} M_p N_I(\mathbf{X}_p)\mathbf{b}(\mathbf{X}_p) + \int_\Gamma N_I(\mathbf{X}_p)\mathbf{\tau}d\Gamma \qquad (2.9)$$

or

$$\mathbf{m}\dot{\mathbf{v}} = \mathbf{f}^{\text{ext}} - \mathbf{f}^{\text{int}}, \qquad (2.10)$$

which is exactly the same form as the conventional FEM given by Eq. (1.52). In Eq.
(2.9), B is the spatial gradient of the shape function N defined as

$$B_I(\mathbf{X}_p) = \frac{\partial N_I(\mathbf{X}_p)}{\partial \mathbf{x}}. \qquad (2.11)$$

In Eq. (2.10), $\mathbf{m}$, $\mathbf{f}^{\text{int}}$, and $\mathbf{f}^{\text{ext}}$ are the consistent mass matrix, internal nodal forces,
and external nodal forces on the computational mesh, respectively. We follow the
procedure that the bold lower case letters denote the spatial/nodal tensor variables of
the computational mesh while the bold upper case letters denote the tensor variables
of the material points. In the MPM, a lumped mass matrix is employed in explicit time
integration instead of the consistent mass matrix on the left hand side of Eq. (2.9) such
that

$$\mathbf{m} = \sum_{p=1}^{N_p} M_p N_I(\mathbf{X}_p). \qquad (2.12)$$

In Eq. (2.12), $\mathbf{m}$ is a diagonal matrix, therefore, each node on the computational mesh
is actually treated individually. The stresses are traced at the material points.
Therefore, the material points are used as numerical volume integration points to
calculate the volume integration (compared to Gauss points in conventional FEM),
hence the first term on the right hand side of Eq. (2.9) is the internal force given by

$$\mathbf{f}^{\text{int}} = \sum_{p=1}^{N_p} M_p B_I^{\ T}(\mathbf{X}_p) \rho_p^{-1} \boldsymbol{\sigma}(\mathbf{X}_p).$$ (2.13)

In order to account for large deformation, the Jaumann rate of stress measurement introduced in section 1.5.1 is used in Eq. (2.13). The density of each material point in Eq. (2.13) has to be updated at each time step to calculate the volume integration. At each time step, the density of the material point is updated according to

$$\rho_p^{t+\Delta t} = (J_t^{t+\Delta t})^{-1} \rho_p^t,$$ (2.14)

where $J_t^{t+\Delta t}$ is the determinant of the deformation gradient from the present time step t to the next time step $t + \Delta t$ (Δt is the length of the time step). Practically, the computational mesh is virtually deformed (the nodal coordinates of the computational mesh is updated) in order to calculate Eq. (2.14) that

$$J_t^{t+\Delta t} = \det\left(B^t(\mathbf{X}_p)\mathbf{x}^{t+\Delta t}\right).$$ (2.15)

The external forces including surface tractions and body forces in Eq. (2.9) are given by

$$\mathbf{f}^{\text{ext}} = \sum_{p=1}^{N_p} M_p N_I(\mathbf{X}_p)\mathbf{b}(\mathbf{X}_p) + \int_\Gamma N_I(\mathbf{X}_p)\boldsymbol{\tau}d\Gamma.$$ (2.16)

2.2.3 Mapping procedure

The mapping procedure is important in the MPM. State variables such as velocity, and acceleration, etc. are kept mapping forward and backward between the material points and the computational mesh. The idea is to use the spatial shape functions in order to gather information of the required position from those of the nearby points. During the mapping process, it must be bear in mind that the state variables are traced at the material points, the number of which is much larger than the number of nodes of the computational mesh. One basic step is to map the mass of a material point to the nodes of the computational mesh, i.e. to calculate the lumped mass matrix

$$m_I = \sum_{p=1}^{N_p} M_p N_I(\mathbf{X}_p). \tag{2.17}$$

The velocities of the material points are mapped onto the nodes of the computational mesh in two steps. Firstly, the momentum of the material points are mapped onto the nodes of the computational mesh by momentum conservation such that

$$m_I \mathbf{v}_I = \sum_{p=1}^{N_p} M_p \mathbf{V}_p N_I(\mathbf{X}_p). \tag{2.18}$$

Then the nodal velocity is calculated by dividing the nodal momentum by the nodal mass. The mapping from the nodes of the computational mesh to the material points follows the standard interpolation procedure that

$$\dot{\mathbf{V}}_p = \sum_I \dot{\mathbf{v}}_I N_I(\mathbf{X}_p) \tag{2.19}$$

and

$$\mathbf{V}_p = \sum_I \mathbf{v}_I N_I(\mathbf{X}_p). \tag{2.20}$$

Accelerations are not mapped from the material points to the computational mesh because the equation of motion, Eq. (2.10), is solved at the computational mesh.

The shape function N_I is generally the shape function of a cell of the computational mesh. Sometimes the nodal mass m_I can be very small if the cell is at the boundary of the material body. For example, as shown in Fig. 2.3, two material points lie near the two sides of a four noded cell. The mass on node I' is very small or even equal to zero. A small nodal mass may produce a large error because the nodal mass of the computational mesh is used as the denominator in Eq. (2.10) and Eq. (2.18). Therefore, in the boundary cells, special care of the mapping procedure is required, which is discussed in the next section.
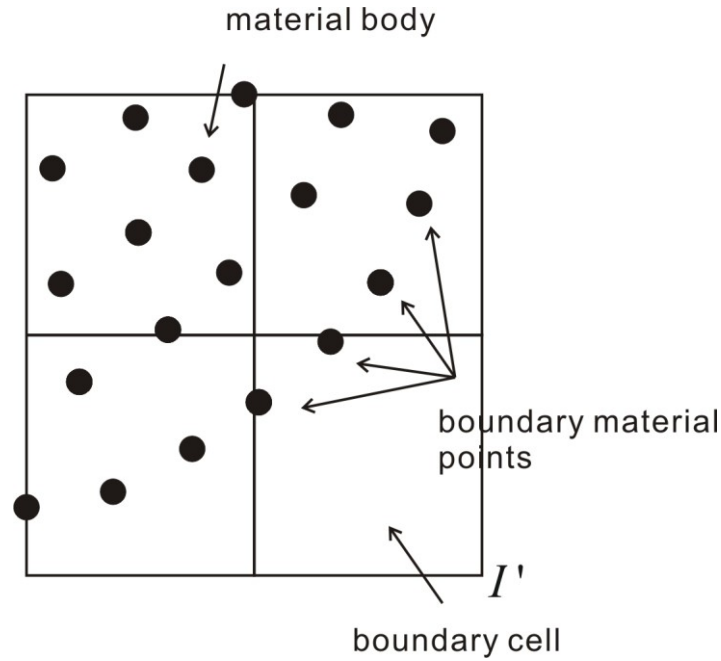
Fig. 2.3 Special care for boundary cells. The nodal mass of node I' is very small in the lumped mass matrix.

2.2.4 Time integration of the dynamic equations

The time integration of the dynamic equations of MPM begins from the material points, where all the state variables are traced. At the beginning of each time step t, the nodal mass m_I^t and the nodal velocities $\mathbf{v}_I^t$ are firstly calculated through the mapping procedure defined in Eq. (2.17) and Eq. (2.18) such that

$$m_I^t = \sum_{p=1}^{N_p} M_p N_I(\mathbf{X}_p^t) \tag{2.21}$$

and

$$\mathbf{v}_I^t = \frac{1}{m_I^t} \sum_{p=1}^{N_p} M_p \mathbf{V}_p^t N_I(\mathbf{X}_p^t). \tag{2.22}$$

Since the stress $\boldsymbol{\sigma}^t(\mathbf{X}_p^t)$ is traced by the material points, the internal force $\mathbf{f}^{int}$ can be calculated from Eq. (2.13) as

$$(\mathbf{f}_I^{int})^t = \sum_{p=1}^{N_p} M_p B_I^{\ T}(\mathbf{X}_p^t) \frac{1}{\rho_p^t} \boldsymbol{\sigma}^t(\mathbf{X}_p^t) . \tag{2.23}$$

Similarly, the external force $\mathbf{f}^{ext}$ can be obtained from Eq. (2.16)

$$(\mathbf{f}_I^{ext})^t = \sum_{p=1}^{N_p} M_p N_I(\mathbf{X}_p^t) \mathbf{b}^t(\mathbf{X}_p^t) + \int_\Gamma N_I(\mathbf{X}_p^t) \boldsymbol{\tau}^t d\Gamma \tag{2.24}$$

The equation of motion of Eq. (2.10) can be used to obtain the nodal acceleration of the next time step $t + \Delta t$ as following

$$\dot{\mathbf{v}}_I^{t+\Delta t} = \frac{1}{m_I^t} \left[(\mathbf{f}_I^{int})^t - (\mathbf{f}_I^{ext})^t \right] . \tag{2.25}$$

The material point velocities are updated by using the mapping equation Eq. (2.19) such that

$$\mathbf{V}_p^{t+\Delta t} = \mathbf{V}_p^t + \Delta t \sum_I \dot{\mathbf{v}}_I^{t+\Delta t} N_I(\mathbf{X}_p^t) . \tag{2.26}$$

The nodal velocities of computational mesh can be updated either from the equation of motion:

$$\mathbf{v}_I^{t+\Delta t} = \mathbf{v}_I^t + \Delta t \dot{\mathbf{v}}_I^{t+\Delta t} \tag{2.27}$$

or from Eq. (2.18), i.e. mapped from the updated velocities of the material points $\mathbf{V}_p^{t+\Delta t}$ as following

$$\mathbf{v}_I^{t+\Delta t} = \frac{1}{m_I^t} \sum_{p=1}^{N_p} M_p \mathbf{V}_p^{t+\Delta t} N_I(\mathbf{X}_p^t) . \tag{2.28}$$

The rate of deformation can be therefore calculated from the updated nodal velocity as

$$\mathbf{D}^{t+\Delta t}(\mathbf{X}_p^t) = B_I(\mathbf{X}_p^t)\mathbf{v}_I^{t+\Delta t} . \tag{2.29}$$

The stress rate $\dot{\boldsymbol{\sigma}}^{t+\Delta t}$ can be calculated according to the constitutive law, and the stress $\boldsymbol{\sigma}$ is updated by

$$\boldsymbol{\sigma}^{t+\Delta t} = \boldsymbol{\sigma}^t + \Delta t \dot{\boldsymbol{\sigma}}^{t+\Delta t} . \tag{2.30}$$

The density can be updated using Eq. (2.14) such that

$$\rho_p^{t+\Delta t} = \rho_p^t \left[\det B(\mathbf{X}_p^t)\mathbf{x}_I^{t+\Delta t} \right]^{-1} = \rho_p^t \left[\det B(\mathbf{X}_p^t)(\mathbf{x}_I^t + \Delta t \mathbf{v}_I^{t+\Delta t}) \right]^{-1} . \tag{2.31}$$

And finally, the positions of the material points are updated by mapping the nodal velocities to the material points using Eq. (2.20):

$$\mathbf{X}_p^{t+\Delta t} = \mathbf{X}_p^t + \Delta t \sum_I N_I(\mathbf{X}_p^t)\mathbf{v}_I^{t+\Delta t} . \tag{2.32}$$

It is important to point out that during the above procedure, the nodal velocity vector $\mathbf{v}_I^{t+\Delta t}$ can be calculated using either Eq. (2.27) or Eq. (2.28). The nodal velocities of the computational mesh, $\mathbf{v}^{t+\Delta t}$, are important as they are used in updating both the stresses and material point positons. In our numerical simulations, both equations are used as explained in the following. If a direct calculation using Eq. (2.27) is employed, then some material points located near the free boundary may separate from the rest of the body. As illustrated in Fig. 2.3, this is possible when the number of material points in one computational cell is very small, e.g. near the free boundary. The mass on some nodes m_I^t calculated from Eq. (2.21) tends to zero while the corresponding nodal internal forces $(\mathbf{f}_I^{\text{int}})^t$ calculated from Eq. (2.23) do not. This could lead to excessive nodal accelerations, resulting unrealistic separations of the material points from the free boundary. A smoothing technique of Eq. (2.28) was suggested by Sulsky *et al.* (1995) to overcome this problem. However, we have observed that, Eq. (2.28) may introduce additional numerical error which leads to numerical oscillations. While Sulsky and Schreyer (1996) still employed Eq. (2.27) in their later publications, our approach is to use Eq. (2.28) only at the boundary cells of the computational mesh.

At each time step, the material boundary is searched to decide whether it is necessary to use Eq. (2.28). It is proved that such procedure has effectively avoided the problem of the material point separation and neutralized the numerical problem.

2.3 VALIDATION OF THE COMPUTER CODE

The above numerical procedure is implemented into a computer program. A flow chart of the programming is provided in APPENDIX II. As suggested by Sulsky and Schreyer (1996), an elastic spherical particle undergoing free vibration is used as a benchmark test for our MPM code. As shown in Fig. 2.4, a spherical particle is discretized into a collection of material points. A square computational mesh is used covering the possible domain of the moving particle. The material points and the computational mesh are constructed uniformly. The axisymmetric formulation of the MPM is used so that the particle in Fig. 2.4 represents a three dimensional sphere. Only half of the sphere is modelled due to symmetry. The particle has a radius $R = 0.6\,\text{m}$, Young's modulus $E = 150$ GPa, Poisson's ratio $v = 0.3$, and density of $\rho = 7 \times 10^3$ kg/m^3. The deformation is assumed to be pure elastic. The centre of the spherical particle is initially located at the position $r = 0$ m, and $z = 1$ m. The domain represented by the computational mesh is 1 m × 2 m, which covers the possible domain of the particle motion. To satisfy the axisymmetry condition, the r-direction of the nodal forces and velocities on the axisymmetric axis of the computational mesh are set as zero. In order to model the free vibration, each material point is initially assigned a radial velocity given by

$$\mathbf{V}_p^{\text{vibration}}(r,z) = 0.02\sqrt{r^2 + (z-1)^2}\,\hat{\mathbf{R}}\,,\tag{2.33}$$

where $\hat{\mathbf{R}}$ is the unit radial vector. Equation (2.33) implies the initial condition of a spherical particle vibrating in its fundamental mode. The analytical solution of the angular frequency $\omega^{\text{vibration}}$ can be obtained by

$$\tilde{x}_1 = \omega^{\text{vibration}} R / C_L\,,\tag{2.34}$$

where C_L is the longitudinal wave speed given by

$$C_L = \sqrt{E / \rho(1-\upsilon^2)} \qquad\qquad (2.35)$$
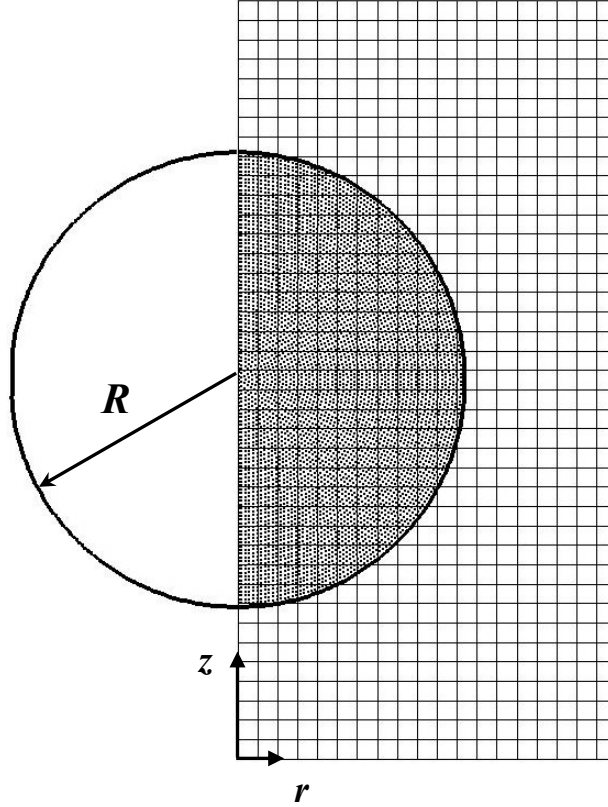
Fig. 2.4 Construction of an axisymmetric spherical particle in MPM. Half of the particle is discretized and is put into a square background computational mesh.

and $\tilde{x}_1$ is the smallest root of equation

$$j_0(\tilde{x}) - \frac{4\mu}{(2\mu+\lambda)\tilde{x}} j_1(\tilde{x}) = 0 . \qquad\qquad (2.36)$$

In Eq. (2.36), μ and λ are Lamé constants, which can be calculated form E and υ as $\lambda = 57.69$ GPa, $\mu = 38.46$ GPa, $j_0(\tilde{x})$ and $j_1(\tilde{x})$ are spherical Bessel functions of order zero and one. From Eqs. (2.34)-(2.36), we have $C_L = 4852$ m/s, $\tilde{x}_1 = 2.67$ and the value of the angular frequency of the vibrating particle can be calculated as

$\omega^{\text{vibration}} = 21.4$ KHz. In order to validate our computer program, as well as testing the convergence of the MPM, several numerical simulations using different mesh constructions are performed. Due to the two kinds of discretizations employed by the Material Point Method, the convergence behaviours are more complicated than the conventional FEMs. The number of material points and the number of cells of the computational mesh are two parameters in MPM. Alternatively, the number of material points per unit cell (material point density) can be used as a mesh parameter along with the total number of material points. The results of the numerical simulation using different mesh statuses are shown in Table 2.1. The size of the computational mesh is chosen to be smaller than the wavelength of the vibration. The kinetic energy of the particle from mesh status 1 is plotted against time in Fig. 2.5. For mesh status 1, the time step is 50 ns, consuming about 0.002 cpu seconds on one 2.2Ghz AMD Opteron 848 Processor. Smaller time step is used while consuming longer cpu seconds as the mesh is refined.
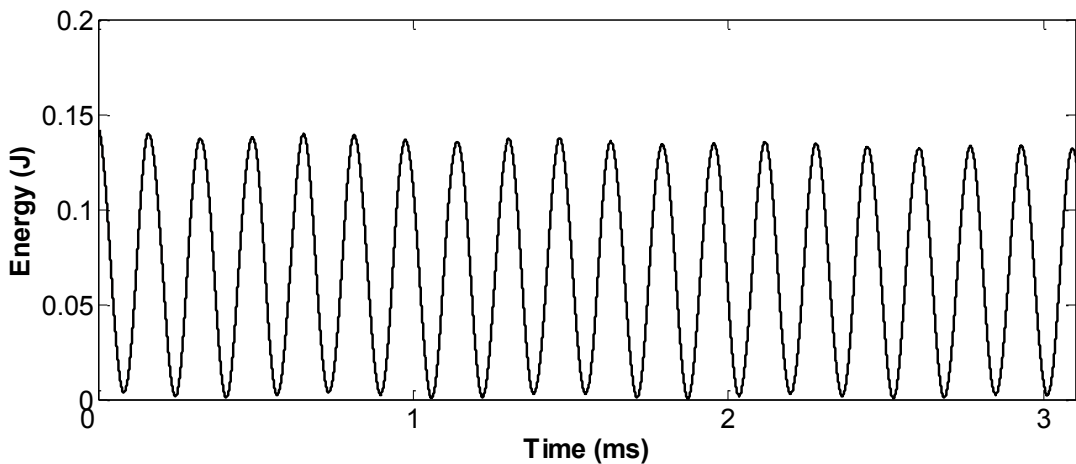
Fig. 2.5 The kinetic energy of a particle under free vibration is plotted against time. The angular frequency of the particle is half of that of the kinetic energy. The period of the energy oscillation is therefore equal to $\pi / \omega^{\text{vibration}}$.

It is noticed that the frequency of vibration $\omega^{\text{vibration}}$ can be observed from the variation of kinetic energy in Fig. 2.5. At the same time, a discernable amount of

energy is dissipated after several periods. The measurement of the energy dissipation follows the method used by Sulsky and Schreyer (1996). Energy dissipates exponentially and can be described using a function of $\tilde{E}_0 \exp(-\kappa \omega^{\text{vibration}} t / 2\pi)$, where $\tilde{E}_0$ is the initial kinetic energy and κ is the measurement of the energy dissipation. Numerical results of different mesh statuses are shown in Table 2.1. For the free vibration test of a particle, Table 2.1 shows that the numerical results of the angular frequency $\omega^{\text{vibration}}$ using all mesh statuses agree reasonably well with the analytical prediction. The MPM programme is therefore validated. Some interesting numerical properties of MPM can also be observed from Table 2.1. As the mesh is refined, the numerical result of $\omega^{\text{vibration}}$ is approaching the analytical solution. The energy dissipation is also reduced by refining of the mesh. System energy dissipates due to either numerical error or the dynamic wave propagation of the particle. Considering the fact that much smaller time step is required for a finer mesh, it can be concluded that all the mesh statuses in Table 2.1 converge in the test of the free vibration problem.

The mesh convergence and the accuracy tests will be performed throughout the thesis before solving each practical problem.

Table 2.1 Numerical results of the angular frequency and energy dissipation of the spherical particle, as the mesh of MPM is refined.

Study case index	Number of Material points	Number of cells (in 1m × 2m square)	Material points density	$\omega^{\text{vibration}}$ (KHz)	Energy dissipation parameter κ
1	5551	20×40	22.93	19.552	0.0386
2	21901	32×64	35.55	19.676	0.0320
3	87001	50×100	59.38	19.688	0.0294
3	346801	80×160	94.01	19.691	0.0215

2.4 CAPABILITY DEMONSTRATION

As introduced in section 2.2, the MPM was initially developed to deal with large deformation problems. Here we consider a soft particle being penetrated by a hard rod as a demonstration example. While the MPM can simulate the problem without remeshing, the problem is very difficult to deal with using the conventional FEM due to mesh distortion. Snapshots of the simulated penetration are shown in Fig. 2.6. A soft particle with Young's modulus as low as $15\,\text{MPa}$ is penetrated by an infinite long rigid rod, with a normal initial velocity of -8 m/s. The mesh status 1 in Table 2.1 is used. The material is assumed to be elastic perfectly plastic with a yield strength of 0.14 MPa. Frictionless contact boundary conditions are assumed between the penetrating rod and the particle. The initial status is shown in Fig. 2.6(a), when the rod is just in point contact with the particle. For simplicity, the rod is not shown in the following snapshots. In Fig. 2.6(b), the contact begins between the particle and the rod. The particle is flattened inside the contact area, while the remaining part of the particle is still undeformed. Figures 2.6(c)-(d) show the rod is penetrating into the particle. The material of the particle in front of the rod is compressed severely and forced to move aside. The shape of the outer boundary of the particle is considerably changed. When the rod penetrates about $1/3$ into the particle, as shown in Fig. 2.6(e) the particle has experienced a very large deformation. The deformation is however localised around the penetrating rod, where the distances between material points are very small. The final status is shown in Fig. 2.6(f), when the kinetic energy of the rod is fully converted to the deformation energy and the relative motion between the rod and the particle stops. The flow of the materials can be clearly observed in Figs. 2.6(a)-2.6(f). As the rod penetrates, material is extruded near the free boundary at the bottom of the particle due to incompressibility of the material. The simulation shown in Fig. 2.6 requires no special treatment of mesh distortion in the programme. Neither any iteration is required to deal with the contact boundary condition.
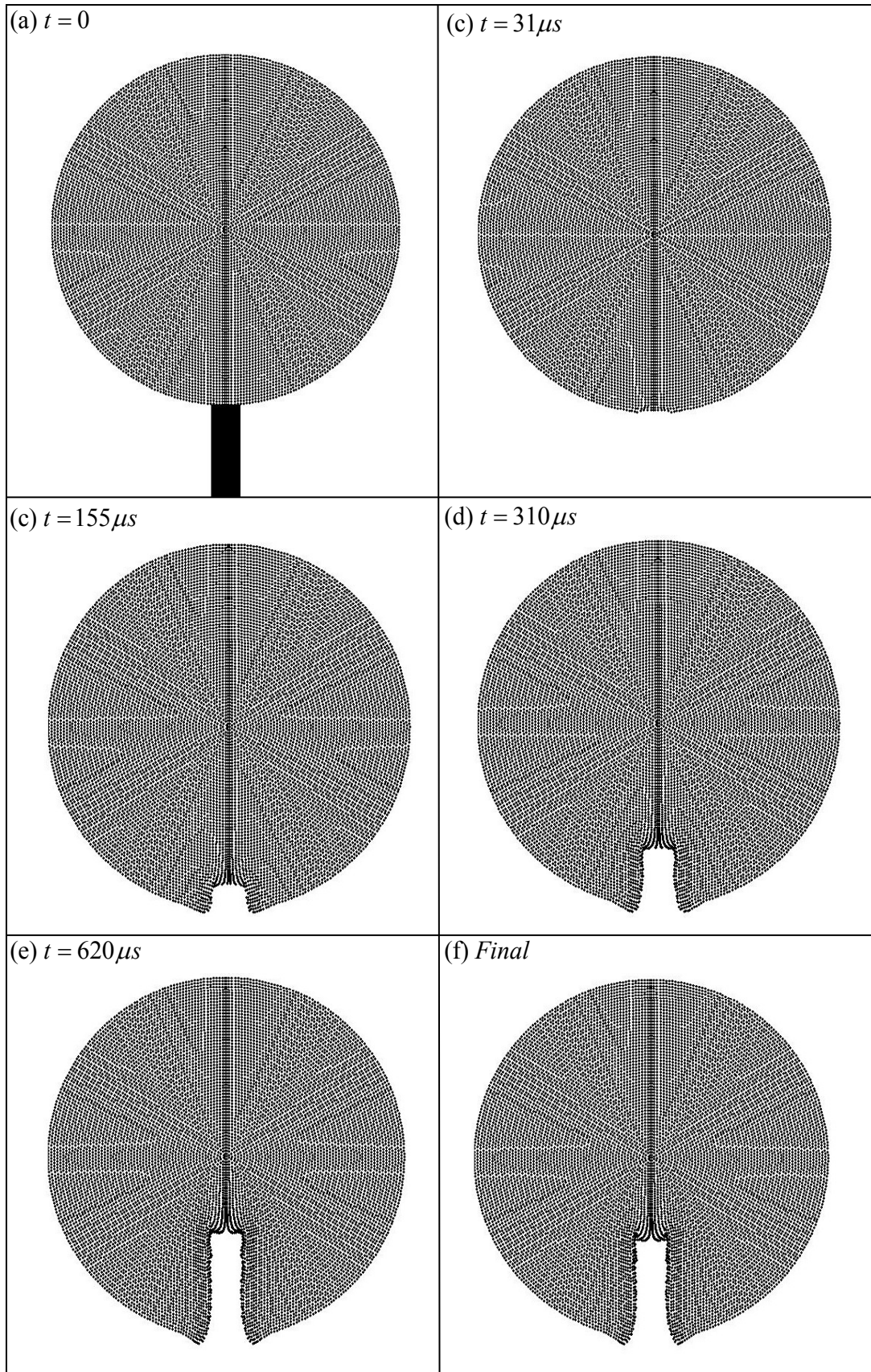
Fig. 2.6 Snapshots of the simulation of a soft particle penetrated by a rigid rod. In order to demonstrate the capability of solving large deformation problems of MPM.

2.5 SUMMARY OF THIS CHAPTER

In this chapter, the major numerical tool of the thesis, the Material Point Method (MPM), is introduced in details. It is shown that the MPM can be used to solve the problem of particle interaction taking large deformation and contact boundary conditions into account in a straightforward manner. The major advantage of the MPM is it does not require extra computer programming effort to deal with mesh distortion and contact boundary conditions, which is a major difficulty when using a conventional Finite Element Method. Numerical methods employing two kinds of discretization are often referred to as the FE^2 method, which usually require more computational time because of the mapping between the two meshes. In our observations, the computational cost of MPM is reasonable. The mesh refinement in Material Point Method is also affordable. For example, considering a model with $\mathfrak{M}1$ material points and $\mathfrak{M}2$ cells in computational mesh, if the material point number is increased by $\mathfrak{A}1$ times, and the cell number of the computational mesh is increased by $\mathfrak{A}2$ times, because the mappings forward and backward between material points and computational mesh are implemented independently, the computational complexity increases by $(\mathfrak{A}1 \times \mathfrak{M}1 + \mathfrak{A}2 \times \mathfrak{M}2)/(\mathfrak{M}1 + \mathfrak{M}2)$ times. Comparing to the usual increasing by $\mathfrak{A}1 \times \mathfrak{A}2$ time in some other FE^2 methods, mesh refinement in the MPM is reasonably affordable. Another appealing feature of the MPM is that the problem construction is fairly easy. The difficulty in mesh construction lies in the complicated graphic algorithms which usually require a commercial mesh generator. The situation is much easier when only dealing with material points. One can construct a very large collection of material points in a three dimensional space, from which any shape of a material body can be cut out by knowing the boundary profile of the object.

In the following chapters, the MPM is used to study a range of important issues when studying the interaction between particles.

CHAPTER 3

THE CONTACT LAW BETWEEN PARTICLES

This chapter is focusing on the study the contact mechanics of particles using the Material Point Method. Providing numerical contact laws of different kinds of particles is the goal of this chapter.

3.1 THEORETICAL BACKGROUND

3.1.1 Force-displacement contact law

In this chapter, the mechanical contact law is studied. Plasticity is an important mechanism during the impact between particles. For soft materials, the particles first deform elastically and then quickly plastic deformation takes place, which is generally referred to as elastoplastic deformation. Figure 3.1(a) shows a spherical particle of radius R impacting on a rigid wall, which also represents the symmetry conditions of two identical particles coming into contact. At the beginning of the impact, the force between the particle and the rigid wall, F, and the displacement of the centre of the particle, δ, increase forming a circular contact area with radius a. Both F and δ will reach their maximum values but not necessarily at the same time during the impact. Then the particle rebounds and finally separates from the wall. The relation between F and δ is referred to as the contact law.

Although there are various theories addressing the contact law, the basic procedure is always the same. On the one hand, the contact force is an integration of the contact pressure distributed over the contact area. This integration provides a connection between the contact force F and the radius of the contact area, a. On the other hand, the profile of the sphere near the contact area is represented by a relatively simple function such that a connection is made between δ and a. The contact law is then

determined by eliminating the contact radius a from the two connections. As introduced in section 1.3, the simplest example of the contact law is the Hertz theory, some of which is to be rewritten here as a starting point. The elastic contact pressure distribution p_{Hertz} at any point r within the contact area is explicitly given by (e.g. Johnson, 1985)

$$p_{\text{Hertz}}(r) = P_0^e \left[1 - (r/a)^2 \right]^{1/2} \tag{3.1}$$

where P_0^e denotes the maximum pressure at the centre of the contact area. Equation (3.1) is shown by curve ACA' in Fig. 3.1(b). The particle shape near the contact area is assumed to be parabolic, i.e. we have

$$\delta = a^2 / \tilde{R} \tag{3.2}$$

where $\tilde{R}$ is the curvature of the particle surface near the contact area as shown in Fig. 3.1(a). For small and elastic deformation, Hertz suggested that $\tilde{R} = R$. The Hertz contact law is then given by

$$F = (4/3)R^{1/2}E^*\delta^{3/2} \tag{3.3}$$

which is shown by curve OA in Fig. 3.1(c), for which the loading and unloading curves are identical.

For elastoplastic impact, obtaining the expressions for the contact pressure and the particle profile becomes more difficult. The loading and unloading curves are different due to plastic deformation as shown by curve $OB\delta_{\text{res}}$ in Fig. 3.1(c), where δ_{res} represents the permanent residual displacement. The particle profile near the contact area keeps changing during the impact due to irreversible piling-up and sinking-in effects. Therefore, the connections between δ and a is no longer easy to obtain. For elastic perfectly plastic spherical particles, Johnson (1985) found that plastic deformation starts beneath the contact area when the maximum contact pressure reaches 1.6 times of the uniaxial yield stress. By equating this value of

elastic limit with the Hertz elastic theory, Johnson (1985) derived a velocity V_y, which is the velocity required for the onset of plastic deformation:
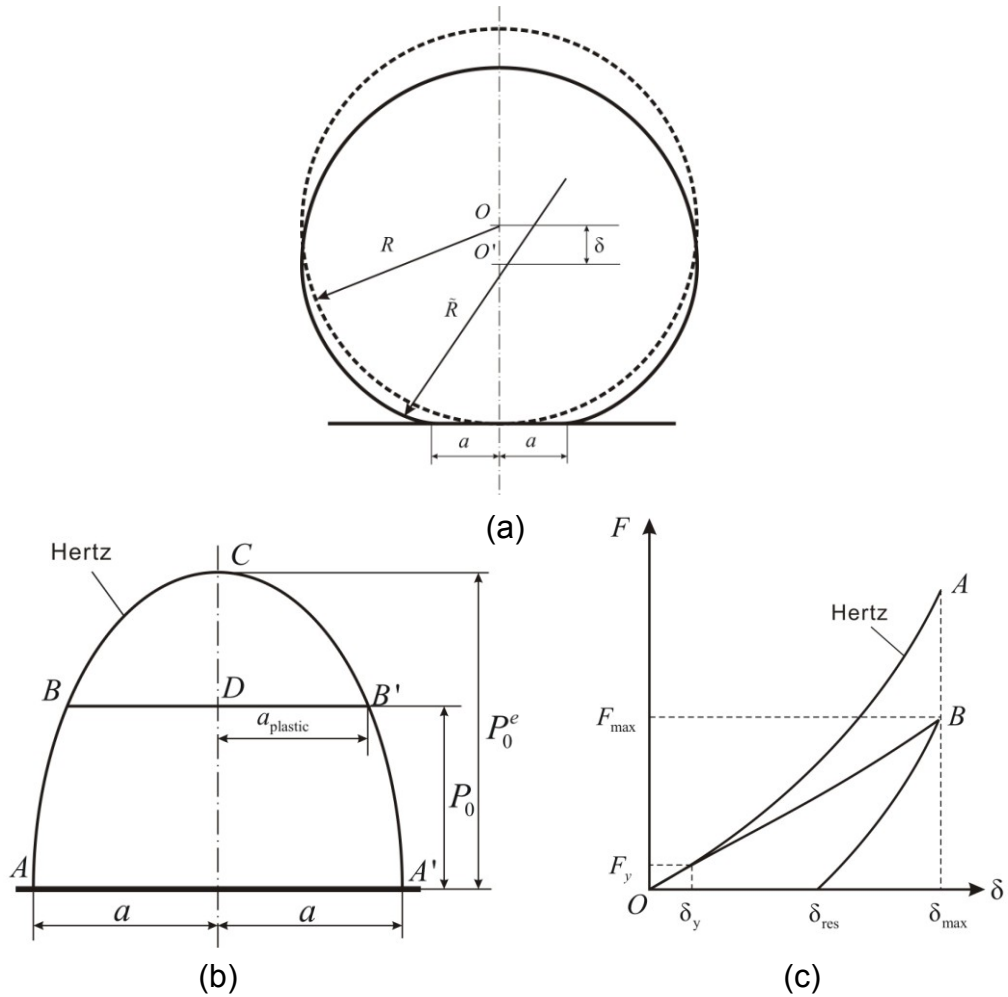
Fig. 3.1 Contact between a sphere and a rigid wall. (a) Initial and deformed spheres, (b) pressure distribution within the contact area, and (c) force-displacement relationships.

$$\frac{\rho V_y^2}{Y} = 26(Y/E^*)^4 \qquad (3.4)$$

in which ρ is the density, Y is the uniaxial yield stress, and E^* is the effective elastic modulus defined as $E^* = E/(1-\upsilon^2)$ with E and υ are Young's modulus and Poisson's ratio. At the onset of plastic deformation, the radius of the contact area a_y, the contact force F_y and the displacement δ_y are given by

$$a_y = \frac{1.6\pi YR}{2E^*},$$

(3.5)

$$F_y = \frac{16}{15}\pi a_y^2 Y,$$

(3.6)

and

$$\delta_y = \frac{a_y^2}{R}$$

(3.7)

respectively. During plastic impact the contact pressure is more uniform within the contact area compared to that given by Eq. (3.1). Johnson (1985) suggested using the mean pressure P_m, which varies from $1.6Y$ at the onset of plastic deformation to $\bar{\varepsilon}Y$ when full plasticity is reached. At full plasticity, the mean contact pressure P_m remains constant as $\bar{\varepsilon}Y$. The value of $\bar{\varepsilon}$ was found to be 3.0 by Johnson (1985) and Storakers (1997), and between 2.7 and 3.0 by Mesarovic and Fleck (2000). Thornton (1997) and Li $et\ al.$ (2002) assumed the pressure distribution marked by $ABDB'A'$ as shown in Fig. 3.1(b) and suggested that the maximum pressure P_0 varies from $1.6Y$ at the onset of plastic deformation to $2.85Y$ at full plasticity. In order to fully describe the variation of P_m or P_0, various fitting functions for the pressure distribution have been proposed. Vu-Quoc and Zhang (1999) decomposed the radius of the contact area a into an elastic part a^{elastic} and a plastic part a^{plastic} and assumed a linear relation between the contact force F and the plastic contact radius a^{plastic}. Li $et\ al.$ (2002) used an exponential function between the maximum contact pressure P_0 and the radius of the contact area a. Mesarovic and Fleck (2000) performed a comprehensive numerical study which outlined the validity conditions for $P_m = 3.0Y$ at full plasticity as suggested by Johnson (1985) and Storakers (1997). The theories of full plasticity break down if the deformation becomes large as observed numerically by Mesarovic and Fleck (2000), and experimentally by Chaudhri $et\ al.$ (1984) and Timothy $et\ al.$ (1987). It is found that if deformation is large enough, the mean contact pressure P_m will first increase to its peak value, hold for a while, and then start to decrease before the particle rebounds (Mesarovic and Fleck, 2000).

Almost all the theories assume that the profile of the sphere near the contact area can be represented by the parabolic Eq. (3.2). During the elastoplastic loading and the elastic unloading, a variation of $\tilde{R}$ in Fig. 3.1(a) is expected. In Johnson's (1985) and Thornton's (1997) theories, $\tilde{R}$ remains constant during loading, and is modified during unloading to account for the permanent deformation. In fact the particle curvature $\tilde{R}$ as shown in Fig. 3.1(a) varies with time. Mesarovic and Fleck (2000) found that $\tilde{R}$ varies between R at the start of contact and $2.8R$. Vu-Quoc and Zhang (1999) and Li *et al.* (2002) used empirical fitting functions to account for the variation of $\tilde{R}$ during contact.

In the above analyses, it is worth noticing that P_m is approaching P_0 along with the increasing amount of plastic deformation. The elastic part is getting smaller and can be ignored after the full plasticity is reached. P_m is experimentally and numerically convenient while P_0 is physically explicit to understand. In most existing theories, the shape of the force-displacement curve of the impact between an elastic perfectly plastic spherical particle and a rigid wall is similar to the curve $OB\delta_{res}$ shown in Fig. 3.1(c). Comparing to the elastic force-displacement curve in Hertz theory, the loading curve is less stiff while the unloading curve is slightly stiffer because $\tilde{R}$ is larger than R during the unloading.

3.1.2 The coefficient of restitution

Practically there are seldom impacts between particles are purely kinetic energy conservative. Coefficient of restitution is therefore introduced to represent the kinetic energy dissipation during the impact. The coefficient of restitution e is defined as the ratio between the impact velocity V_0 and rebound velocity V_r, which represents the kinetic energy dissipation during the impact. Compared with the contact law, e is relatively easy to obtain theoretically (Johnson, 1985; Thornton, 1997), numerically (Li *et al.*, 2002; Wu *et al.*, 2003, 2005) or experimentally (Mangwandi *et al.*, 2007). When the contact law is unavailable or a reduction in the complexity of the problem is

necessary, the coefficient of restitution can be used to simulate the particulate systems (e.g. Hoomans, 2000).

Even in the elastic regime, kinetic energy can be dissipated by the propagation of elastic waves. Hunter (1957) showed theoretically that this energy loss is less than 1% of the initial kinetic energy. Hutchings (1979) showed that the energy loss due to elastic waves in a plastic impact is less than 3% of the total kinetic energy. In a particulate system, Wu *et al*. (2005) showed that if the duration of the impact is large enough and the elastic waves can be reflected back by particle interfaces, the energy dissipation due to elastic waves will be much smaller. In elastoplastic impact, the dominant mechanism for the loss of kinetic energy is plastic deformation. This loss of kinetic energy is represented by the area under the force-displacement curve (area $OB\delta_{res}$ in Fig. 3.1(c)). Generally, for identical particles, the coefficient of restitution will be always less than 1 and decrease with the increasing of impact velocity. For elastic perfectly plastic spherical particles, Johnson (1985) related the coefficient of restitution to the mean contact pressure P_m such that

$$e^2 = \frac{V_0^{\,2}}{V_r^{\,2}} = \frac{3\pi^{5/4}4^{3/4}}{10}\left(\frac{P_m}{E^*}\right)\left(\frac{0.5mV_0^2}{P_mR^3}\right)^{-1/4},$$

(3.8)

in which m is the mass of the particle. Alternatively, Thornton (1997) related the coefficient of restitution to the maximum contact pressure P_0 such that

$$e = \left(\frac{6\sqrt{3}}{5}\right)^{1/2}\left[1-\frac{1}{6}\left(\frac{\bar{V}_y}{V_0}\right)^2\right]^{1/2}\left[\frac{\left(\dfrac{\bar{V}_y}{V_0}\right)}{\left(\dfrac{\bar{V}_y}{V_0}\right)+2\sqrt{\dfrac{6}{5}-\dfrac{1}{5}\left(\dfrac{\bar{V}_y}{V_0}\right)^2}}\right]^{1/4}$$

(3.9)

in which

$$\bar{V}_y = 1.56\left(\frac{P_0^5}{E^{*4}\rho}\right)^{1/2}.$$

(3.10)

Equations (3.8) and (3.9) become identical after full plasticity is reached when P_m is very close to P_0. Wu $et\ al.$ (2003) indicated that $\overline{V}_y$ defined by Eq. (3.10) is equal to V_y defined by Eq. (3.4) at the onset of yield, and increases until P_0 reaches $2.85Y$. As one can see from Eqs. (3.8)-(3.10), the coefficient of restitution follows a power law dependence with the exponent of $-1/4$, after full plasticity is reached. At large deformation, the decrease in e as the impact velocity V_0 increases is faster than that predicted by Eq. (3.8) or (3.9) and cannot be uniquely determined from V_0/V_y. Wu $et\ al.$ (2003, 2005) suggested the following empirical relation:

$$e = 0.58 \left(\frac{V_0/V_y}{E^*/Y} \right)^{-0.49} \tag{3.11}$$

for large deformation impact, in which V_y is defined by Eq. (3.4).

3.2 THE NUMERICAL MODEL AND ITS VALIDATION

3.2.1 The plasticity model

The Material Point Method (MPM) introduced in CHAPTER 2 is employed here to simulate the impact of particles. Figure 3.2 shows the material point model and computational mesh used in the study. Axisymmetric conditions are assumed. The rigid wall is represented by setting zero vertical velocity and acceleration for all the nodes at the bottom line of the computational mesh. The bottom row of the computational mesh is thinner than others to represent a rigid wall. The boundary condition at the contact is assumed to be frictionless. However if the model is viewed as impact between two identical particles, then the same boundary condition represents a no-slip contact. Although any elastoplastic constitutive law is conveniently employed in MPM, for research purposes, isotropic linear hardening or softening is employed here. Compared with elastic perfect plasticity, isotropic linear hardening/softening introduces one additional hardening parameter H. Typically, in uniaxial situation, the stress-strain relationship is described by

$$\tilde{\sigma} = Y + H\tilde{\varepsilon}, \tag{3.12}$$

where $\tilde{\sigma}$ and $\tilde{\varepsilon}$ are the uniaxial stress and strain. $H = 0$ corresponds to elastic perfectly plastic material, $H > 0$ to linear strain hardening, while $H < 0$ to linear strain softening. The radial return mapping method for J_2 flow theory and objective stress rate (Belytschko *et al.*, 2000) are used. According to the theory of objective stress for large deformation, the tensor of Jaumann stress rate $\boldsymbol{\sigma}^{\nabla J}$ defined in Eq. (1.62) is rewritten here as
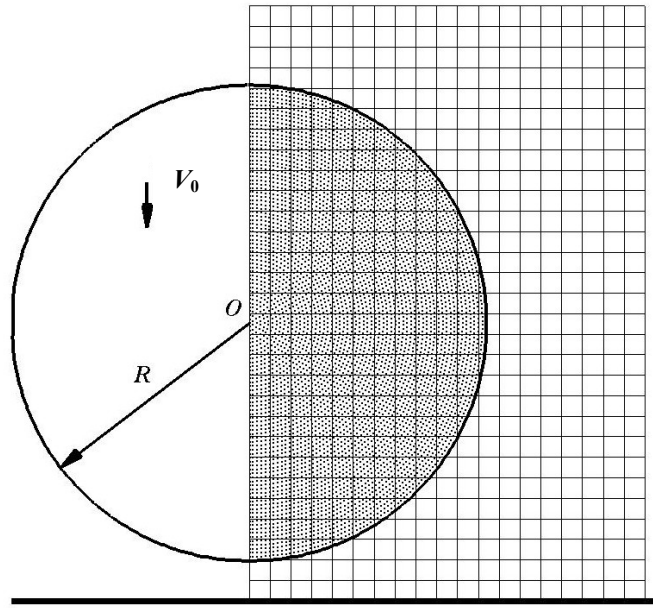
Fig. 3.2 The impact model between a spherical particle and a rigid wall. The particle is discretized into material points, embedded in the background computational mesh. The rigid wall is represented by fixed boundary conditions at the bottom of the computational mesh.

$$\boldsymbol{\sigma}^{\nabla J} = \dot{\boldsymbol{\sigma}} - \mathbf{W} \cdot \boldsymbol{\sigma} - \boldsymbol{\sigma} \cdot \mathbf{W}^T , \tag{3.13}$$

where $\dot{\boldsymbol{\sigma}}$ is the time derivative of the normal Cauchy stress tensor $\boldsymbol{\sigma}$, and $\mathbf{W}$ is the spin tensor which is given by

$$W_{ij} = \frac{1}{2}(\frac{\partial v_i}{\partial x_j} - \frac{\partial v_j}{\partial x_i}).$$
(3.14)

Here v_i, v_j are the components of velocity vector and x_i, x_j are the components of spatial coordinate. Due to the existence of the spin tensor $\mathbf{W}$, at time step t the stress tensor $\boldsymbol{\sigma}$ is updated by

$$\boldsymbol{\sigma}^{t+\Delta t} = \mathbf{Q}^{t+\Delta t} \cdot \boldsymbol{\sigma}^t \cdot (\mathbf{Q}^{t+\Delta t})^T + \Delta t(\boldsymbol{\sigma}^{\nabla J})^{t+\Delta t}$$
(3.15)

where Δt is the time increment, and $\mathbf{Q}$ is the incremental rotation tensor associated with the spin tensor $\mathbf{W}$ such that

$$\mathbf{Q} = \exp[\mathbf{W}\Delta t].$$
(3.16)

At each time step, the return mapping algorithm firstly projects the stress elastically (trial stress) beyond the yield surface and then uses a plastic corrector to return the trial stress onto the updated yield surface along a specified direction. The elastic trial stress, $(\boldsymbol{\sigma}^{t+\Delta t})^{(0)}$, is calculated by

$$(\boldsymbol{\sigma}^{t+\Delta t})^{(0)} = \mathbf{Q}^{t+\Delta t} \cdot \boldsymbol{\sigma}^t \cdot (\mathbf{Q}^{t+\Delta t})^T + \Delta t\mathbf{C}:\mathbf{D}$$
(3.17)

where $\mathbf{C}$ is the elastic modulus tensor given by Eq. (1.58) and $\mathbf{D}$ is the deformation rate tensor which is given by

$$D_{ij} = \frac{1}{2}(\frac{\partial v_i}{\partial x_j} + \frac{\partial v_j}{\partial x_i}).$$
(3.18)

The direction vector of the plastic corrector for the radial return is calculated by

$$\hat{\mathbf{n}} = \boldsymbol{\sigma}_{dev}^{(0)} / \left\| \boldsymbol{\sigma}_{dev}^{(0)} \right\|$$
(3.19)

where $\boldsymbol{\sigma}_{dev}^{(0)}$ is the deviatoric part of the trial stress $(\boldsymbol{\sigma}^{t+\Delta t})^{(0)}$. The standard small deformation radial return mapping iteration is then performed to locate the yield surface. Details of the iteration procedure can be found in APPENDIX III.

3.2.2 Convergence test

A convergence test is carried before studying the contact laws. As introduced in section 2.3, three kinds of mesh factors are possibly to affect the convergence: the number of material points, the number of cells of computational mesh, and the material point density, which is the average number of material points per unit cell of computational mesh. The mesh dependence of the Material Point Method in elastoplastic impact problems can be summarized below.

In our study, it is observed that the material point density, i.e. the average number of material points per cell of computational mesh, is the key factor that controls the convergence. Figure 3.3 shows the coefficient of restitution for an elastic perfectly plastic particle obtained using the MPM with different densities of material points. From point A to E in Fig. 3.3, the computational mesh is either maintained or refined. A faster refinement is used to increase the material point density. For the points A, B, C, D, and E in Fig. 3.3, the number of material points used are 5551, 21901, 87001, 346801, and 1384801, respectively. Convergence is achieved at the point D where about 94 material points are used in each computational cell to obtain the theoretical value of e=0.698. All of our following simulations in this chapter use this set of computational mesh and material points.

3.2.3 Accuracy test

According to Johnson (1985), for an elastic spherical particle at small deformation, the force-displacement relationship is given by Eq. (3.3). The displacement δ is related to time t by

$$t = \frac{\delta^*}{V_0} \int \frac{\mathrm{d}(\delta/\delta^*)}{\left[1-(\delta/\delta^*)^{5/2}\right]^{1/2}} \tag{3.20}$$

in which δ^* is the maximum δ given by

$$\delta^* = \left(\frac{15mV_0^2}{16R^{1/2}E^*} \right)^{2/5} .$$ (3.21)
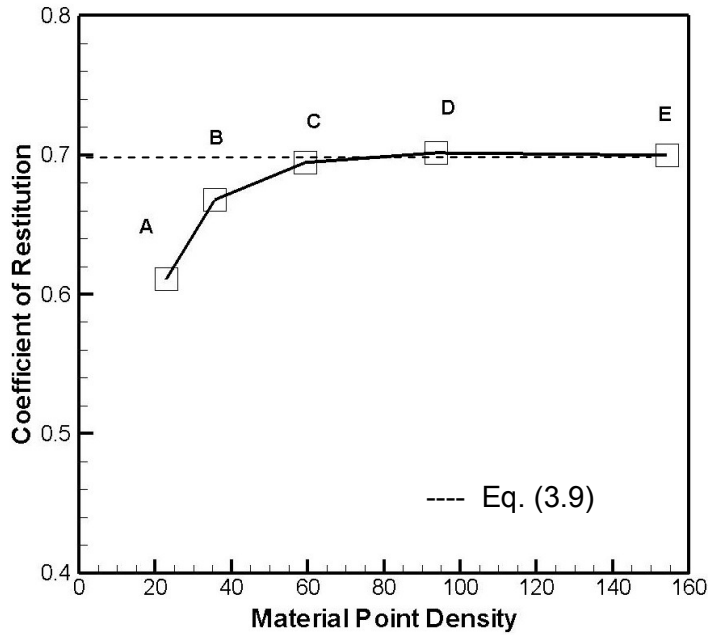
Fig. 3.3 Convergence test of the Material Point Method. Coefficient of restitution of elastic perfectly plastic impact obtained using MPM with different material point densities. For points A, B, C, D, and E, the number of material points used are 5551, 21901, 87001, 346801, and 1384801, respectively.

The corresponding maximum impact force F^* can be obtained from Eqs. (3.3) and (3.21). The total impact duration T^* is given by

$$T^* = 2.87(m^2 / RE^{*2}V_0)^{1/5} .$$ (3.22)

These analytical equations are used to further test the material point model. The following parameters are used: particle radius $R = 10$ mm, Young's modulus $E = 208$ GPa, Poisson's ratio $\nu = 0.29$, density $\rho = 7850$ kg/m^3. The impact velocity is selected to be $V_0 = 1$ m/s to meet the Hertz assumption of small deformation. Contact force F is computed by the sum of total nodal forces at the computational mesh excluding the nodes at the contact boundary. The displacement of the particle δ is defined as the displacement of the initial centre of the particle. The contact time t

starts when the kinetic energy of the particle starts to reduce and the total contact time T^* is the value of t when the kinetic energy recovers to its maximum. Figure 3.4 shows the comparison between the analytical and numerical results for F/F^* and δ/δ^* as functions of t/T^*. The discrete symbols are the numerical results. The analytical values of δ^*, F^*, and T^* calculated from Eqs. (3.21), (3.3), and (3.22) are 0.0179 mm, 2293.17 N, and 52.74 µs respectively, which can be compared with our numerical values of 0.0174 mm, 2350 N, and 51.32 µs obtained using the material point model.
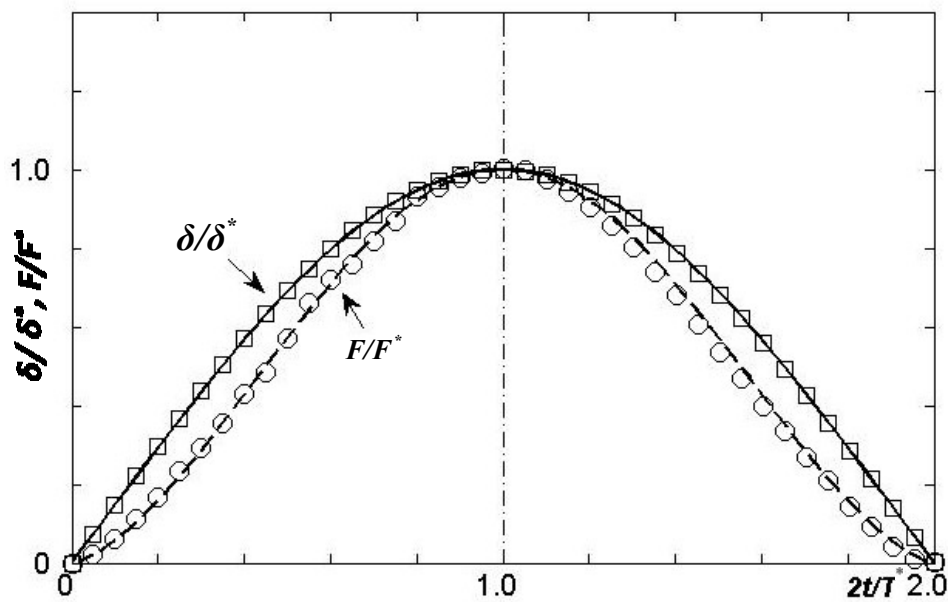
Fig. 3.4 The normalised contact force, F/F^*, and displacement, δ/δ^*, as functions of the normalised time, t/T^*, obtained from the analytical solution due to Johnson (1985) and numerically using the Material Point Method respectively. The discrete symbols are the numerical results.

In the numerical simulations, the energy dissipation due to both elastic waves and numerical dissipation was found to be 2.3% of the total initial kinetic energy, which is consistent with the findings by Hutchings (1979) that kinetic energy loss is less than 3% due to elastic waves. It is interesting to point out that the differences between the numerical and analytical values of δ^*, F^*, and T^* are 2.9%, 2.4%, 2.7% respectively, which are approximately the same as the total amount of energy dissipation. These

good agreements between the numerical and analytical results show the good accuracy of the material point model.

3.3 FORCE-DISPLACEMENT RELATION FOR SPHERICAL PARTICLES

This section presents the numerically obtained relation between the contact force and displacement for spherical particles. It is convenient to discuss the numerical results using non-dimensionalised forms. All the length scales are normalised by the initial radius, R, of the particle. All the velocities are normalised by V_y defined through Eq. (3.4) and the contact force is normalised by F_y defined by Eq. (3.6).

3.3.1 Spherical particles of elastic perfectly plastic material

Simulations of particle impact were carried out on an elastic, perfectly plastic solid using three different impact velocities of V_0/V_y = 40, 1200, 4000 for particles with E^* = 227MPa, 321MPa, 227GPa, 321GPa, and E^*/Y = 168, 238, 336. The contact force-displacement curves are shown in the left column of Fig. 3.5. The right column of Fig. 3.5 gives examples of the particle at maximum deformation for the corresponding impact velocity. The hollow symbols represent cases with low values of Young's modulus while the solid symbols represent cases with high values of Young's modulus. An immediate observation from all the cases is that the normalised contact law depends on the ratio of E^*/Y rather than on E^* and Y independently. Despite the large difference in Young's modulus, the normalised contact law remains the same as long as the ratio of E^*/Y and the impact velocity, V_0/V_y, remain constant. This can be understood through dimensional analysis. The area under the elastoplastic loading curve is always equal to the initial kinetic energy such that

$$\frac{1}{2}mV_0^2 = \int_0^{\delta_{max}} Fd\delta \tag{3.23}$$

in which δ_{max} is the maximum displacement. For the velocity required for the onset of yielding V_y, there is

$$\frac{1}{2}mV_y^2 = \int_0^{\delta_y} Fd\delta \; . \tag{3.24}$$

The force-displacement curve of an elastoplastic impact contains an elastic part before δ reaches δ_y. Subtracting Eq. (3.23) by Eq. (3.24) leads

$$\frac{1}{2}mV_0^2 - \frac{1}{2}mV_y^2 = \int_0^{\delta_{max}} Fd\delta - \int_0^{\delta_y} Fd\delta = \int_{\delta_y}^{\delta_{max}} Fd\delta \; . \tag{3.25}$$

Using the definitions of V_y, F_y and δ_y through Eqs. (3.4)-(3.7), Eq. (3.25) is equivalent to

$$\left(\frac{V_0}{V_y}\right)^2 = 1 + \int_{\delta_y}^{\delta_{max}} \left(\frac{2F}{mV_y^2}\right)d\delta = 1 + \frac{5}{2}\int_1^{\delta_{max}/\delta_y} \left(\frac{F}{F_y}\right)d\frac{\delta}{\delta_y}$$

$$= 1 + \frac{2}{5}\left(\frac{E^*}{Y}\right)^2 \int_{(4/5)^2\pi^2(E^*/Y)^{-2}}^{\delta_{max}/R}\left(\frac{F}{F_y}\right)d\frac{\delta}{R} = 1 + \frac{2}{5}\left(\frac{E^*}{Y}\right)^2 \int_{6.3(E^*/Y)^{-2}}^{\delta_{max}/R}\left(\frac{F}{F_y}\right)d\frac{\delta}{R} \; . \tag{3.26}$$

The non-dimensional groups are V_0/V_y, E^*/Y, F/F_y, and δ/R. For a force-displacement curve, given a value of displacement δ, there is only one corresponding force F. Therefore, it is can be seen from Eq. (3.26), V_0/V_y and E^*/Y completely determine the relationship between δ/R and F/F_y, which is consistent to Fig. 3.5.

In Fig. 3.5(a) where the relative impact velocity V_0/V_y is set as 40, the deformations are very small and the contact force-displacement behaviour falls into the scope of the theories due to Thornton (1997) and Li *et al.* (2002). The loading curves are firstly elastic and then become more linear but slightly concave after yield. The elastic unloading curves still follow Eq. (3.3) but with a different value of $\tilde{R}$. It is interesting to observe that the normalised maximum contact force, F_{max}/F_y, remains constant for all the cases. On the other hand, both loading and unloading curves become stiffer with the increasing of E^*/Y. This indicates that the maximum displacement δ_{max}/R, the residual displacement, δ_{res}/R, and the relative recovering displacement during unloading, $(\delta_{max} - \delta_{res})/R$, all decrease as E^*/Y increases.
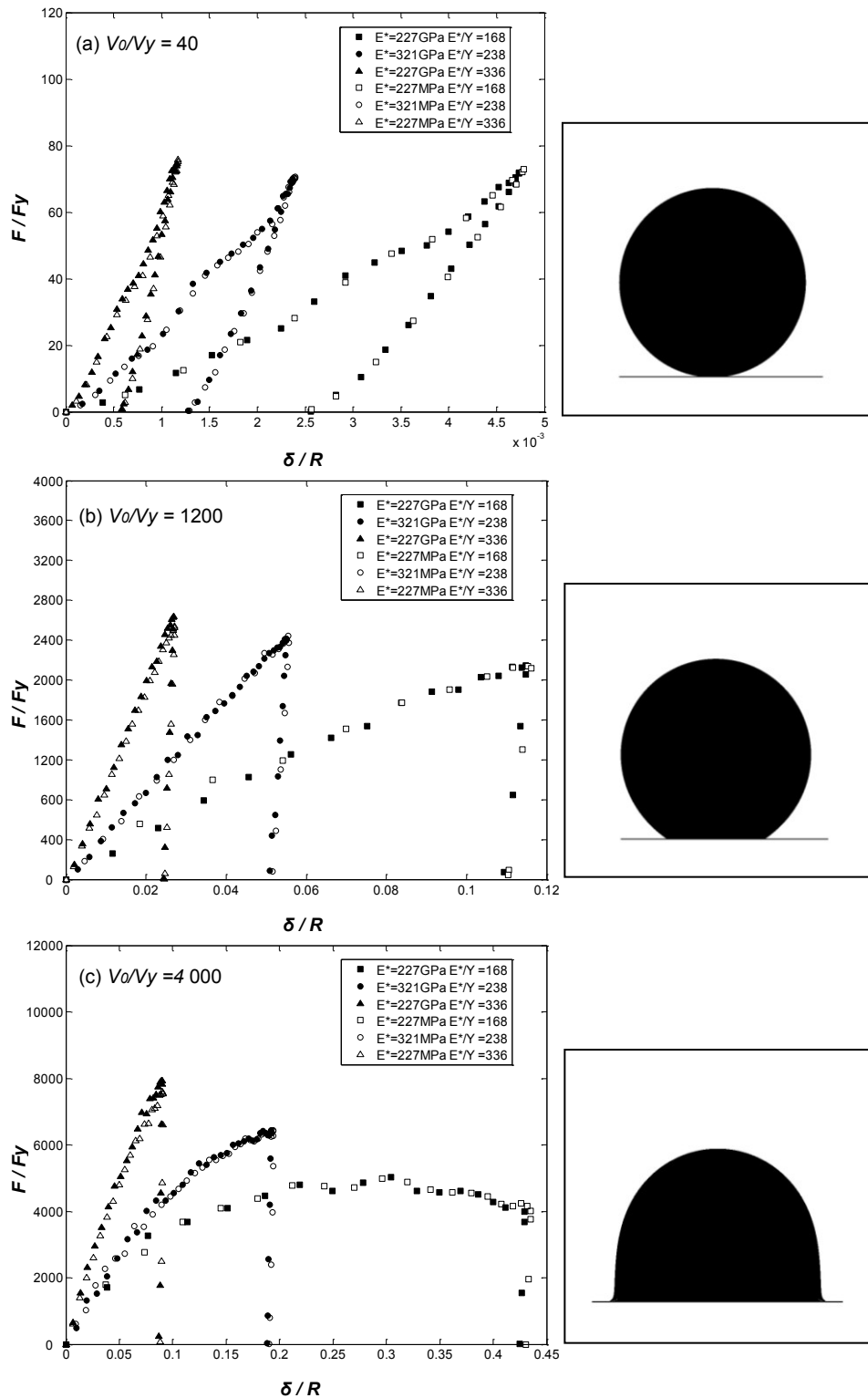
Fig. 3.5 Impact of elastic perfectly plastic spherical particles for different impact velocities and material properties. (a) $V_0/V_y = 40$, (b) $V_0/V_y = 1200$ and (c) $V_0/V_y = 4000$. The left column shows the normalized force-displacement curves, where solid symbols show cases with high Young's modulus and hollow symbols show cases with low Young's modulus. Different shapes of the symbols indicate different ratios of E^*/Y. The right column shows examples of the particle at the maximum possible deformation for the three impact velocities.

In Fig. 3.5(b) where the relative impact velocity V_0/V_y is set as 1200, the deformations are much larger than those in Fig. 3.5(a). During the loading, the loading curves continue ascending but much more slowly comparing to those in Fig. 3.5(a). The loading curves are still roughly linear but become slightly convex. The unloading curves are still elastic but much stiffer than those in small deformations. Unlike small deformations, a clear descending trend is observed for the maximum normalised contact force, F_{max}/F_y, as the ratio of E^*/Y decreases. In Fig. 3.5(c) where the relative impact velocity V_0/V_y is set as 4000, the deformations are very large. The loading curves are clearly convex. For the cases with $E^*/Y = 168$, the contact force remains almost constant for a long period as the particle centre continues to approach the wall. It reaches its maximum at $\delta/R = 0.3$ and starts to decrease gently long before the particle rebounds. From all our simulations which are not presented here, it seems to be a general conclusion that the contact force would drop before the particle rebounds as long as the impact deformation is larger than $\delta/R = 0.3$. Similar behaviours were observed by Adams *et al.* (2004). Another interesting observation in our numerical results is that if the impact deformation is larger than $\delta/R = 0.3$, the total contact time increases with increasing impact velocity, which is shown in Fig. 3.6. These numerical findings are somehow against our common sense and may be caused by the drop in the contact pressure at large deformation (Mesarovic and Fleck 2000).

A general observation of the numerical results is that the normalized contact law can be uniquely determined from E^*/Y and V_0/V_y at all levels of deformations. Two points on the force-displacement curve are of importance: the loading-unloading turning point and the end point of unloading curve. The force and displacement values at these two points are plotted against E^*/Y and V_0/V_y in Fig. 3.7. Figure 3.7(a) shows the normalized maximum contact force F_{max}/F_y as a function of the relative impact velocity, V_0/V_y, for different values of E^*/Y. It can be observed from the figure that F_{max}/F_y increases linearly with V_0/V_y for large values of E^*/Y, which correspond to small deformations. The relationship becomes non-linear as E^*/Y gets smaller. If $V_0/V_y < 100$, then F_{max}/F_y becomes independent of E^*/Y, which is

consistent with that shown in Fig. 3.5(a). If the value of V_0/V_y is high, then F_{max}/F_y increases with E^*/Y. This can be interpreted by the level of deformation. For a large E^*/Y, very small deformation is obtained even at large values of V_0/V_y. Therefore, the normalized maximum force behaves more elastically, showing a more linear relationship between F_{max}/F_y and V_0/V_y.
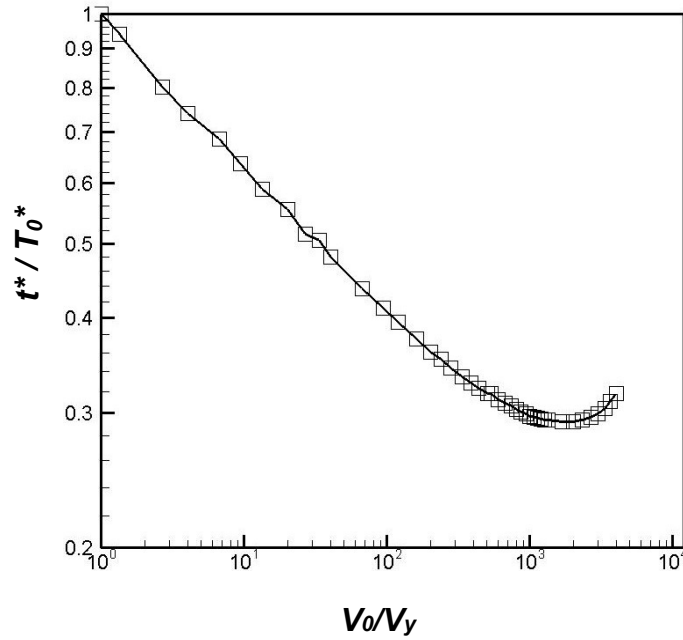
Fig. 3.6 Normalised total contact time t^*/T_0^* as a function of relative impact velocity V_0/V_y for the spherical particle shown in Fig. 3.5 with $E^*/Y = 168$. Total contact time is normalized by the total contact time T_0^* at $V_0 = V_y$.

Figure 3.7(b) shows the normalized maximum displacement, δ_{max}/R, and normalized residual displacement, δ_{res}/R, as functions of the relative impact velocity, V_0/V_y, for different values of E^*/Y. The results are shown in groups of two lines. Each group corresponds to a different value of E^*/Y. In each group, the upper line is δ_{max}/R and the lower one is δ_{res}/R. Figure 3.7(c) shows a zoom-in for large values of E^*/Y. A striking linear relationship between the characteristic displacements and the impact velocity is observed. In details, the difference between δ_{max}/R and δ_{res}/R increases very slowly along with the increasing of V_0/V_y. For a same relative velocity value

V_0/V_y, the value of $(\delta_{max} - \delta_{res})/R$ is the largest in the a medium E^*/Y. This is because the elastic recovery unloading displacement $(\delta_{max} - \delta_{res})/R$ is determined by the elastic component of the deformation history. For a small E^*/Y, the elastic component is relatively small and therefore $(\delta_{max} - \delta_{res})/R$ is small. For a large E^*/Y, although the elastic component is relatively large and the ratio between elastic recovery unloading displacement and the total displacement is large. However, the value of $(\delta_{max} - \delta_{res})/R$ is still small because the value of the total displacement is very small.
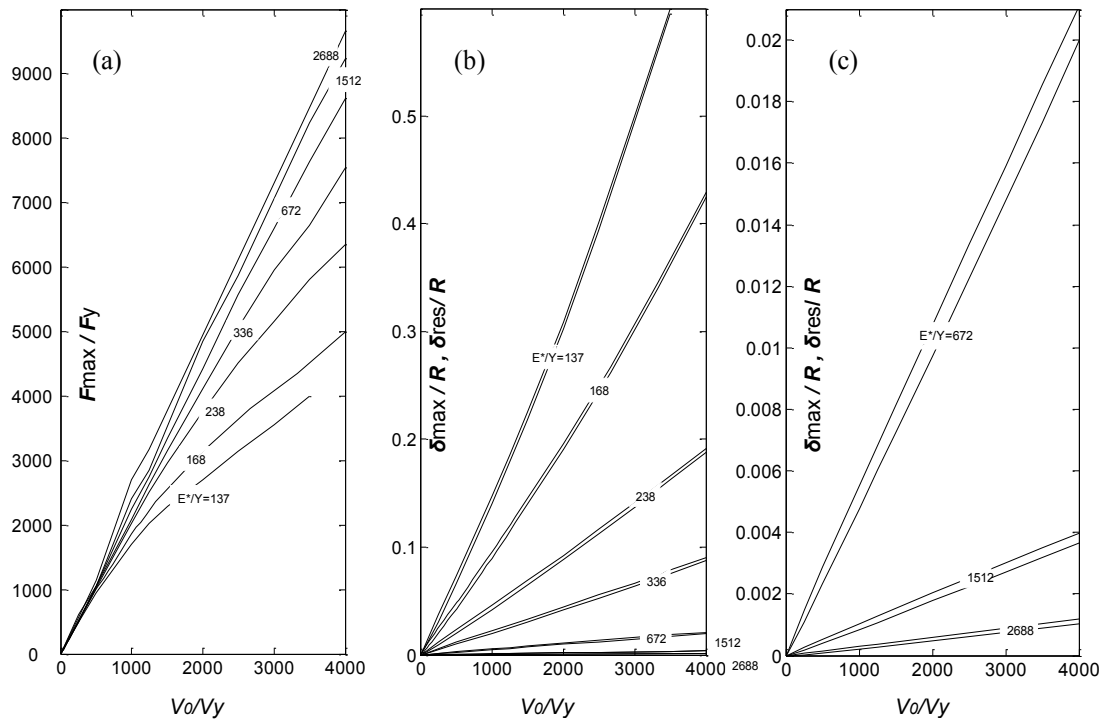
Fig. 3.7 Characteristic points of contact law for elastic perfectly plastic impact of spherical particles. (a) Normalized maximum contact force as a function of the relative impact velocity V_0/V_y for different values of E^*/Y, (b) normalized maximum and residual displacements as functions of V_0/V_y for different values of E^*/Y. For each value of E^*/Y, the upper line shows the normalized maximum displacement and lower line shows the normalized residual displacement, and (c) a zoom-in of the small deformation part of Fig. 3.7 (b).

3.3.2 Effect of strain hardening and softening

A large number of particles undergo strain hardening/softening in the plastic impact. In this section, the strain hardening/softening effect is taken into account. For simplicity and research purpose, the linear isotropic hardening/softening described by Eq. (3.12) is employed here. Figure 3.8 shows the contact force-displacement curves at three different impact velocities for different values of H. Similar to Fig. 3.5, the numerical results are presented in a normalised form. In order to focus on the effect of H, the value of E^*/Y is fixed at 168. At the low relative impact velocity of $V_0/V_y =$ 40 (hence small deformation), it can be observed from Fig. 3.8(a) that the effect of strain hardening or softening on the contact law is relatively small. Similar to Fig. 3.5(a), the loading curves can be well approximated as straight lines but slightly concave. As the deformation is increased, the force-displacement curves are affected significantly by the value of H as shown in Fig. 3.8(b). The maximum contact force decreases and the maximum displacement increases as H/Y decreases. However the loading curves can still be roughly approximated by straight lines (but slightly convex). At very large deformation as shown in Fig. 3.8(c), the contact law becomes strongly non-linear and H has a major effect on the contact force-displacement curve. If the normalized displacement δ/R exceeds 0.3 then the particle continues to deform toward the rigid wall after the contact force has reached its maximum value.

To summarise, for small deformation impact with significant plasticity which covers a wide range of applications, the loading curves can be regarded as linear while the unloading curves are elastic. The effect of strain hardening or softening can be ignored and the contact law assuming elastic perfectly plastic material can be used. As the deformation reaches intermediate level, the contact law is significantly affected by both the strain hardening and the ratio of the effective Young's modulus to yield strength. The loading curves can however still be roughly approximated as linear. As the deformation gets larger, the loading curves become strongly non-linear and at very large deformation ($\delta/R > 0.3$), the contact law behaves like the stress-strain curve for elastoplastic solid.
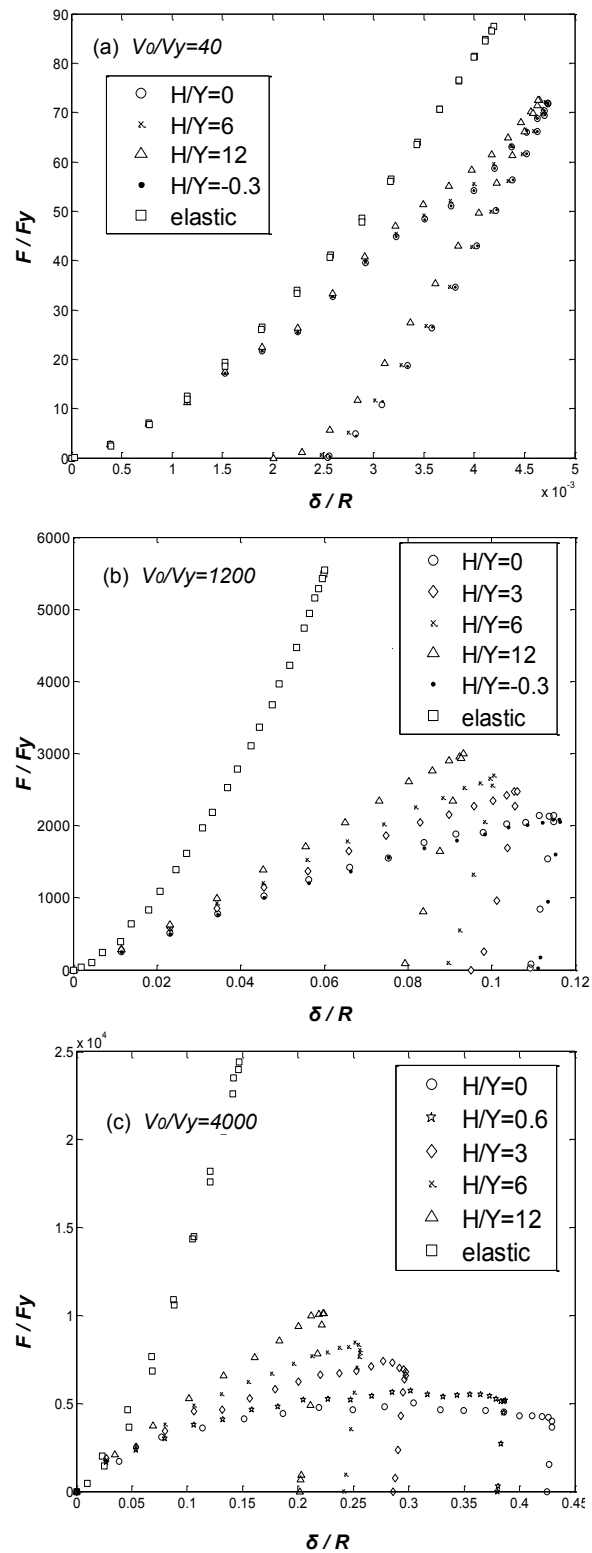
Fig. 3.8 Normalized force-displacement curves for the impact of plastic isotropic linear hardening spherical particles. $E^*/Y = 168$. (a) $V_0/V_y = 40$, (b) $V_0/V_y = 1200$, and (c) $V_0/V_y = 4000$. Elastic contact law is also shown for comparison.

3.4 COEFFICIENT OF RESTITUTION FOR SPHERICAL PARTICLES

3.4.1 Elastic perfectly plastic particles

As introduced in section 3.1.2, several theoretical and numerical models of the coefficient of restitution are developed for the impact of elastic perfectly plastic particles. Wu *et al.* (2003) showed that the coefficient of restitution can be uniquely determined from V_0/V_y for small deformation impact, and from V_0/V_y and E^*/Y for large deformation impact. The boundary between the small and large deformations is defined by

$$\frac{V_0/V_y}{\left(E^*/Y\right)^2} = 0.008 \,. \tag{3.27}$$

The coefficient of restitution reflects the area between the loading and unloading curves. Our numerical results in section 3.3 show that the loading and unloading curves can be uniquely determined from V_0/V_y and E^*/Y for all levels of deformations. These numerical results are therefore in general agreement with the conclusion by Wu *et al.* (2003). The discrete symbols in Fig. 3.9 shows our numerically obtained coefficient of restitution, e, as a function of the relative impact velocity V_0/V_y for elastic perfectly plastic particles. It can be observed from the figure that there are three zones of different behaviours. In Zone I, the deformation is small. The contact pressure increases as the particles approach each other and the e-V_0/V_y curve follows the power law with a varying exponent. In Zone II, full plasticity is reached during the impact when the maximum contact pressure P_0 remains as $2.85Y$, the e-V_0/V_y curve follows the power law with a fixed exponent of $-1/4$. In Zone III, the e-V_0/V_y curve also follows the power law with a fixed but greater exponent. In this zone e also depends on E^*/Y in addition to V_0/V_y (the results shown in the figure are for $E^*/Y = 168$).
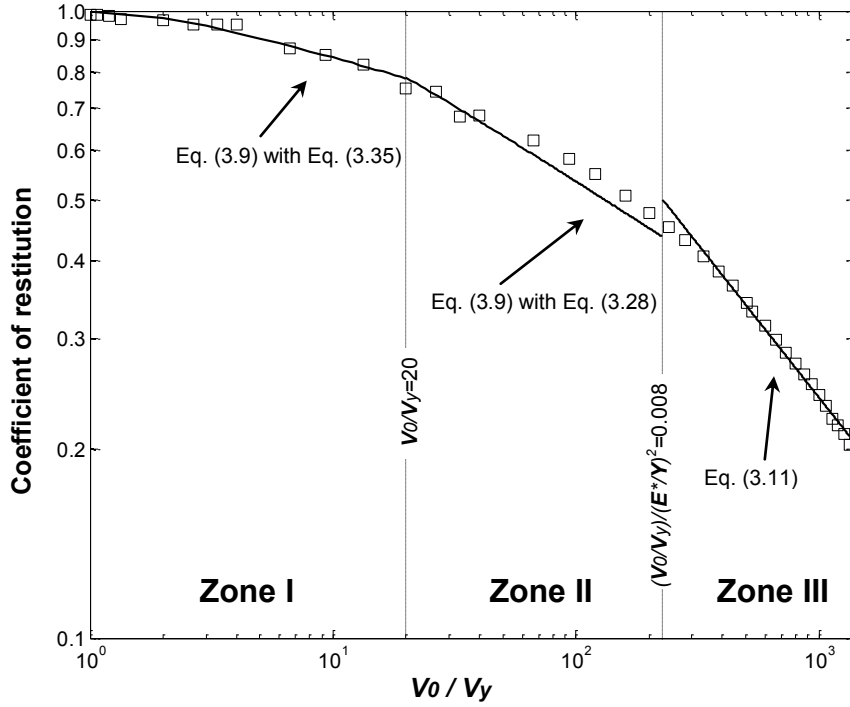
Fig. 3.9 The coefficient of restitution as a function of the relative impact velocity for impact between spherical particles of elastic perfectly plastic materials. Square symbols: numerically obtained by Material Pointed Method. Solid lines: analytical expressions. Dashed lines: boundaries between different zones.

These results are consistent with previous understandings. For Zone II, using $P_0 = 2.85Y$ in Eq. (3.10) gives

$$\bar{V}_y = 4.23 V_y,\tag{3.28}$$

which is substituted into Eq. (3.9) and plotted in Fig. 3.9 (the solid line in Zone II). For Zone III, Eq. (3.11) is plotted in the figure (the solid line in Zone III). The boundary between Zone II and Zone III is given by Eq. (3.27) and also shown in the figure. It can be seen that the analytical expressions agree with our numerical results very well.

The author is not aware of any significant discussion about Zone I in the literature. In fact this is an important zone because most of the applications fall into this zone of small impact velocity and localised plasticity. In this zone, the maximum contact pressure P_0 in Eq. (3.10) increases as the particle deforms into the rigid wall.

Mestrovic and Fleck (2000) showed that the boundary between the elastic-plastic and full plastic impacts is given by

$$aE^* / RY \approx 50 \ .$$

(3.29)

Unfortunately, Eq. (3.29) contains an intermediate variable - the radius of the contact area a, and is therefore rather inconvenient to use. Thornton (1997) suggested the following relationship between the maximum contact force F_{max} and the coefficient of restitution e:

$$e^2 = \frac{3F_{max}^2}{5E^* amV_0^2} \ .$$

(3.30)

However the force-displacement curve suggested by Thornton (1997) is too soft (Vu-Quoc and Zhang, 1999) because the maximum contact pressure, P_0, was taken as $1.6Y$ at the onset of yielding. On full plasticity, Eq. (3.30) can be modified by taking $P_0 = 2.85Y$ to give

$$e^2 = \frac{9.51F_{max}^2}{5E^* amV_0^2} \ .$$

(3.31)

Our numerical results in Fig. 3.7(a) indicate that when the maximum contact pressure P_0 just reaches its maximum value $2.85Y$, the relative impact velocity V_0 / V_y is still relatively small and the normalized maximum force F_{max} / F_y is independent of E^* / Y. Under these conditions, the numerical results can be approximated as

$$\frac{F_{max}}{F_y} \approx 2\frac{V_0}{V_y} \ .$$

(3.32)

Combining Eqs. (3.29), (3.31) and (3.32) and using Eqs. (3.4)-(3.6), we find that Zone I should terminate at

$$e \approx 0.79 \ .$$

(3.33)

Substituting Eq. (3.33) into Eq. (3.9), and using $P_0 = 2.85Y$ in Eq. (3.10), the boundary between Zone I and Zone II can be determined as

$$V_0 / V_y \approx 20 \tag{3.34}$$

which is shown in Fig. 3.9. When deriving Eqs. (3.31) and (3.34), the mean contact pressure P_m is used instead of the maximum contact pressure P_0 because the elastic part of the contact pressure can be ignored on full plasticity. In Zone I, $\bar{V}_y$ in Eq. (3.9) varies from slightly less than V_y at $V_0 = V_y$ to about $4.23V_y$ at $V_0 = 20V_y$. We propose the following expression for $\bar{V}_y$ in Zone I:

$$\bar{V}_y = 0.96\sqrt{(V_0 / V_y)} \times V_y \tag{3.35}$$

which is substituted into Eq. (3.9) and plotted in Fig. 3.9. A complete set of analytical expressions for the coefficient of restitution has therefore been obtained.

3.4.2 Effect of strain hardening and softening on coefficient of restitution

Figure 3.10 shows the coefficient of restitution as a function of the relative impact velocity V_0 / V_y for different values of the hardening parameter H and E^* / Y. The results for elastic perfectly plastic particle are also shown in the figure for comparison. It can be seen that for small impact velocity, the coefficient of restitution e is insensitive to the hardening parameter H. At higher impact velocity however, the hardening parameter has a strong effect on e. A higher value of H represents stronger strain hardening and leads to less energy loss during the impact, hence a higher value of the coefficient of restitution at the same impact velocity. The numerical results shown in Fig. 3.10 therefore follow the common sense. Unlike elastic perfectly plastic particles, with strain hardening, the coefficient of restitution cannot be uniquely determined from V_0 / V_y even at small impact velocity. A different value of E^* / Y leads to significantly different values of the coefficient of restitution. It is difficult to place any analytical framework over the numerical results shown in Fig 3.10.
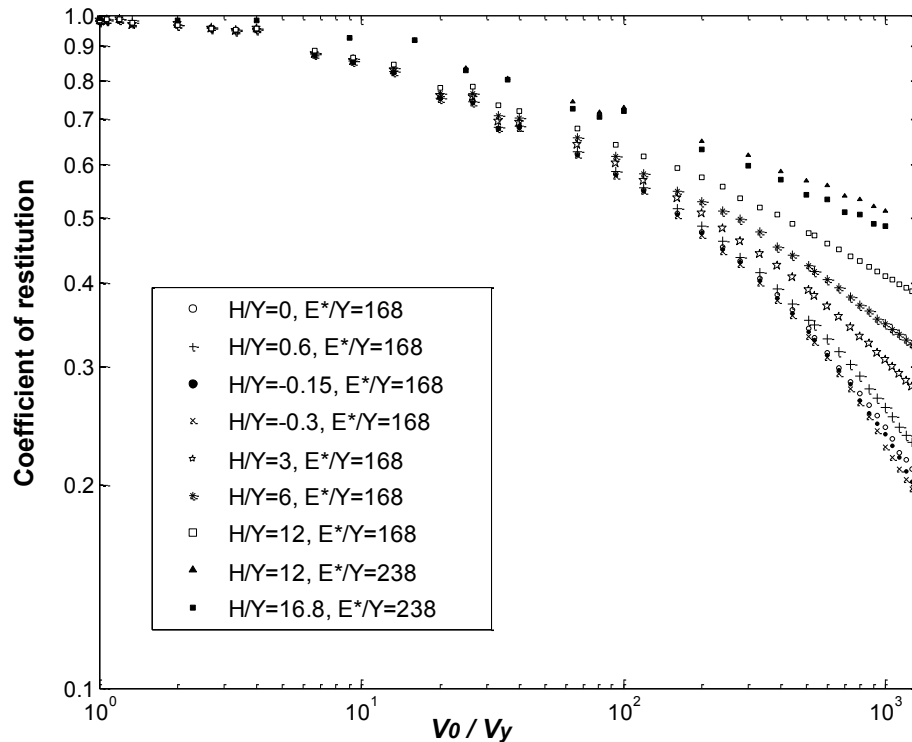
Fig. 3.10 Coefficient of restitution as a function of the relative impact velocity for different levels of strain hardening and effective modulus.

3.5 PARTICLES OF IRREGULAR SHAPE OR HETEROGENEOUS MATERIALS

In most DEM simulations, spherical particles are often bonded together to represent irregular particles. This approach is inappropriate if most of the particles are irregular. For example pharmaceutical powder formulations usually consist of a mixture of soft and hard particles with irregular shapes. In addition, tablets or pellets can be film coated for functional reasons, elegance, as well as to improve mechanical integrity. There has been very little work on contact laws for non-spherical particles. The Discrete Element Method (DEM) would be very useful if it could be used in applications in which the particles are either of irregular shape or made of heterogeneous materials. For these problems the contact law can only be obtained numerically. The question is how sensitive the contact law is to material and geometry details of the particles.
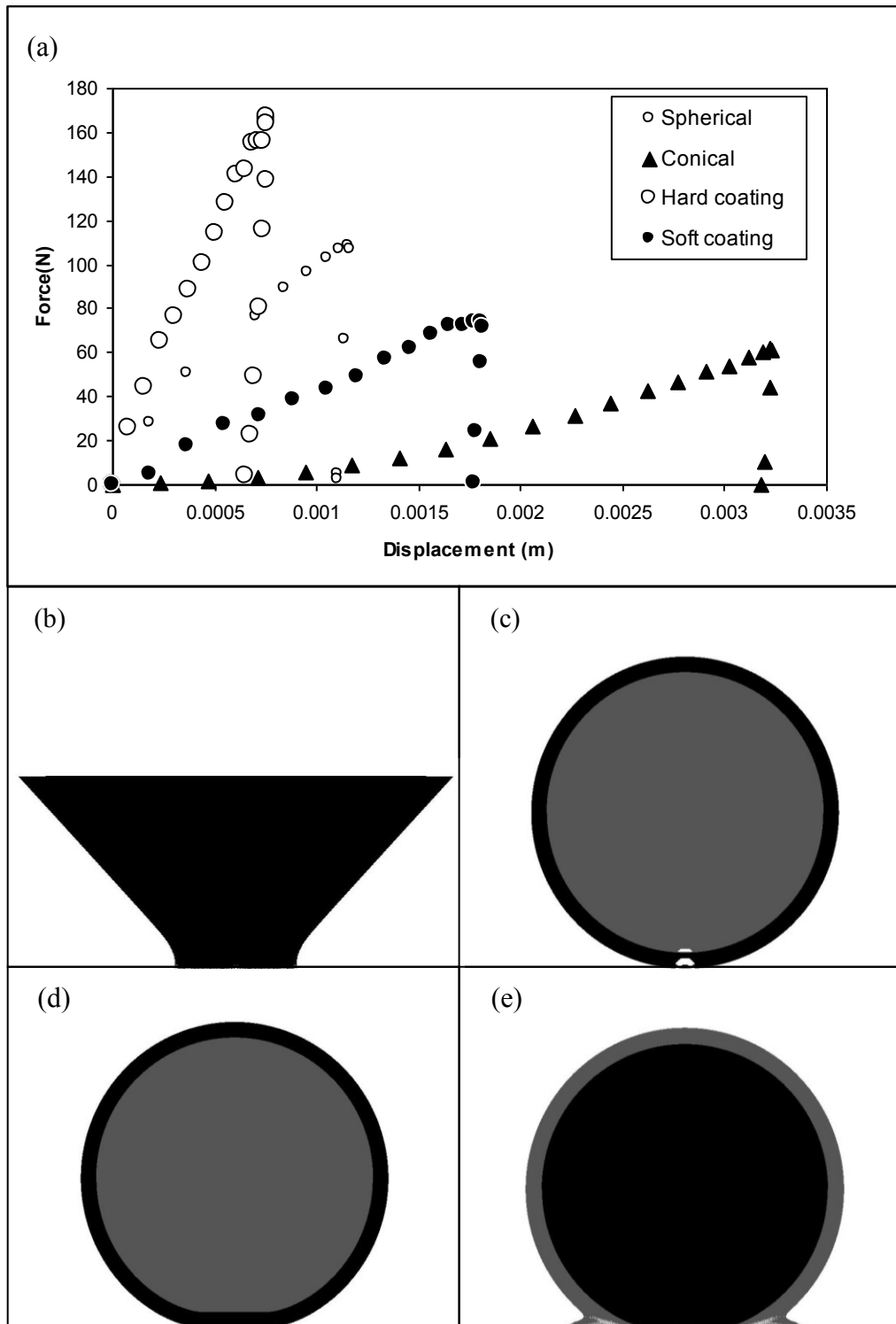
Fig. 3.11 Impact of particles of conical shape and heterogeneous materials. All particles share the same volume. The impact velocity is 2.88 m/s. $E^*/Y = 168$. Other parameters are the same as the case shown in Fig 3.4. (a) Force-displacement curves, hard coating: the Young's modulus of the coating is 10 times of the core, the soft coating: the Young's modulus of the coating is 0.1 times of the core. (b) conical particle at its maximum deformation, (c) locations where yield is initialized in coated particle, and (d, e) hard and soft coated particles at their maximum deformation.

Figure 3.11 compares the contact laws for particles of different geometries and materials. All the particles have the same impact velocity and volume. The solid triangle symbols in Fig. 3.11(a) show the force-displacement curve of a conical particle made of elastic perfectly plastic material (shown at its maximum deformation in Fig. 3.11(b)). It can be compared to the small hollow circles which represent the force-displacement curve of a spherical particle of the same material. It can be clearly seen that the contact law of the conical particle is very different from that of the spherical one. In fact the two contact laws are very different even at small deformation as suggested by Johnson (1985). The onset of yield for a conical particle occurs at the tip of the cone rather than inside the particle and the curvature of the conical particle near the contact area is always negative as shown in Fig. 3.11(b). It is difficult to obtain the contact law analytically for all the possible geometries. Furthermore non-normal impact is very common in irregular particulate systems, which is impossible to deal with analytically. Figure 3.11(a) also shows contact laws for a particle containing an outer layer which has a different material property, i.e. a coated pellet. The thickness of the coating layer is one tenth of the particle radius. The core and the coated layer share the same value of $E^* / Y = 168$. In the hard coating case, the Young's modulus of the coating is 10 times that of the core material. In the soft coating case, the Young's modulus of the coating is 0.1 times that of the core material. Significant differences can be observed in the force-displacement contact laws. For the particle with hard coating, the coating layer dominates the impact behaviour as can be seen from the deformation in Fig. 3.11(d). For the particle with soft coating however, both the coating and the core play an important role to the energy dissipation and the contact law shows a complicated behaviour.

3.6 SUMMARY

This chapter presents a comprehensive study for the contact laws between solid particles taking into account of the effects of plasticity, strain hardening and softening, very large deformation, non-spherical geometry and material heterogeneity. The study takes advantage of the Material Point Method and demonstrates that the method is efficient and reliable when solving impact problems involving all these factors. The

numerical studies revealed some new understandings about the frictionless normal impact behaviour of particles. For example, it is shown that the contact law for elastic perfectly plastic spherical particles can be uniquely determined from the relative impact velocity and normalised Young's modulus. The contact law at very large deformation shows a perfectly plastic behaviour. Strain hardening can be ignored for small deformation impact. A complete analytical framework is possible to calculate the contact law as well as the coefficient of restitution for elastic perfectly plastic spherical particles.

In the case of non-spherical particles or particles with strain hardening or softening behaviour, it is difficult to develop analytical contact laws. The use of numerical contact laws for solving practical problems is discussed in the context of discrete element simulation of powder flow, where a two-step approach is proposed, i.e., a numerical contact law is calculated using the Material Point Method. The reliability of the Material Point Method makes this a routine task. Secondly the numerical contact law can be directly fed into the discrete element simulation.

CHAPTER 4

IMPACT FAILUE OF BRITTLE PARTICLES

The failure of brittle particles through multi-crackings could be very difficult to simulate by conventional FE analysis. Based on the Material Point Method, this chapter is to develop a simple and robust model in order to study the failure of brittle particles.

4.1 BACKGROUND

4.1.1 Experimentally observed failure patterns

In this chapter, we focus on the brittle failure of a single particle during impact. A continuum particle undergoing brittle failure is transformed into a discrete assembly because of the development of multiple cracks. Extensive experimental research has been conducted during the past decades. Due to the high speed and violent nature of the damage and failure process of brittle materials, experiment observations are normally restricted to the final states of the particles. In summary the failure patterns observed experimentally can be divided into three categories as shown in Fig. 4.1. Patten I is a small damage concentrating on a ring of material surrounding the contact area. This is normally referred to as Hertzian ring. After impact, as shown in Fig. 4.1(a), sometimes secondary ring cracks may be formed within the Hertzian ring. If the impact velocity increases, a cone crack linking with the meridian cracks, i.e., meridian cracks with a missing cone as shown in Fig. 4.1(b), are formed, this is referred to as Pattern II. The particle is divided into two or several pieces along the meridian planes. Pattern III refers to oblique cracks, as shown in Fig. 4.1(c), which divide the particle into small pieces with or without the help of the meridian cracks. The left hand side of Fig. 4.1(c) shows the oblique cracks formed at medium impact velocities for large particle as observed by Salman and Gorham (2000). The right

hand side of Fig. 4.1(c) shows particles at large impact velocities, with firstly meridian cracks and then oblique cracks developing and dividing the particle into small pieces (Wu *et al*., 2004).

[1]
(a) Pattern I: Hertzian fracture system ring crack

[1]

[2]
(b) Pattern II: Meridian plane cracks with missing cone

[1]

[2]
(c) Pattern III: Oblique cracks and small fragments
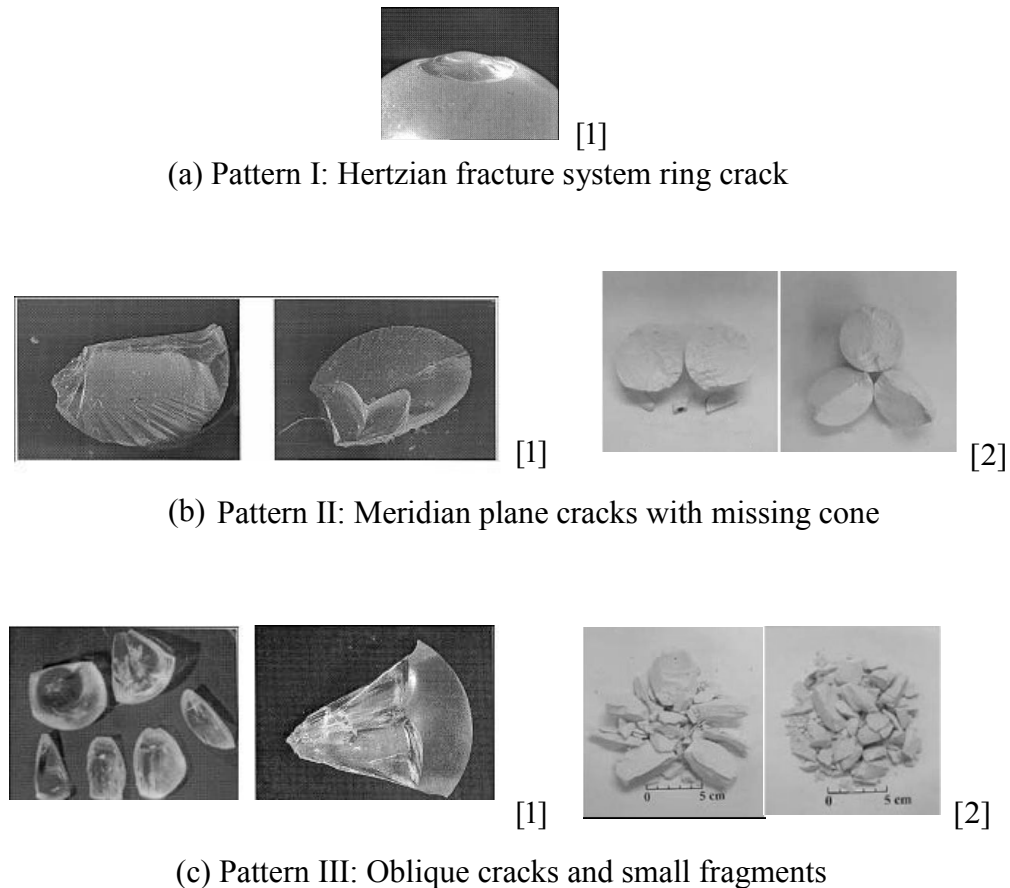
Fig. 4.1 Three types of experimentally observed failure patterns of brittle particles upon impact. (Reproduced from [1] Salman and Gorham, 2000, and [2] Wu *et al*., 2004.)

The patterns shown in Fig. 4.1 are in general agreements with other experimental observations. Arbiter *et al*. (1969) studied the fracture patterns by impact of sand-cement spheres to the ground and observed Hertzian ring and cone cracks after low velocity impact and meridian cracks after higher velocity impact. The Hertzian ring and cone crack were also observed after the impact of soda-lime glass spheres

(Salman and Gorham, 2000). For different materials subject to higher impact velocities, splitting failures by meridian cracks were observed by Shipway and Hutchings (1993) and by Andrews and Kim (1998). Salman and Gorham (2000) claimed that the meridian cracks only occur in soda-lime glass particles of very small sizes at very high impact velocities while the oblique cracks are induced in large particles. Wu *et al*. (2004) categorised twelve failure patterns in their double impact experiment using plaster spheres. Hertzian cone cracks and meridian cracks were found in low kinetic energy impact. Small fragments and powders at higher kinetic energy impact were considered to occur due to the coalescence of oblique and meridian cracks.

4.1.2 Modelling brittle impact failure

The existing models for brittle failure can be divided into two categories – those based on the statistical strength theory and those based on fracture mechanics. Crack problems naturally fall into the field of fracture mechanics. Stresses at a crack tip are theoretically infinite and they can be handled using the concepts of stress intensity factor or energy release rate. A large amount of literature exists on fracture mechanics models. However, the fracture mechanics approach can only predict crack propagation, not crack initiation. In a numerical model small initial cracks have to be placed into a material. The predicted failure pattern strongly depends on the assumed pattern of the initial cracks and is often unrealistic. On the other hand models based on the strength theory, as adopted in this study, have been shown to be successful in various applications. The brittle failure of particles during impact has been modelled extensively in the past decades. Most of the previous studies used the Finite Element Method (FEM). Many efforts were focussed on the modelling of the fragmentation process, which is somewhat inconsistent with the continuum description used in the FEM. Tvergaard (1982) developed an element vanishing technique which removes an element that meets the failure criterion in the sense that this element no longer contributes to the virtual work integral of the FE weak form. The element vanishing method has been used in modelling the failure of both brittle materials (Guo, 1995)

and porous ductile materials (Needleman and Tvergaard, 1987). Xu and Needleman (1994) developed a mesh splitting technique to simulate crack propagation and branching. As the failure criterion is reached at a finite element node, the node is duplicated and separates according to the cohesive crack constitutive law. Based on this method, an elaborate model was built up by Camacho and Ortiz (1996). By involving the boundary search and contact search algorithm, the phenomenon of fragmentation, including crack opening, growing, and healing, as well as multiple crack coalescence and frictional contact between fragments, were simulated by Camacho and Ortiz (1996). Espinosa (1998) simplified the model of Camacho and Ortiz (1996) in order to account for material microstructures. Such node duplicating technique is widely used to model brittle failures (e.g. Batra and Lear, 2004). However, as multiple cracks appear, the mesh distortion and separation can be excessive and adaptive mesh refinement is required . The complexity in the numerical procedure has severely limited the applications of the computer modelling in practical problems.

On the other hand, various discrete numerical methods have been used to model brittle failure during impact. Molecular Dynamics (MD) is a straightforward and reliable method of modelling the failure of materials (e.g. Wagner and Holian, 1992). However, it is difficult to model structures of any real size in an MD model because of the limitation of computational capability. A generalized MD method was suggested by Smith and Srolovitz (1995, 1996), who represented a cluster of atoms as a particle and assumed a potential to govern the particle movements. Although the impact induced crack initialization and propagation are observed, the validity conditions of their inter-particle potential are still uncertain. There are also efforts trying to apply the Discrete Element Method (DEM) to model the failure of brittle materials. Potapov and Campbell (1994, 1997, and 2001) employed this method and studied the failure mechanisms during impact. It is possible to use DEM to study the complicated failure patterns and fragmentation (Kadono and Arakawa, 2002; Cheong and Reynolds, 2004). However, contact laws and failure criterions used in DEM are not always established on solid physical basis and complex material properties cannot

be readily modelled. It has been pointed out that the DEM behaves too 'discrete' and is only useful for modelling the breakage of brittle agglomerates (Thornton *et al*., 1996; Moreno *et al*., 2003; Behera *et al*., 2005).

4.1.3 The purpose of this chapter

The purpose of this chapter is to study the performance of the Material Point Method (MPM) in modelling brittle failure during impact. The behaviours of brittle particles are studied in details in order to provide a better understanding on the simulation of particulate systems. The MPM was used to simulate dynamic material failure by Sulsky and Shreyer (2004), who adopted a decohesion law following the idea of Xu and Needleman (1994). However, only a small number of numerical results have been presented so far. In this chapter, a completely new treatment of the failure of brittle materials is proposed.

The primary motivation of employing MPM to simulate the impact induced brittle failure is its potential advantage in dealing with material fragmentation. In MPM, it is straightforward to separate two material points as opposed to mesh splitting in the traditional FEM. The accuracy of the stress analysis of MPM is the same as the traditional FEM. In addition, various different failure criteria can be used in MPM to model different materials and failure conditions. Finally, as discussed in the previous chapters, it is very easy to satisfy the contact boundary conditions. In this chapter, the Material Point Method is combined with the Weibull's failure theory (introduced in section 1.4.1) to simulate the brittle failure. Details of the numerical methodology are described in the next section. Numerical examples are presented in section 4.3. After the validation of the model, the impact failure of spherical particles is studied comprehensively and the dominating mechanisms in the impact failure are revealed. It is shown that, the MPM is very suitable for modelling of brittle failure in particulate systems.

4.2 DESCRIPTION OF THE MODEL

4.2.1 Review of the Material Point Method

The formulation of the Material Point Method (MPM) is described in details in CHAPTER 2. Here the discretized form of MPM is briefly outlined in order to provide a context for our model of brittle failure. In the MPM, the deformation of a solid body is obtained by tracing the motion of the material points, which is calculated from the nodal acceleration of the computational mesh using

$$\sum_{p=1}^{N_p} M_p N^T(\mathbf{X}_p) N(\mathbf{X}_p)\dot{\mathbf{v}} =$$
$$-\sum_{p=1}^{N_p} M_p B^T(\mathbf{X}_p)\rho_p^{-1}\boldsymbol{\sigma}(\mathbf{X}_p) + \sum_{p=1}^{N_p} M_p N(\mathbf{X}_p)\mathbf{b}(\mathbf{X}_p) + \int_{\partial\Omega} N(\mathbf{X}_p)\boldsymbol{\tau}dS$$

(4.1)

or

$$\mathbf{m}\dot{\mathbf{v}} = \mathbf{f}^{\text{int}} + \mathbf{f}^{\text{ext}}.$$

(4.2)

In Eq. (4.1) B is the spatial gradient of the shape function N. In Eq. (4.2), $\mathbf{m}$, $\mathbf{f}^{\text{int}}$, and $\mathbf{f}^{\text{ext}}$ are the consistent mass matrix, internal nodal forces, and external nodal forces on the computational mesh respectively. The bold lower case letters denote the spatial/nodal tensor variables of computational mesh while bold upper case letters denote the tensor variables of the material points. Therefore $\dot{\mathbf{v}}$ is the nodal acceleration and $\mathbf{X}_p$, M_p are coordinates, mass of the material points, respectively. In MPM, a lumped mass matrix is employed in explicit time integration instead of the consistent mass matrix on the left hand of Eq. (4.1). The stresses $\boldsymbol{\sigma}$ are traced at the material points. The material points are used as numerical integration points to calculate the volume integration, hence the first term on the right hand side of Eq. (4.1). The density of each material point ρ_p is updated at each time step in order to calculate the volume integration. In brittle failure, although the strains generally remain small, large deformation and rotation are locally possible. In order to account this, the Jaumann rate stress measure (introduced in section 1.5.1) is used in the model. The second term of the right hand side of Eq. (4.1) shows how body forces $\mathbf{b}$ such as

gravity are applied on the material points. Surface tractions $\boldsymbol{\tau}$ are applied on the computational mesh according to the third term at the right hand side of Eq. (4.1).

4.2.2 Failure criterion and its implementation in MPM

As introduced in section 1.4.1, the variability in the strength of brittle materials can be modelled using Weibull's theory (e.g. Ashby and Jones, 1986). The maximum principal stress is the dominant factor causing the brittle failure and therefore, it is used here as the stress input in Weibull's theory. The key elements of Weibull's theory is briefly outline as following: the survival probability $\bar{P}_s(V_{ref})$ of material samples of a standard volume V_{ref}, under a maximum principle stress $\sigma_{principle}^{max}$, can be calculated as

$$\bar{P}_s(V_{ref}) = \exp\left\{-\left(\frac{\sigma_{principle}^{max}}{\sigma_{ref}}\right)^{\tilde{m}}\right\} \tag{4.3}$$

where σ_{ref} is a reference stress at which the fraction of $\exp[-1] \approx 37\%$ of samples survive. $\tilde{m}$ is the Weibull's modulus reflecting how rapidly the survival probability reduces as $\sigma_{principle}^{max}$ approaches σ_{ref}. For material with a volume of $V_{material}$, its survival probability is given by

$$\bar{P}_s(V_{material}) = (\bar{P}_s(V_{ref}))^{V_{material}/V_{ref}} \; . \tag{4.4}$$

In the present model, the maximum principle stress is calculated at each material point at each time step. The survival probability of the material is then calculated using Eqs. (4.3) and (4.4). To determine whether a material point actually fails or not in the analysis knowing its survival probability, a numerical random test is performed. At the beginning of the simulation, each material point is assigned a random value ζ, between 0 and 1. At each time step, the survival probability is compared with the random value for each material point. If the survival probability of a material point is less than ζ, then this material point fails.

If failure occurs at a material point, then, the stress components of this material point will not contribute to the volume integration to $\mathbf{f}^{int}$ in Eq. (4.2). The material point is referred to as a 'ghost material point' which is kept in the system with its stress state updated. Using k as the index for the 'ghost material point', the first term of the right hand side of Eq. (4.1) can be written as

$$\left(\mathbf{f}^{int}\right)' = -\left[\sum_{p=1}^{N_p} M_p B^T(\mathbf{X}_p)\rho_p^{-1}\boldsymbol{\sigma}(\mathbf{X}_p) - \sum_k M_k B^T(\mathbf{X}_k)\rho_k^{-1}\boldsymbol{\sigma}(\mathbf{X}_k)\right] = \mathbf{f}^{int} - \mathbf{f}^{int}_{ghost}. \qquad (4.5)$$

where $\mathbf{f}^{int}_{ghost}$ is the contribution of nodal force by all the 'ghost material points' fall in the failure criteria.
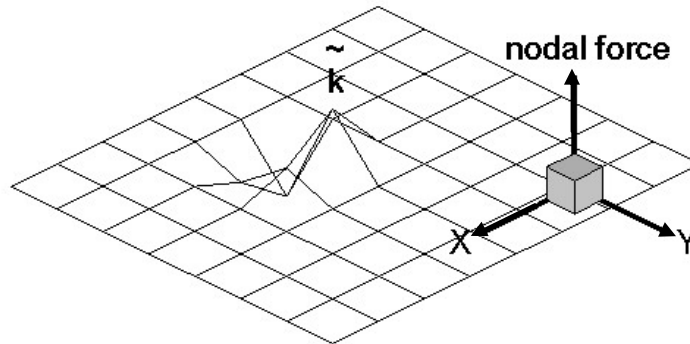
Fig. 4.2 Nodal force singularity caused by failed material point, in a 2D uniform stress plane.

The nodal force calculated from Eq. (4.5) for a uniform stress state with one 'ghost material point' is shown in Fig. 4.2. Because of the piecewise property of the shape function, the component of $\mathbf{f}^{int}_{ghost}$ reaches the maximum contribution at node $\tilde{k}$, which is the nearest node on the computational mesh to material point k. Node $\tilde{k}$ becomes a singular node where a crack is formed. In the node duplicating scheme in the

traditional FEM (Xu and Needleman, 1994, Camacho and Ortiz, 1996, Espinosa *et al.*, 1998), the node $\tilde{k}$ is duplicated and separated in order to generate a crack. The convenience when using the MPM is that the singularity is mapped back to the material points without losing any information. It is the discrete material points that are separated instead of the finite element mesh. The separation process takes place automatically through the mapping procedures. On the other hand, if a crack is closed, the stress state of the 'ghost material point' becomes compressive. The 'ghost material points' are allowed to be re-introduced back to the volume integration to the nodal force. Because all the other state variables of the 'ghost material point' are updated, the failed material points can still support compression. The stable crack healing process is therefore properly described.

4.2.3 Overall algorithm

The overall algorithm of modelling brittle failure using the Material Point Method is described as following.

1. Construct a collection of material points, and calculate their mass M_p to represent a solid body.

2. Initialize the state variables of the material points, including stresses, velocities, and strains, assign the random values of ζ .

3. Calculate nodal velocities of the computational mesh $\mathbf{v}^t$ by momentum conservation (where t denotes the present time step)

$$\mathbf{mv}^t = \sum_{p=1}^{N_p} N(\mathbf{X}_p) M_p \mathbf{V}_p^t .$$
(4.6)

4. Calculate $\mathbf{f}^{int}$ and $\mathbf{f}^{ext}$ using Eqs. (4.1) and (4.2), by excluding the contributions of the 'ghost material points'.

5. Calculate nodal acceleration of computational mesh $\dot{\mathbf{v}}^{t+\Delta t}$ using Eq. (4.2).

6. Update material point velocity

$$\mathbf{V}_p^{t+\Delta t} = \mathbf{V}_p^t + \Delta t N(\mathbf{X}_p) \dot{\mathbf{v}}^{t+\Delta t} .$$
(4.7)

7. Update nodal velocities of computational mesh, $\mathbf{v}^{t+\Delta t}$, either by solving the system of equations of

$$\mathbf{m}\mathbf{v}^{t+\Delta t} = \sum_{p=1}^{N_p} N(\mathbf{X}_p) M_p \mathbf{V}_p^{t+\Delta t} \ . \tag{4.8}$$

or by updating from previous nodal velocities

$$\mathbf{v}^{t+\Delta t} = \mathbf{v}^t + \Delta t \dot{\mathbf{v}}^{t+\Delta t} \ . \tag{4.9}$$

8. Calculate strain rate $\dot{\boldsymbol{\varepsilon}}^{t+\Delta t}$ at each material point from velocity vector $\mathbf{v}^{t+\Delta t}$. Calculate stress rate $\dot{\boldsymbol{\sigma}}^{t+\Delta t}$ using the constitutive law. Update stresses according to

$$\boldsymbol{\sigma}^{t+\Delta t} = \boldsymbol{\sigma}^t + \Delta t \dot{\boldsymbol{\sigma}}^{t+\Delta t} \ . \tag{4.10}$$

9. Calculate the maximum principle stress $\sigma_{\text{principle}}^{\max}$ from $\boldsymbol{\sigma}^{t+\Delta t}$. Calculate the survival probability using Eqs. (4.3) and (4.4).

10. Compare the survival probability with the random value of ζ to check if failure has occurred.

11. If failure has occurred at a material point, this material point is set to be a 'ghost material point'.

12. Update material point density using the determinant of the deformation gradient $J_t^{t+\Delta t}$

$$\rho_p^{t+\Delta t} = \rho_p^t (J_t^{t+\Delta t})^{-1} \ . \tag{4.11}$$

13. Update the positions of all the material points

$$\mathbf{X}_p^{t+\Delta t} = \mathbf{X}_p^t + \Delta t N(\mathbf{X}_p) \mathbf{v}^{t+\Delta t} \ . \tag{4.12}$$

14. $t \rightarrow t + \Delta t$, go back to step 3 if the computation not terminated.

The reason for using different update schemes to update nodal velocity in Eq. (4.8) or Eq. (4.9) has been explained in section 2.2.4. At each time step, the material boundary is searched to decide whether it is necessary to use Eq. (4.8), especially when new surfaces are produced by the growth of multiple cracks. It is proved that this procedure has effectively avoided the material point separation problems and minimized the numerical problems.

4.3 MODELLING THE IMPACT INDUCED BRITTLE FAILURE OF CIRCULAR PARTICLES

4.3.1 Convergence test

In the MPM model for brittle failure, the stress singularity is ignored. It is therefore necessary to show that the MPM prediction of the failure pattern 'converges' if the mesh is fine enough. As shown in Fig. 4.3, a circular disc impact on the rigid wall with a relatively high velocity of $V_0 = 16$ m/s. Plane stress conditions are assumed in the numerical model. A square computational mesh is used to cover the possible domain of the particle motion. The rigid wall is represented by imposing the acceleration and velocity constraints at the bottom line of the computational mesh. In order to focus on the effect of the mesh size, the material strength is assumed to be uniform here, i.e., $\tilde{m}$ is taken as being infinitely large in Eq. (4.3). Consequently, a material point will not fail until the maximum principle stress reaches the failure stress, which is assigned to be 50 MPa. Convergence is considered to be achieved if further refining the mesh does not change the failure pattern during impact. A range of meshes with different numbers of material points are used in the test which are listed in Table 4.1. The predicted failure patterns using the different levels of meshes are shown in the APPENDIX IV. As shown in Table 4.1, for each level of mesh status, either the material point or the computational mesh is refined. From our numerical observations, the 2D MPM model for brittle failure is not very sensitive to the material point density (this cannot be too low of course). The stress concentration is sensitive to the computational mesh. It is the computational mesh which needs to be

refined in order to capture the concentrated stress crack tips. In the comparison of the failure patterns obtained by different levels of mesh statuses in APPENDIX IV, the convergence is found to be achieved at the mesh level 4 in Table 4.1.
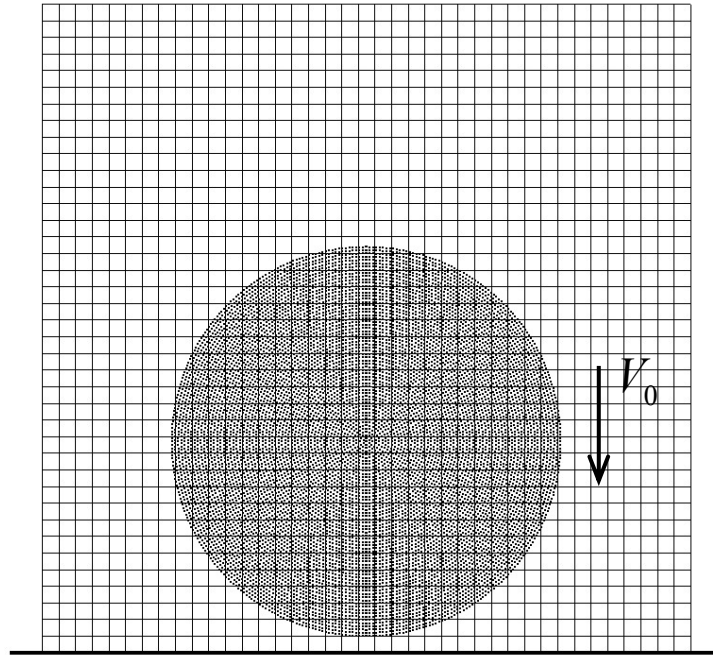
Fig. 4.3 The computational mesh of the MPM for a 2D plane stress, simulation of a circular disc impacting on a rigid wall.

4.3.2 Computer simulated impact failure using the Material Point Method

In order to simulate the experimental failure patterns described in section 4.1.1, a circular particle with a diameter of $D = 4.7$ mm is projected with different initial velocities of V_0 perpendicularly to a rigid stationary wall. Gravity is neglected therefore the starting position of the particle with respect to the wall does not have an effect on the impact. The model described in section 4.2 is used.

Table 4.1 Convergence test for the MPM model of failure patterns during particle impact.

level of mesh status	Number of material points	Number of cells in whole domain	Same pattern predicted using finer mesh ?	Same pattern predicted using much finer mesh ?
1	11102	80×80	No	No
2	43802	128×128	Yes	No
3	174002	200×200	No	No
4	693602	320×320	Yes	Yes
5	693602	400×400	Yes	N/A
6	2769602	500×500	N/A	N/A

The material parameters used in the simulations are: initial density $\rho = 2440$ kg/m^3, Young's modulus $E = 69$ GPa, and Poisson's ratio $v = 0.22$. The Weibull's modulus $\tilde{m}$ and reference stress σ_{ref} in Eq. (4.3) are taken as 20 and 50 MPa, respectively. The reference volume V_{ref} in Eq. (4.4) is taken as the entire volume of the particle. Figure 4.4 shows the kinetic energy as a function of time for four different initial velocities. The kinetic energy is normalized by the initial kinetic energy for each case. A series of snapshots of the particle are also shown in Fig. 4.4 for the case of impact velocity $V_0 = 10$ m/s. Figure 4.5 shows the final failure patterns of the particle for four different impact velocities. At impact velocity of $V_0 = 5$ m/s, the brittle particle exhibits a typical elastic response. Starting form the point of impact, the kinetic energy reduces gradually to zero, which reflects the maximum compression status during the impact. The total kinetic energy then increases and fully recovers after rebound (excluding the numerical and elastic wave dissipation). No crack is found as no material point meets the failure criterion during the impact.

At impact velocity of $V_0 = 6$ m/s, the falling of kinetic energy is slightly faster than that of $V_0 = 5$ m/s and the total impact time is shortened. Discernable energy

dissipation (about 10% of initial kinetic energy) is observed after rebound, reflecting the total amount of converting kinetic energy into crack formation energy. In the final state, the particle shows some damage adjacent to both sides of the contact area. Recalling that the simulations assume plane stress conditions, it is reasonable to associate Pattern i in Fig. 4.5 with the experimental observation, Pattern I, in Fig. 4.1(a), Furthermore, inside the ring, two secondary vertical cracks at both sides of the central axis can be clearly observed. These details are in good consistency with experimental observations shown in Fig. 4.1(a).
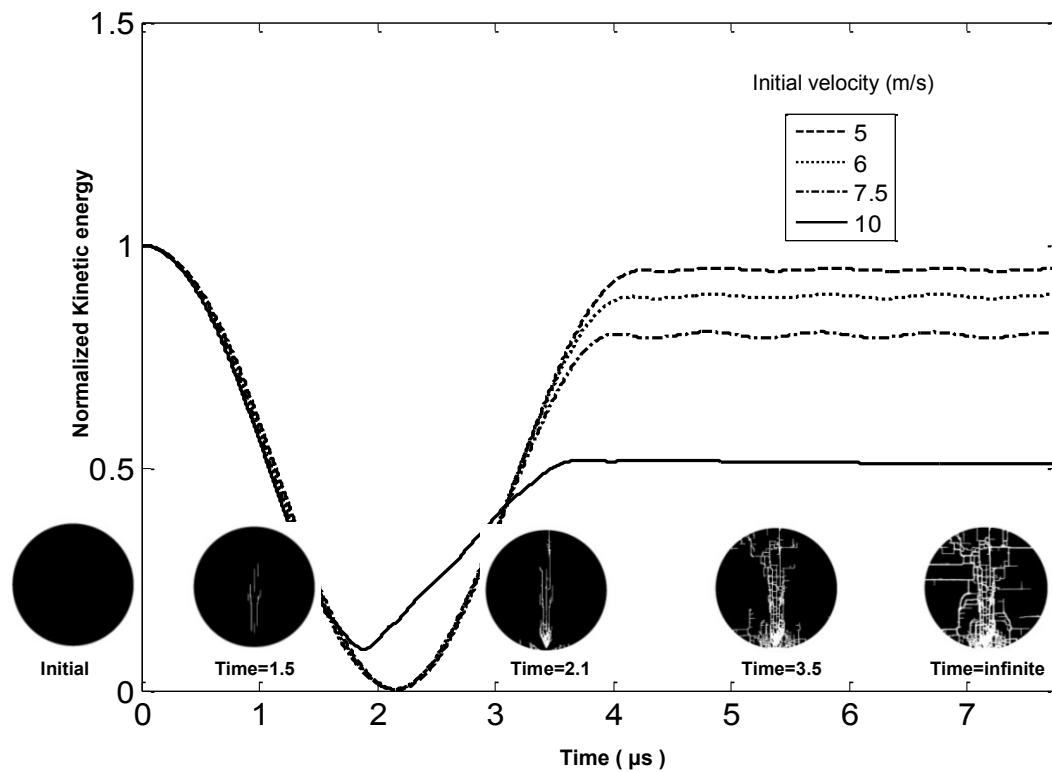
Fig. 4.4 Normalized kinetic energy as a function of time for different impact velocities. The horizontal row of particles shows snapshots during impact for the initial impact velocity of $V_0 = 10$ m/s.

If the initial impact velocity of the brittle particle is increased to $V_0 = 7.5$ m/s, there is a remarkable reduction in the kinetic energy after rebound. The minimum value of the kinetic energy is close but not equal to zero. The non-zero part suggests that some

material points have failed and some of the kinetic energy was used for crack formation. The reason why the kinetic energy at the bottom is slightly above zero is that the failed material points do not move harmonically with the main particle anymore. The final failure pattern is that the particle is divided into two halves by a main crack along the middle axis, with some small branches also present (Pattern ii in Fig. 4.5). This can be directly related to the meridian crack that splits the particle into two or several parts, i.e. Fig. 3.1(b), Pattern II observed experimentally. About 20% of the initial kinetic energy is converted into crack energy leading to this brittle failure pattern. It is noticeable that the crack is not exactly lying on the central axis. This is possibly because the strengths between the two sides of the central axis are not the same. The long main crack grows from a small crack which is in a weaker side of the central axis.
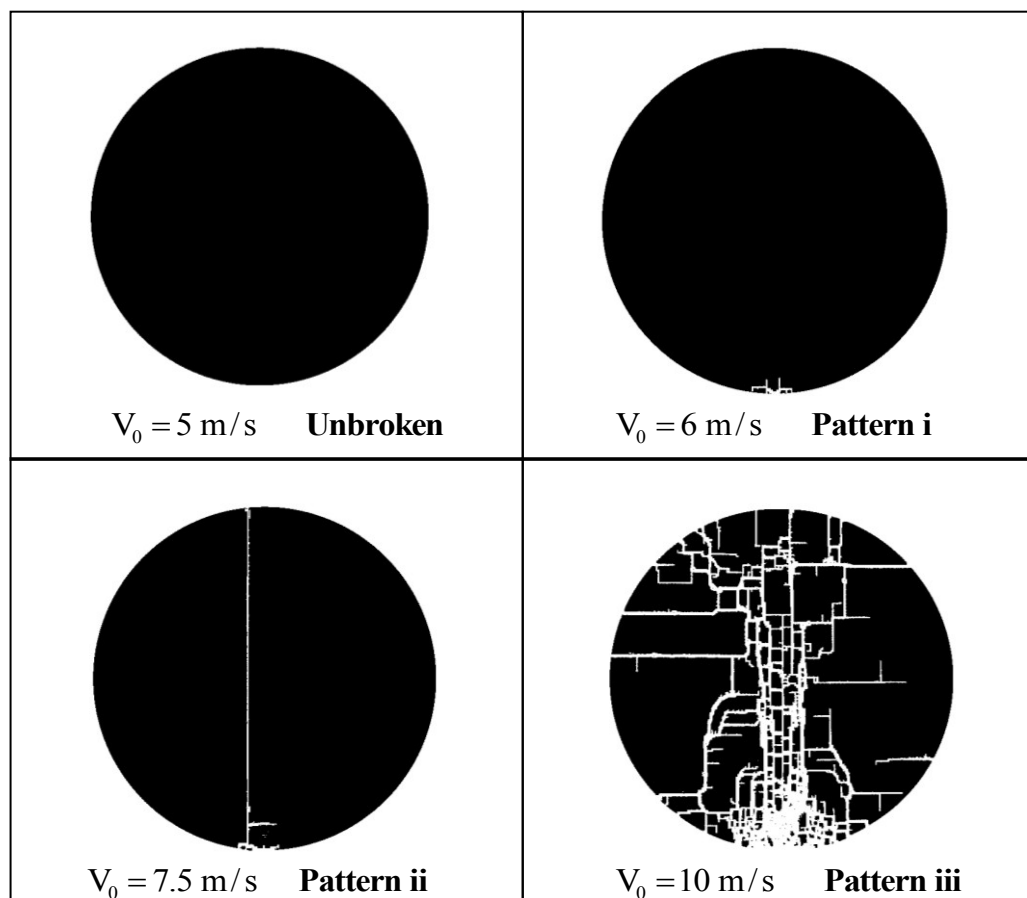
Fig. 4.5 Computer simulated final failure patterns for different impact velocities.

The largest initial impact speed shown in Fig. 4.4 is $V_0 = 10$ m/s. At this velocity, the normalized kinetic energy curve (solid line in Fig. 4.4) behaves similarly to the study of shock induced cracks, by Wagner and Holian (1992) using molecular dynamics simulations. At first, the kinetic energy decreases fast. The bottom of the curve drifts upwards from zero by 10%, reflecting that a large part of the material failed during the inbound period of impact. During the rebound period, the curve reaches a peak, marking the finishing point of the impact. After rebound, the total kinetic energy, including the kinetic energy of both failed and unfailed materials, slowly decreases to the final stable status. This suggests that the cracks continue to grow gradually after the full rebound to reach the final failure pattern - Pattern iii in Fig. 4.5.

The evolution of the failure Pattern for $V_0 = 10$ m/s is also shown in the horizontal row of particles in Fig. 4.4. Cracking is firstly initiated beneath the contact area during the inbound stage of impact. When compression reaches its peak, this crack grows vertically upwards and downwards. Ring cracks are also generated at the bottom of the particle while they coalesce with the vertical crack to form a cone crack pattern. Cracks are formed and grow very fast during the rebound period of the impact. It is important to note that most cracks are generated at this period. As suggested by Potapov and Campbell (1997), cracks perpendicular to the vertical crack are formed during the rebound period because of bulk bending in the material. Furthermore, the secondary cracks could originate not only from the main crack tips but also some distance away. Similar findings were reported by Xu and Needleman (1994). After full rebound, the inter-perpendicular cracks further grow and divide the material into small pieces projecting away from the area of impact. The simulated final failure pattern relates well to the experimental observations summarized in Fig. 4.1(c).

4.3.3 Stress field in the particle

In order to obtain a more fundamental understanding of the failure patterns shown in section 4.3.2, it is instructive to examine the distribution of the maximum principle stress, which is used in the failure criterion for brittle failure. The stress field at an

early stage of the impact when there exists only one main crack is plotted in Fig. 4.6(a). For comparison purpose, the stress field of an unbroken particle (obtained by setting a ultimate high value for the reference stress σ_{ref} in Eq. (4.3) while keeping all other parameters the same) is plotted in Fig. 4.6(b). The maximum principle stress contours of the unbroken particle are similar to the force contours found by Potapov and Campbell (1997) using the Discrete Element Method. The maximum principle stress of an unbroken particle has an azimuthal distribution. The maximum value of the maximum principle stress occurs beneath the contact area. This position of maximum principle stress coincides with the location of crack initiation. The stress decreases upward and downward. Originating in the small zone between the maximum location and the contact area, isostress contours surround azimuthally the maximum stress zone and spread into the whole particle. The stress field is extensively altered by the opening of cracks. In Fig. 4.6(a), in the presence of a crack along the central axis, the stresses away from both sides of the crack are severely reduced. Stresses near crack tips are intensified and small areas of stress concentration near crack tips are formed. These stress concentrations drive the growth of the main crack and can lead the current crack to meridian failure of Pattern II in Fig. 4.1(b) and Pattern ii in Fig. 4.5. Above the main crack, stress distribution is relatively unchanged. The main difference is that all stress contours originate at the upper crack tip rather than just above the contact area.

The stress field of a particle when rebounding but still in contact with the wall is plotted in Fig. 4.6(c). At this time instance, most stresses in the material body have been relaxed, leaving two stress concentration zones on the both sides of the contact area, which resemble the Hertzian rings normally occurring at lower impact velocities. The stress concentration just before the full rebound is the main mechanism for Pattern I in Fig. 4.1(a) and Pattern i in Fig. 4.5. Naturally Hertzian ring cracks can occur at other time instances during the high velocity impact history, such as shown in the series of snapshots in Fig. 4.4. However, in this case the Hertzian rings may be surpassed by other cracks developing during the process. Therefore, the distinct ring cracks are unlikely to be present in the final configuration. From the stress analysis

point of view, however, the Pattern III in Fig. 4.1(a) and Pattern iii in Fig. 4.5 result from the iteration of crack induced stress concentration, which is similar to the stress field in Fig. 4.6(a).

label number	max principle stress(MPa)
1	5
2	10
3	20
4	30
5	40

(c)   **legend**
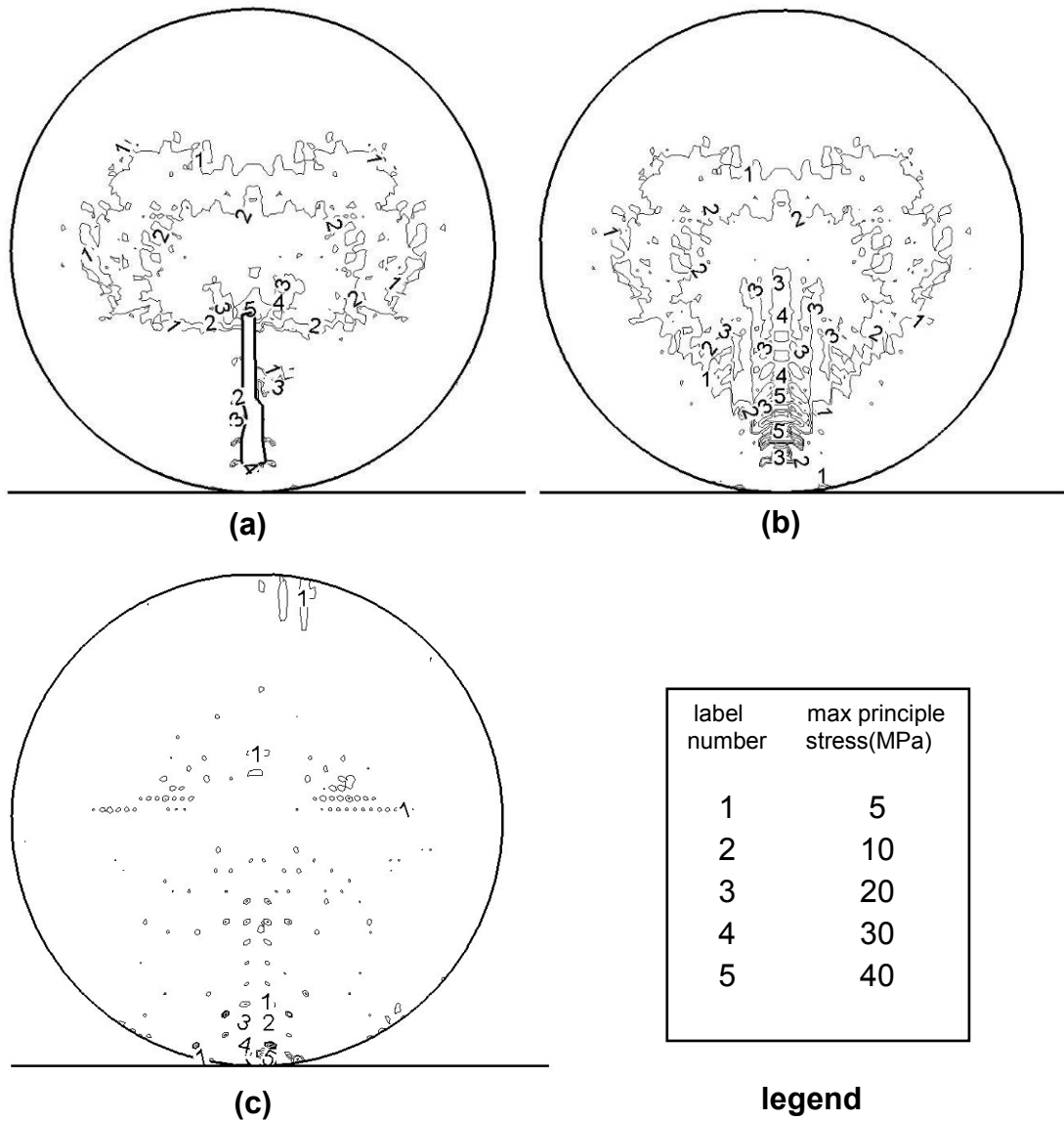
Fig. 4.6 Contour lines of the maximum principle stress field at three different characteristic impact stages. The numbers refer to the stress values. (a) The stress field of a particle with one open crack beneath the contact area, (b) the stress field of a particle same with (a) except it is unbroken, and (c) the stress field of an unbroken particle at the time instance that the particle is just releasing from the wall.

4.3.4 Threshold velocity

According to Cheong *et al.* (2003), and Andrews and Kim (1998), the thresholds of impact velocities exist for failure Patterns I and II to occur respectively. The threshold velocity was found to follow a power law relation on the particle size with a negative exponent. Whilst it is intuitive that the severity of the damage increases with the impact velocity, modelling this phenomenon provides a quantitative understanding of the velocity effect. In order to focus on the effect of the impact velocity, the parameter ζ is set randomly (as before) but fixed for all particles. The reference volume V_{ref} in Eq. (4.4) is taken as the volume of the particle of 4.7 mm in diameter. The threshold velocities for Pattern I and Pattern II are plotted against the particle diameter (in logarithm scale) in Fig. 4.7.

As shown in Fig. 4.7, the threshold velocity of brittle failure Pattern I, i.e. Hertzian ring, decreases exponentially with the increasing diameter of the particle, D. The relationship can be written as

$$V_{\text{Hertz}}^{\text{th}} = \overline{A}_1 D^{\overline{\alpha}} . \tag{4.13}$$

The threshold velocity of brittle failure Pattern ii, meridian crack, also decreases exponentially with the increasing diameter of the particle, i.e.

$$V_{\text{meri}}^{\text{th}} = \overline{A}_2 D^{\overline{\beta}} . \tag{4.14}$$

In Eq. (4.13) and Eq. (4.14), $\overline{A}_1$, $\overline{A}_2$ are numerical coefficients, and $\overline{\alpha}$, $\overline{\beta}$ are exponents determined from Fig. 4.7 as $\overline{\alpha} = -0.074$, $\overline{\beta} = -0.094$, respectively. From the elastic theory for 2D impact (Potapov and Campbell, 2001), the maximum compressive force occurs at the time instance of the largest compression, given by

$$F_{\text{max}} = const\ ED(V_0 / \sqrt{E/\rho})^{1.07} . \tag{4.15}$$
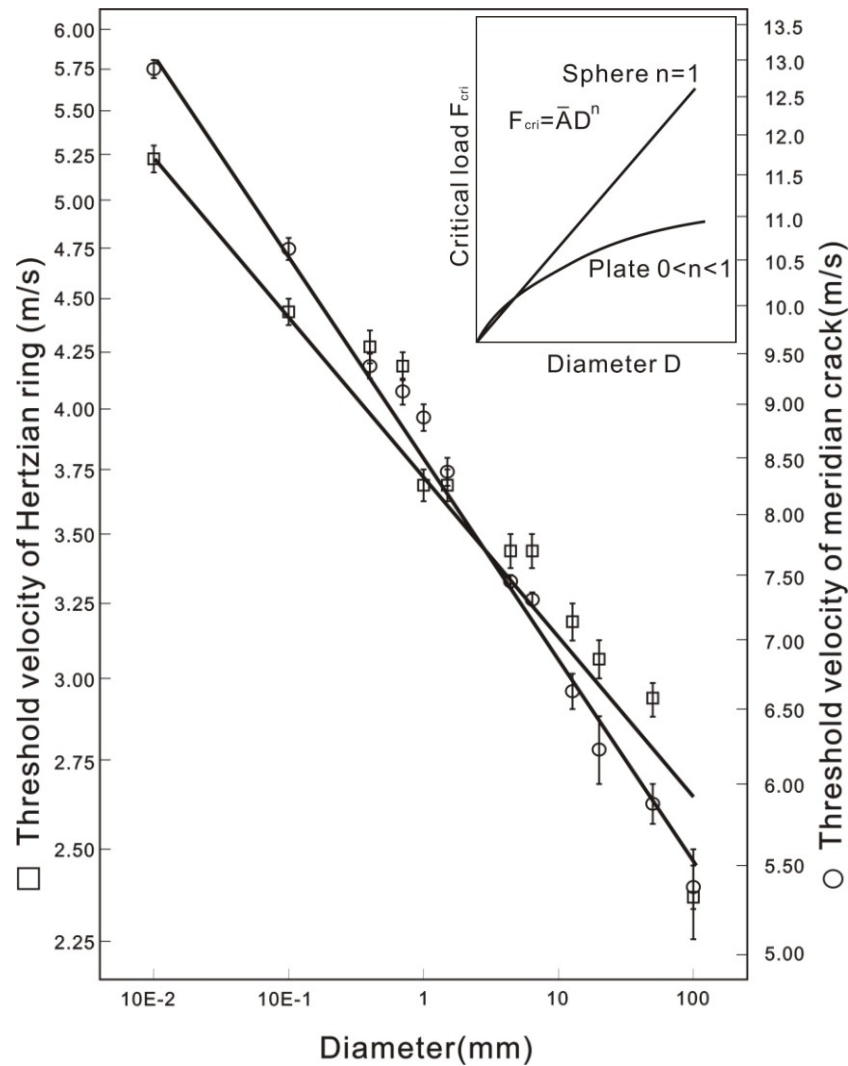
Fig. 4.7 Threshold velocities against particle diameter. Inset: modified Auerbach's Law of 3D, and 2D plane stress.

As suggested by Cheong *et al*. (2003), the impact threshold velocity for Hertzian ring can be analysed using the well known Auerbach's Law, which can be used to infer the value of the static loading necessary to produce a Hertzian ring crack. As shown in the inset of Fig. 4.8, in the present model the plane stress particle represents a plate. In this case it is easier to induce damage as the particle size increases comparing with the 3D situation, so we have

$$F_{cri} = \bar{A} D^n. \tag{4.16}$$

where F_{cri} is the force required to create a damage. The exponent n in Eq. (4.16) as well as in the inset of Fig. 4.7 can be found by experiment and is expected to be between 0 and 1. To examine the value of n, we equate Eqs. (4.13) and (4.15) with the Auerbach's Law $F_{max} = F_{cri}$. The threshold velocity for the Hertzian ring crack is

$$V_{Hertz}^{th} \propto D^{(n-1)/1.07} = D^{\bar{\alpha}}.$$ (4.17)

Equation (4.17) implies that, if $0 < n < 1$, $\bar{\alpha}$ is a number between 0 to -1 with a small absolute value, which is consistent to our numerical result $\bar{\alpha} = -0.074$. For the meridian cracks, Potapov and Campbell (1997) suggested that the central axis crack length parameter ε^* is given by

$$\varepsilon^* = \frac{\rho D V_0^2}{W_{fr}} (V_0 / \sqrt{E/\rho})^{0.14} f^*(v)$$ (4.18)

where W_{fr} is the energy required to produce unit length of crack, and $f^*(v)$ is a function depending only on Poisson's ratio v. In order to generate a crack along the central axis, the central axis crack length must be proportional to the particle size such that

$$D \propto \varepsilon^*$$ (4.19)

Solving Eq. (4.18) and Eq. (4.19) for the particle diameter D indicates that the velocity for generating a central axis crack, referred to as V_{meri}, which is independent of the particle size D. However, the central axis crack must appear after the cone crack which is generated from the Hertzian ring crack. Considering the crack formation energy, the threshold velocity of initializing the meridian crack pattern is consisted of two parts, i.e.

$$V_{meri}^{th\ 2} = V_{Hertz}^{th\ 2} + V_{meri}^{2}$$ (4.20)

The first term on the right hand side of Eq. (4.20) denotes the formation energy for Hertzian crack while the second term denotes the formation energy for central axis crack. Since the velocities are always positive, Eq. (4.20) leads

$$(V_{\text{Hertz}}^{\text{th}} + V_{\text{meri}})^2 \geq V_{\text{meri}}^{\text{th}}{}^2 = V_{\text{Hertz}}^{\text{th}}{}^2 + V_{\text{meri}}{}^2 \geq V_{\text{Hertz}}^{\text{th}}{}^2 \tag{4.21}$$

Using Eq. (4.13), we obtain

$$D^{\bar{\alpha}} + C_1 \propto (V_{\text{Hertz}}^{\text{th}} + V_{\text{meri}}) \geq V_{\text{meri}}^{\text{th}} \geq V_{\text{Hertz}}^{\text{th}} \propto D^{\bar{\alpha}} \tag{4.22}$$

where C_1 is a positive constant because V_{meri} is independent of D. It is noticed that the particle sizes D shown in Fig. 4.7 are relatively small (see Fig. 2 by Cheong *et al.* 2003, and Fig. 3 by Potapov and Campbell, 2001 for details). Approximating the left hand side of Eq. (4.22) using an exponential function, Eq. (4.14) and Eq. (4.21) lead to

$$\bar{\alpha} + C_2 \leq \bar{\beta} \leq \bar{\alpha} \tag{4.23}$$

where C_2 is a negative number depending on C_1. Since the crack energy for cone crack and the crack energy for central axis crack are always comparable, $V_{\text{Hertz}}^{\text{th}}$ and V_{meri} are comparable. As a consequence, $D^{\bar{\alpha}}$ and C_1 are comparable, and $\bar{\alpha}$ and C_2 are also comparable. Therefore, Eq. (4.23) is also consistent with our numerical observations in Fig. 4.7 that $\bar{\beta} = -0.094$ and $\bar{\beta}/\bar{\alpha} = 1.27$.

4.3.5 Discussions

It can be observed that the brittle failure patterns in our numerical simulations shown in Fig. 4.5 and the experimental observations shown in Fig. 4.1 are consistent with each other despite that the experiment used 3D particles while the numerical models assumed plane stress. However, during the modelling of Pattern III, it appears that the meridian crack is almost always present. The failure pattern is sensitive to the randomly assigned values of ζ which reflect the material heterogeneity. This is consistent with the findings by Xu and Needleman (1994). The process of the crack formation can be understood as a competition between the stress field and the strength heterogeneity of the material. Due to this competition, amongst our simulations with different distributions of ζ, there are some cases that show only oblique cracks

without a meridian crack. Salman and Gorham (2000) showed that all particles in a certain velocity and size range fail by forming oblique cracks in their experiments. This failure pattern (left hand side in Fig. 4.1(c)) appeared to have a weak dependence on the material heterogeneities. More study is needed to fully understand this phenomenon.

The azimuthal stress field in Fig. 4.6(b) is inevitably altered by crack formation. Unlike the crack patterns predicted by Potapov and Campbell (1997) using the Discrete Element Method, the fan like cracks along the paths of the maximum principle stress are not observed in our simulations. Meanwhile, the energy trade off between cracks generated during inbound process and cracks generated during rebound process still holds but not as obvious as that in DEM predictions (Potapov and Campbell, 1997). The expanded crack distributions during inbound at a larger impact speed could be attributed to the larger contact area.

The threshold velocity study shown in Fig. 4.7 indicates a possible way of obtaining a particular crack pattern during an impact. The negative exponential dependence means that as the particle size gets smaller, the particle becomes more sensitive to impact velocity. For example, in order to eliminate particle damage, there are basically two methods: to increase particle size or to reduce impact velocity. Which method to choose depends on the level of the impact velocity and the particle size. For example, to avoid impact damage, the method of changing particle size is much more effective for small particles than for large particles.

4.4 CONCLUDING REMARKS

Understanding the impact failure of brittle particles is an important issue for many industrial particles. The Finite Element Method is fundamentally ill-equipped to model the brittle failure. In this chapter Weibull's theory is incorporated into the Material Point Method to model the multi-cracking of brittle particle during impact. Three particle impact failure patterns observed experimentally are predicted by the

model: Hertzian ring cracks, meridian cracks, and fragmentation patterns. The observed power law relation between the threshold impact velocity and particle size is also confirmed by the numerical study. These comparisons, despite being quantitative, give confidence to the numerical model. Detailed stress analysis is carried out in order to interpret the experimental observations. It is however difficult to convey the numerical and programming simplicity of the MPM in dealing with multiple cracks and material fragmentation. Almost no extra programming effort is needed to deal with the complicated failure process when implementing the Material Point Method. Because the method does not involve any imperial judgement in mesh splitting, the computer simulations are rarely terminated prematurely due to numerical issues. The Material Point Method is ideal to model to transition from continuum to discreteness.

Modelling multiple cracking and material fragmentation is perhaps one of the most challenging tasks in computer simulation. There are still some unresolved issues in this topic. The MPM model proposed in this chapter provides a confident and simple solution. For the simulation of particulate systems in Discrete Element Method (DEM), the MPM model can be used for both the brittle failure checking and the final fragment prediction. Furthermore, the contact law between fragments can be also calculated using the MPM, as introduced in the previous chapter. The MPM model can be therefore performed routinely to obtain the detailed inputs for the DEM simulations.

CHAPTER 5 ADHESIVE CONTACT BETWEEN FINE PARTICLES

This chapter proposes a new model based on the MPM, which is used to study the contact laws between fine particles taking into account the effect of surface energy.

5.1 THEORETICAL BACKGROUND

As described in section 1.4.2, the influence of adhesion can be important in particulate systems. The effect of adhesion becomes more significant during the contact between finer particles. In the past decades, the research focused on measuring local mechanical properties as well as characterizing the deformation of small particles leads to the need of coupling material properties with surface interactions. Moreover, the expanding demand for simulating particulate systems generated significant interest in the adhesive contact law between two fine particles, since it provides a fundamental understanding of how fine particles interact with each other.

The origin of adhesion lies in inter-atomic forces, which form inter-atomic bonds when two surfaces are put together. The work done by the inter-atomic forces when eliminating the two surfaces macroscopically is termed as surface energy. During the contact between two deformable particles, the released surface energy (or free energy) is readily converted to deformation strain energy which further deforms the two contacting bodies. As a consequence, the deformation changes the status of the surfaces and the amount of surface energy, causing further deformation. This nonlinearity due to the interplay between the surface energy and the deformation strain energy makes the problem of adhesive contact much more complicated than contact problems neglecting adhesion (studied in CHAPTER 3).

The well known JKR theory (Johnson *et al.*, 1971) is very widely used as an adhesive contact law today in the simulations of particulate systems containing fine particles. However, as pointed out by Johnson *et al.* (1971), the JKR theory is only valid if the particles are pure elastic and so soft that the surface roughness can be easily flattened to smooth the surface. In most practical particulate systems, contacts are controlled by the interaction between asperities of the rough surfaces, where plastic deformation may dominate and the JKR theory is no longer valid any more.

The purpose of this chapter is to obtain more realistic adhesive contact laws numerically. The existing literature is reviewed in the next section, and then a new multi-scale model based on the Material Point Method (MPM) and Molecular Dynamics (MD) is developed. A range of important factors of adhesive contact are studied under realistic situations in order to provide a better understanding of the interactions between fine particles. The ultimate goal of this chapter is to provide realistic adhesive contact laws which can be used as inputs in discrete element simulations of particulate systems. Like other contact laws studied in previous chapters, this chapter focuses on the frictionless normal contact between a spherical particle and a planar rigid wall, which is equivalent to the none-slip contact between two identical spherical particles.

Before we start, the following terminology used in the present chapter is introduced. Surface energy is defined as the total energy released by eliminating two free surfaces. Specific surface energy is defined as the surface energy per unit area of the surface. Adhesion force is defined as the normal force due to surface energy acting on a particle surface when two surfaces are interacting. Adhesive surface traction is defined as the adhesion force per unit area, which depends on the gap between surfaces. Pressure on the surface is the material response due to deformation and can be understood as 'stress on the surface'.

5.1.1 Two classical approaches

As mentioned above, the complexity of the adhesive contact is represented by the nonlinear interplay between the surface energy and the deformation strain energy (and mechanical potential for static loading or kinetic energy for dynamic problems). Two classical approaches are generally used in the past works. The first approach is named as the analytical approach, which assumes that contact takes place at an equilibrium distance between two surfaces. The distance between two contacting surfaces is always a constant ε, which is normally comparable to the equilibrium atomic spacing ε_0. The two surfaces attract each other when they are not in contact, i.e., when the gap between the two surfaces is larger than ε. Therefore, one can use a distance dependant adhesive surface traction outside the contact area (Derjaguin *et al*., 1975; Maugis, 1992; Greenwood and Johnson, 1998; Schwarz, 2003). The JKR theory (Johnson *et al*., 1971) can be also considered as a special case of this approach since it implicitly assumes an infinite adhesive surface traction at the edge of the contact area. The second approach is named as the numerical approach, which uses more 'realistic' adhesive surface traction between surfaces. The adhesive surface traction with an equilibrium distance ε includes an attractive part and a repulsive part. Two surfaces are attracting each other when the gap is larger than ε, while repelling each other when the gap is smaller than ε. This distance dependent adhesive surface traction is regarded as the pressure on the surface through a series of small time steps. By solving the equations of elasticity, the interplay between the deformation and the surface energy can be studied using an iterative scheme (Parker and Attard, 1992; Greenwood, 1997; Feng, 2000).

In the terminology of contact mechanics, most analytical elastic adhesive contact theories are based on the well known Hertz theory (e. g. Johnson, 1985), and can be distinguished by their unique assumptions (either explicit or implicit) about the pressure distribution on the surface. The Hertz theory outlined in section 1.3 is a basis for the subsequent review of the theories of adhesive contact. The basic assumptions of Hertz theory include: (i) the particle is spherical and purely elastic; (ii) the curvature of the particle near the contact area is large compared to the size of contact

area; and (iii) the contact is normal, frictionless (or non-slip between two identical particles). Figure 5.1(a) shows a typical Hertz contact of an elastic, spherical particle with a radius R, in normal contact against a rigid wall, forming a circular contact area with radius a_0. The displacement of the particle δ is the change of length of the diameter on the central axis of the particle, which is given by Eq. (1.11). As shown in Fig. 5.1(a), the Hertz elliptical contact pressure distribution $p_{\mathrm{Hertz}}(r)$ at an arbitrary radial distance r on the surface is non-zero only inside the contact area, which is explicitly given by Eq. (1.13). The Hertz contact law in the form of $F - \delta$ relation is given by Eq. (1.19).

5.1.2 The Analytical approach

The most widely used adhesive contact law when simulating particulate systems is the JRK theory (Johnson *et al.*, 1971). Therefore it is worthy to introduce the JRK theory first. Johnson *et al.* (1971) noticed that the adhesion force between an elastic particle and a rigid wall has a tendency to increase the size of the contact area. As shown in Fig. 5.1(b) the radius is increased from a_0 to a_1 in the presence of adhesion. Therefore there must be an adhesive tensile pressure applying to the particle surface in addition to the Hertz compressive pressure. On the other hand, if assumption (ii) is valid, the profile of the particle near the contacting surface should remain unchanged. Johnson *et al.* (1971) therefore assumed that the additional adhesive pressure produces a uniform normal displacement within the contact area and follows the form (as shown in Fig. 5.1(b))

$$p_1(r) = P_1 \left[1 - (r/a_1)^2 \right]^{-1/2}.$$ (5.1)

Consequently the pressure on the surface only exists inside the contact area and is the sum of the compressive Hertz pressure (Eq. (1.13)) and the tensile pressure that produces a uniform displacement (Eq. (5.1)), i.e. we have

$$p_{\mathrm{JKR}}(r) = p_1(r) + p_{\mathrm{Hertz}}(r) = P_0^e \left[1 - (r/a_1)^2 \right]^{1/2} + P_1 \left[1 - (r/a_1)^2 \right]^{-1/2}.$$ (5.2)
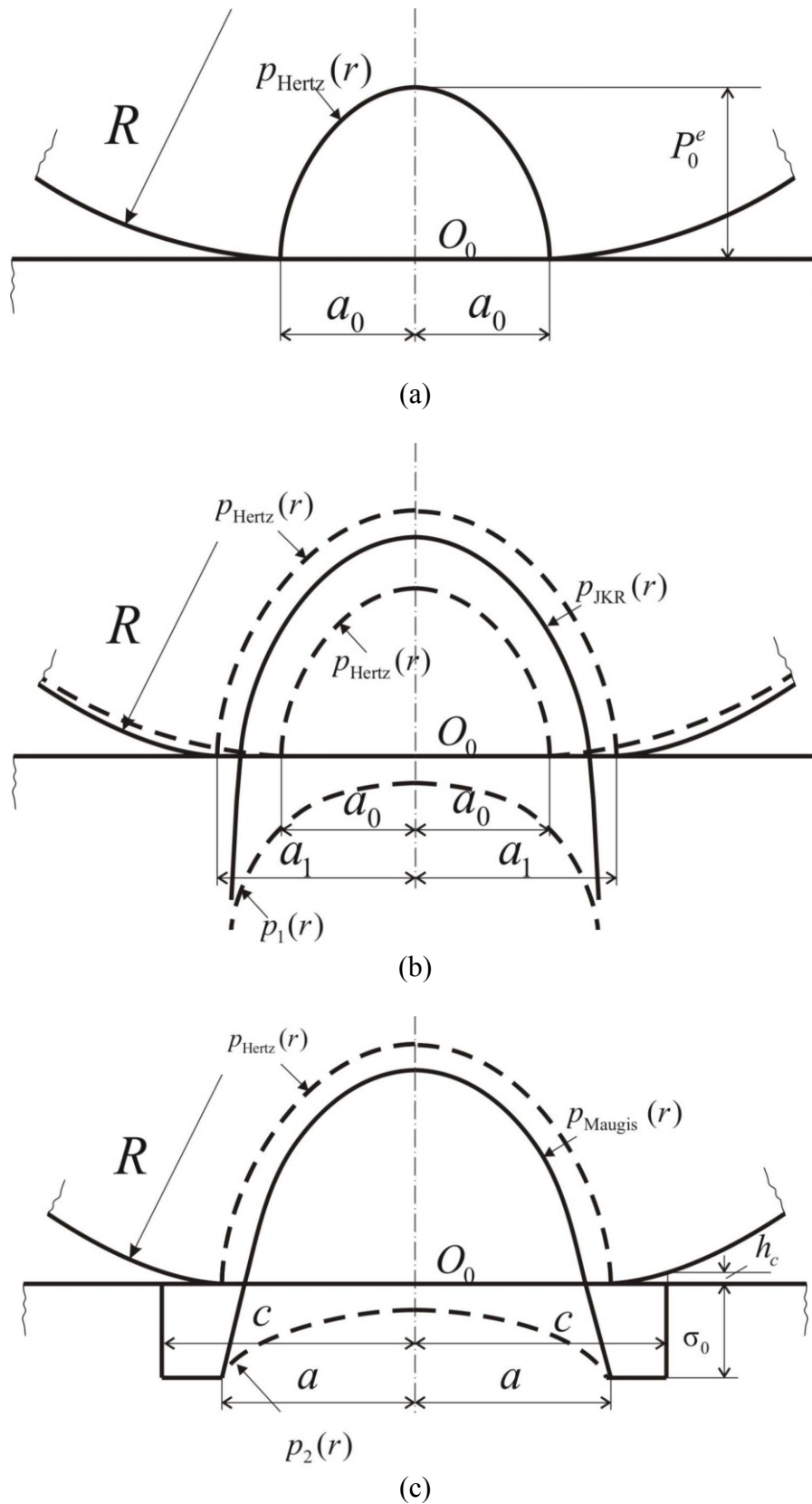
Fig. 5.1 Particle profile and distribution of contact pressure. (a) Hertz theory, (b) JKR theory, (c) Maugis theory.

In Eq. (5.2), $P_0^e = 2E^* a_1 / \pi R$, which takes the same form as the Hertz theory but applies on the increased contact area a_1. P_1 is the value of the tensile pressure at the centre of the contact area which can be obtained by balancing the elastic strain energy with the total surface energy as

$$P_1 = -(2\gamma E^* / \pi a_1)^{1/2}.$$

(5.3)

In Eq. (5.3), γ is the specific surface energy of the surface of the particle. The rigid wall is considered to have no surface energy in order to represent the contact between two identical particles. Knowledge of the pressure distribution $p_{JKR}(r)$ is crucial in calculating the contact law. For the normal contact, F_{JKR} can be obtained as

$$F_{JKR} = \int_0^{+\infty} 2\pi r p_{JKR}(r) dr,$$

(5.4)

which leads to

$$\left(F_{JKR} - \frac{4E^* a_1^3}{3R} \right)^2 = 8\pi\gamma E^* a_1^3.$$

(5.5)

The total displacement, δ_{JKR}, is the sum of the displacement produced by Hertz contact pressure and the additional adhesive tensile pressure $p_1(r)$, given by

$$\delta_{JKR} = (\pi a_1 / 2E^*)(P_0^e + 2P_1).$$

(5.6)

The JKR contact law can be obtained by eliminating a_1 from Eq. (5.5) and Eq. (5.6), as shown in Fig. 5.2. Furthermore, by minimizing the F_{JKR} in Eq. (5.10) the maximum tensile force F_{JKR}^c is found as

$$F_{JKR}^c = -1.5\pi\gamma R,$$

(5.7)

which is the tensile force required to pull a spherical particle off a rigid wall (the pull-off force). The pull-off force only depends on the size and specific surface energy of the particle and does not depend on external loading or any other material parameters.

The JKR theory works well in a range of elastic contact problems. However, as shown in Fig. 5.1(b), the JKR theory suggested that there is no adhesive tensile pressure outside the contact area, but an infinite adhesive tensile pressure at the edge of the contact area. This is somehow confusing. According to the concept of surface energy, the surfaces attract each other by an adhesive surface traction when the two surfaces are not in contact, i.e., an adhesive surface traction should exist outside the contact area. Based on this argument, Derjaguin *et al.* (1975) proposed their DMT theory. They assumed that the adhesion between two simple curved surfaces such as spherical surfaces can be represented by the adhesion between two planar surfaces such that

$$F_{\text{adhesion}}^{\text{Derjaguin}} = \int_0^R 2\pi r \sigma_a(h) dr = 2\pi R \int_0^{+\infty} \sigma_a(h) dh = 2\pi\gamma R, \tag{5.8}$$

where $\sigma_a(h)$ is the adhesive surface traction depending on the distance due to the attraction between the two surfaces, and h is the size of the gap between the two surfaces. This assumption is referred to as the Derjaguin's approximation, which employs a simplification at small deformation $rdr = Rdh$ to derive Eq. (5.8). Derjaguin *et al.* (1975) also assumed that the adhesive surface traction only takes place outside the contact area. The adhesive surface traction only changes the total contact force but produces no further deformation. Therefore, the normal contact force F_{DMT} is given by

$$F_{\text{DMT}} = F_{\text{Hertz}} - F_{\text{adhesion}}^{\text{Derjaguin}} = F_{\text{Hertz}} - 2\pi\gamma R. \tag{5.9}$$

The radius of the contact area in DMT theory follows the Hertz theory in Eq. (1.17) and the displacement δ_{DMT} follows exactly the Hertz solution (Eq. (1.19)) such that

$$\delta_{\text{DMT}} = \left[3F_{\text{Hertz}} / (4R^{1/2}E^*) \right]^{2/3}. \tag{5.10}$$

The DMT theory employs a direct force summation in Eq. (5.9) rather than the pressure integration as in the JKR theory. The DMT contact law is therefore rather different from the JKR contact law, as shown in Fig. 5.2. Meanwhile, from Eq. (5.9),

by simply setting the Hertz force to zero, the pull-off force from DMT theory is obtained as

$$F_{DMT}^c = -2\pi\gamma R,$$
(5.11)

which differs from the pull-off force of JKR theory given by Eq. (5.7).

Tabor (1977) pointed out that the JKR theory and the DMT theory are two opposite extremes of the elastic adhesive contact, which can be controlled by the Tabor's parameter

$$\bar{\mu} = \left(\frac{R\gamma^2}{E^{*2}\varepsilon^3} \right)^{1/3},$$
(5.12)

Equation (5.12) is obtained from the ratio between the elastic displacement produced by the maximum tensile (pull-off) force and the distance between the two contacting surfaces ε. The JKR theory is valid for large values of $\bar{\mu}$ which can be achieved in large and compliant spheres with relatively large specific surface energy γ. The DMT theory is valid on the opposite extreme. The transition behaviour between the JKR theory and DMT theory was modelled by Maugis (1992). As shown in Fig. 5.1(c), an additional adhesive tensile pressure distribution $p_2(r)$ is added to the Hertz contact pressure. Maugis employed a tensile pressure, $p_2(r)$, of the following form

$$p_2(r) = \begin{cases} -(\sigma_0/\pi)\cos^{-1}\left\{ \dfrac{2a^2 - c^2 - r^2}{c^2 - r^2} \right\}, & r \leq a \\ -\sigma_0, & a \leq r \leq c \end{cases}$$
(5.13)

where a is the radius of the contact area. The tensile pressure outside the contact area is assumed as a constant adhesive surface traction σ_0 acting over the range of $a \leq r \leq c$. Typically, the gap between the two surfaces at $r = c$ is equal to the critical length h_c beyond which the adhesive tensile pressure $p_2(r)$ vanishes, and we have the following relation:

$$h_c \sigma_0 = \gamma. \tag{5.14}$$

The pressure distribution on the surface is therefore the Hertz pressure plus the additional adhesive tensile pressure $p_2(r)$

$$p_{\text{Maugis}}(r) = p_{\text{Hertz}}(r) + p_2(r). \tag{5.15}$$

The total contact force is calculated by integrating Eq. (5.15) over the entire particle surface

$$F_{\text{Maugis}} = \int_0^{+\infty} 2\pi r p_{\text{Maugis}}(r) dr = (2/3) P_0^e \pi a^2 - 2\sigma_0 \left[c^2 \cos^{-1}(a/c) + a\sqrt{c^2 - a^2} \right]. \tag{5.16}$$

The displacement δ_{Maugis} is the Hertz displacement plus an additional displacement produced by $p_2(r)$, i.e. we have

$$\delta_{\text{Maugis}} = (\pi a / 2E^*) P_0^e - (2\sigma_0 / E^*)\sqrt{(c^2 - a^2)}. \tag{5.17}$$

The main contribution of the Maugis theory is that there introduced a non-dimensional parameter $\bar{\lambda}$ to characterise the transition between the JKR extreme and the DMT extreme, which is given by

$$\bar{\lambda} = \sigma_0 \left(\frac{9R}{2\pi\gamma E^{*2}} \right)^{1/3}. \tag{5.18}$$

The gap between the two surfaces at any position outside the contact area can be obtained from the pressure $p_{\text{Maugis}}(r)$. The relationship between a and c can be obtained by equating the gap between the two surfaces at $r = c$ to h_c, which leads to

$$\frac{\bar{\lambda}\bar{a}^2}{2}\left\{ (\bar{m}^2 - 2)\sec^{-1}\bar{m} + \sqrt{\bar{m}^2 - 1} \right\} + \frac{4\bar{\lambda}^2\bar{a}}{3}\left\{ \sqrt{\bar{m}^2 - 1}\sec^{-1}\bar{m} - \bar{m} + 1 \right\} = 1, \tag{5.19}$$

in which $\bar{m} = c/a$ and $\bar{a}$ is the none-dimensional radius of the contact area

$$\bar{a} = a \left(\frac{4E^*}{3\pi\gamma R^2} \right)^{1/3} .$$

(5.20)

By controlling the value of $\bar{\lambda}$, the ratio of $\bar{m} = c/a$ can be controlled. Therefore the effective range of the adhesive tensile pressure outside the contact area can be controlled. The non-dimensional variable $\bar{\lambda}$ acts as a control parameter for the transition from the JKR extreme to the DMT extreme. For example, if $\bar{\lambda}$ is large, $\bar{m} \to 1$, which means that the effective range of the pressure outside the contact area is small, i.e. $h_c \to 0$ and $\sigma_0 \to \infty$, thus the JKR extreme is achieved. Similarly, the DMT extreme is achieved when $\bar{\lambda}$ is small. Using Eqs. (5.16)-(5.20), the adhesive contact law of the Maugis theory can be obtained. A more general form of the Maugis contact law is given below by using non-dimensional groups that

$$\bar{F} = F/(\pi R\gamma) ,$$

(5.21)

$$\bar{\delta} = \delta \left(\frac{16E^{*2}}{9\pi^2\gamma^2 R} \right)^{1/3} .$$

(5.22)

The contact law relating the normalized contact force $\bar{F}$ and the normalized displacement $\bar{\delta}$ can be obtained using

$$\bar{F} = \bar{a}^3 - \bar{\lambda}\bar{a}^2 \left\{ \sqrt{\bar{m}^2 - 1} + \bar{m}^2 \sec^{-1} \bar{m} \right\}$$

(5.23)

and

$$\bar{\delta} = \bar{a}^2 - \frac{4}{3}\bar{\lambda}\bar{a}^2 \sqrt{\bar{m}^2 - 1} .$$

(5.24)

Two Maugis contact laws with $\bar{\lambda} = 0.058$ and $\bar{\lambda} = 0.58$ is plotted in Fig. 5.2, where the transition between the JKR extreme and the DMT extreme is clearly illustrated.
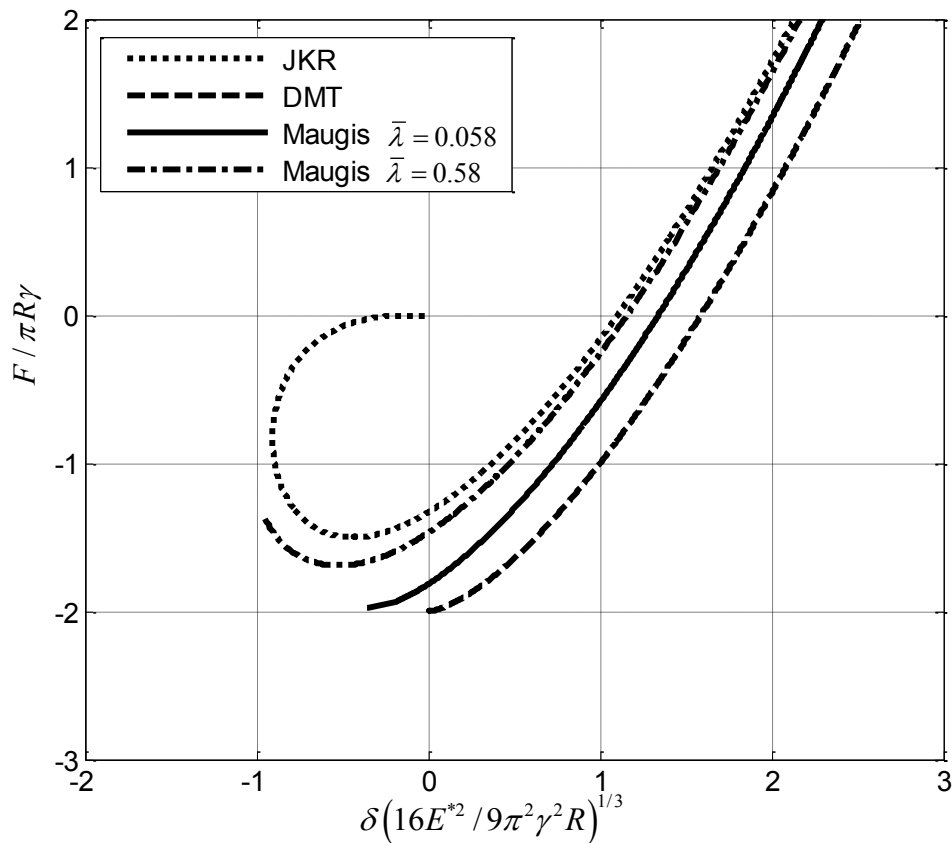
Fig. 5.2 Three representative analytical adhesive contact laws. Two Maugis contact laws are plotted using the control parameter $\bar{\lambda} = 0.058$ and $\bar{\lambda} = 0.58$.

Theories of the elastic adhesive contact following the Maugis' work were focusing on revising the shape of the adhesive tensile pressure outside the contact area described by Eq. (5.13) to more realistic but still analytically explicit forms. For example, Greenwood and Johnson (1998) presented a 'double-Hertz' approach in order to derive a distance dependant adhesive tensile pressure outside the contact area. The shape of the adhesive tensile pressure is the subtraction of a Hertz contact pressure from another Hertz contact pressure (applied on different contact areas). Schwarz (2003) combined the two extremes JKR theory and DMT theory together in order to obtain a smooth transition between the JKR theory and DMT theory. Schwarz (2003) implicitly assumed that the adhesive pressure outside the contact area is a linear combination of the infinitely large JKR pressure at the edge of the contact area and

the small but longer range DMT adhesive surface traction outside the contact area. An important conclusion was drawn by Barthel (1997) as follows. Having tried different expressions of the adhesive tensile pressure outside the contact area, Barthel (1997) demonstrated that the details of the shape of adhesive tensile pressure distribution outside the contact area have little influence on the adhesive contact law. What is important for the elastic adhesive contact law is the value of the specific surface energy γ, the size and the elastic parameters of the spherical particle. Therefore, the Maugis theory described by Eqs. (5.13)-(5.24) can be regarded as a representative analytical model of the adhesive contact between elastic spherical particles.

5.1.3 The Numerical approach

One drawback of the analytical approach is that it is unable to address the material response of the adhesive surface traction outside the contact area. In all analytical models, the values of the adhesive tensile pressure outside the contact area values have to be set as the adhesive surface traction. This issue can be resolved by numerical iterations of the interplay between the deformation and adhesion. As introduced in section 1.4.2, the relatively 'realistic' inter-atomic force may be calculated though the Lennard-Jones potential:

$$U_{L-J}(s) = 4\tilde{e}\left[\left(\frac{\varepsilon_0}{s}\right)^{12} - \left(\frac{\varepsilon_0}{s}\right)^{6}\right].$$
(5.25)

In Eq. (5.25), s is the inter-atomic distance, $\tilde{e}$ is a constant representing the minimum of the potential, and ε_0 is the inter-atomic distance corresponding to zero inter-atomic potential. The adhesion force per unit area between two surfaces can be obtained by integrating Eq. (5.25) over the volumes (Argento *et al.*, 1997). Specifically, if the two surfaces are infinite planar surfaces, then the resulting adhesion force per unit area will only contain a normal component, which is the adhesive surface traction given by

$$\sigma_a(h) = -\frac{8\gamma}{3\varepsilon_1}\left[\left(\frac{\varepsilon_1}{h}\right)^3 - \left(\frac{\varepsilon_1}{h}\right)^9\right],$$
(5.26)

where h is the gap between the two surfaces, ε_1 is the distance corresponding to zero adhesive surface traction between two infinite surfaces

$$\varepsilon_1 = (2/15)^{1/6}\varepsilon_0.$$
(5.27)

The details of derivation for Eq. (5.26) and Eq. (5.27) are presented in APPENDIX V. In the numerical approach, the adhesive surface traction between two planar surfaces (Eq. (5.26)) can be also applied on spherical particles due to the Derjaguin's approximation in Eq. (5.8). Using the Derjaguin's approximation, the problem of adhesive contact between elastic particles can be solved numerically. The general surface displacement on the surface of a half space $\bar{u}_z(r)$ under an arbitrary axisymmetric pressure distribution $p(r)$ is given by elastic analysis as

$$\bar{u}_z(r) = \frac{1}{E^*}\int p(\hat{r})G(r,\hat{r})\hat{r}d\hat{r},$$
(5.28)

where

$$G(r,\hat{r}) = \begin{cases} \dfrac{4}{\pi r}\hat{K}\left(\dfrac{\hat{r}}{r}\right), & \hat{r} < r \\ \dfrac{4}{\pi r}\hat{K}\left(\dfrac{r}{\hat{r}}\right), & \hat{r} > r \end{cases}$$
(5.29)

and $\hat{K}$ is an elliptic integral of the first kind. Based on the parabolic profile assumption (Eq. (1.11)), the gap h can be obtained on a arbitrary radial distance r that

$$h(r) = -\delta + \varepsilon_1 + r^2/2R + \bar{u}_z(r).$$
(5.30)

In Eq. (5.30), the gap between two surfaces $h(r)$ is allowed to be smaller than the distance ε_1 corresponding to zero adhesive surface traction. The adhesive surface

traction is allowed to repel the two surfaces, representing the pressure within the contact area.

Equations (5.26)-(5.30) can be solved using iterative numerical schemes. Starting from an undeformed spherical particle approaching a rigid wall, the adhesive surface traction is calculated according to Eq. (5.26). The resulting deformation is then calculated from Eq. (5.28). Then the new status of the surface is obtained from Eq. (5.30). The interplay between the deformation strain energy and the surface energy is therefore determined. However, this numerical approach is in fact an iterative solution of the Derjaguin's approximation used in Eq. (5.8) and the parabolic profile of the Hertz theory used in Eq. (5.30), which have to be satisfied in the first place. The results of the above numerical procedure are rather similar to those of the analytical approaches in section 5.2.2 and are not able to go beyond the scope of the analytical solutions. A weakness of the iterative procedure is that the underlying assumptions become less appropriate as the deformation becomes large (Parker and Attard, 1992). As pointed out by Feng (2000), even when deformation is still small, Eqs. (5.26) and (5.30) may break down for particles of small radius R and large values of Tabor's parameter $\bar{\mu}$, because the large effect of adhesion changes the particle shape near the contact area.

An important phenomenon predicted by both the analytical and numerical approach is the finite initial contact area, which is known as the jump-into contact (see e.g. Feng, 2000). As shown in Fig. 5.2, the contact law may have ultimate large tangent at the maximum negative displacement (maximum elongation), representing an instability during the adhesive contact. As the particle approaches the rigid wall, the adhesion force keeps increasing and can be so large that the shape of the particle changes due to elastic deformation. The particle surface near the rigid wall becomes unstable and jumps into contact within an infinitesimal time period. The contact area is initialized in a finite size rather than point contact. Numerically, the curve of the contact law can be S-shaped, having several points with infinitively large tangents, which represent unstable points where the contact may undergo sudden changes. Similarly, the contact

area terminates in a finite size of contact area after the maximum force reaches the pull-off force. Due to the multiple unstable regions on the force-displacement curve, the maximum tensile force during loading is not necessarily equal to the maximum tensile force during unloading. The maximum elongation may be different during loading and unloading as well. The loading and unloading curves of elastic adhesive contact can be therefore different in terms of the tensile response.

5.1.4 Some vital issues

In practice, the situation can be even more complicated. The adhesion is intensively influenced by the surface roughness and contaminations. That is why most particles are able to flow rather than stick together (Kendall, 2001). The contact between particles is actually the contact between surface asperities, which are usually in the order of nanometers for fine particles. Although the contact of asperities is often considered as a collection of DMT-like contacts. However, the DMT theory has been proved to be inaccurate at such a small scale. Despite the unrealistic DMT assumption that the adhesion will not create any further deformation, the pressure on the surface is so large that the contact always deforms plastically rather than elastically (Rimai *et al.*, 2000; German, 2003). Rimai *et al.* (2000) reported their experimental discovery that, due to the large stress produced by the adhesion, fine particles with submicron size will deform plastically merely under gravity. Since there is no established theory on the pressure distribution in the adhesive plastic contact, it is difficult to follow the analytical approach to solve the adhesive plastic contact problems. A popular approach to model the adhesive plastic contact is to apply the JRK pressure (e. g. Gu and Li, 2008) or DMT pressure (e.g. Sahoo and Banerjee, 2005) on the classical plastic contact theory. However, despite the huge difference between the elastic and plastic contacts, the effect of adhesion can be so significant that it is questionable if the pressure distribution on the surface will be still the same. Similarly, the elastic theory based on the numerical iteration scheme fails for fine particles undergoing plasticity.

Based on practical observations of the contact between fine particles, three issues are worthy of attention. Firstly, as the size of particles decreases, the assumptions of the Hertz theory and the Derjaguin's approximation may break down. Therefore, a full numerical method is required to address the size effect of the particles. Secondly, the interactions between the plastic deformation and adhesion are unknown. Particularly, whether there is any change in the adhesion in presence of plasticity, or if there is any change in the plastic behaviour in presence of adhesion. Thirdly, the effect of surface roughness is ubiquitous and important for adhesive contact. The goal of the present chapter is to investigate (a) if the classical contact laws can still be used for fine particles; (b) what is the dominant factor affecting the contact law; and (c) the size effect of nano particles on the contact law.

The next section presents a new multi-scale model which based on the continuum Material Point Method (MPM) and the atomistic Molecular Dynamics (MD), in order to simulate the adhesive contact. Section 5.3 addresses the size effect of the particle and explores if the analytical theories outlined above still work for fine particles. Section 5.4 focuses on realistic contact laws when plasticity and surface roughness play a role. The major conclusion of this study is that it is necessary to use a full numerical method to obtain the contact laws for the adhesive contact between fine particles.

5.2 MATERIAL POINT MODEL WITH INTER-ATOMIC FORCES

5.2.1 Brief overview

Considering the nature of adhesion, the adhesive contact between spherical particles is a typical problem that couples large scale continuum problems with micro scale inter-atomic interactions. In recent years, methods combining atomic simulations with continuum simulations have been studied intensively in order to introduce detailed material information into continuum models. The Finite Element (FE) method is generally used to simulate large scale continuum. The Molecular Dynamics (MD)

method is preferred to simulate a small region, where details of atomic interactions are required. In order to combine the FE region with the MD region, an FE-MD transition zone is introduced (see Kohlhoff *et al*., 1991 for example). Inside the transition zone, the FE nodes and MD atoms are coupled using various mapping schemes. Various issues arise such as mesh distortions in large deformation problems, ghost forces due to the inconsistency between the finite element and the atomistic models, and mismatch between the time scales of the two models.

Recently a new FE-MD coupling method was suggested by Lu *et al*. (2006). Instead of using the conventional FE method, Lu *et al*. (2006) employed the Material Point Method (MPM) to couple with the MD method. The material points within the interested zone are refined hierarchically until the size of the material points reaches the atomic size. Since both the MPM and MD are point based methods, the coupling within the MPM-MD transition zone is natural. Within the transition zone, the material points are boundary points for both atoms (MD zone) and material points (MPM zone). The velocity of these boundary points are determined by MD simulation. Then these velocities are used as boundary conditions for the MPM simulation, in order to update the positions of all the material points. The updated material points in the transition zone are used as boundary points of the MD simulation, causing the change of the inter-atomic potential and further velocity change of the MD zone (excluding the boundary points). The problem of mesh distortion is automatically resolved because the material point method uses a fixed background mesh.

A major problem of the coupled continuum and molecular dynamic model is that the time step length is controlled by the atomistic model which has to be extremely small. The total physical time that can be achieved in the simulations is in the order of pico-seconds. Most of the practical events, including the adhesive particle contact studied in this thesis, take much longer time and are therefore beyond the capacity of the model. The purpose of this work is to develop an alternative approach to the direct coupling between the MPM and the MD models. The key idea here is to entirely constrain the atoms embedded in the continuum model so that they can only move with the continuum solid (elastically or plastically) while the inter-atomic forces are

taking into account as in the usual molecular dynamic model. The deformation mechanism is therefore assumed through the constitutive law of the continuum material rather than computed from the atomic model. The model is therefore unable to capture events like dislocation formation and interaction, solid state diffusion and etc. However the approach is entirely appropriate to study adhesive particle contact as the mechanism of deformation is not the issue. As shown in Fig. 5.3, by refining the material points near the contact area, the distances between material points are in the range of inter-atomic distance. A virtual mirror particle is used to calculate the interaction between the two particles. Only the inter-atomic forces between atoms on different particles are considered and are treated as the external forces and applied on the material points to simulate the adhesion force. For simplicity, the term 'MD' is still used in the present model. However, one needs to bear in mind that the full MD model is not used in the present model. Instead, only the inter-atomic forces are considered while the atoms are constrained to deform with the continuum solid obeying the continuum constitutive law.

5.2.2 The Material Point Method

In order to extend the Material Point Method (MPM) to simulate the adhesive contact between fine particles, it is necessary to briefly outline the standard MPM formula. As shown in Fig. 5.3, the discretization in MPM is realised by concentrating the material density into material points. A background computational mesh is used to determine the movements of these material points. The discretized formula of MPM is given by Eqs. (2.9) and (2.10) and will not be repeated here. At each time step, the nodal acceleration is solved at the background mesh by Eq. (2.10). Then the computational mesh can be discarded and new computational mesh is used for the next time step. Problems associated with large deformation are therefore automatically overcome because the material points do not connect to any mesh.
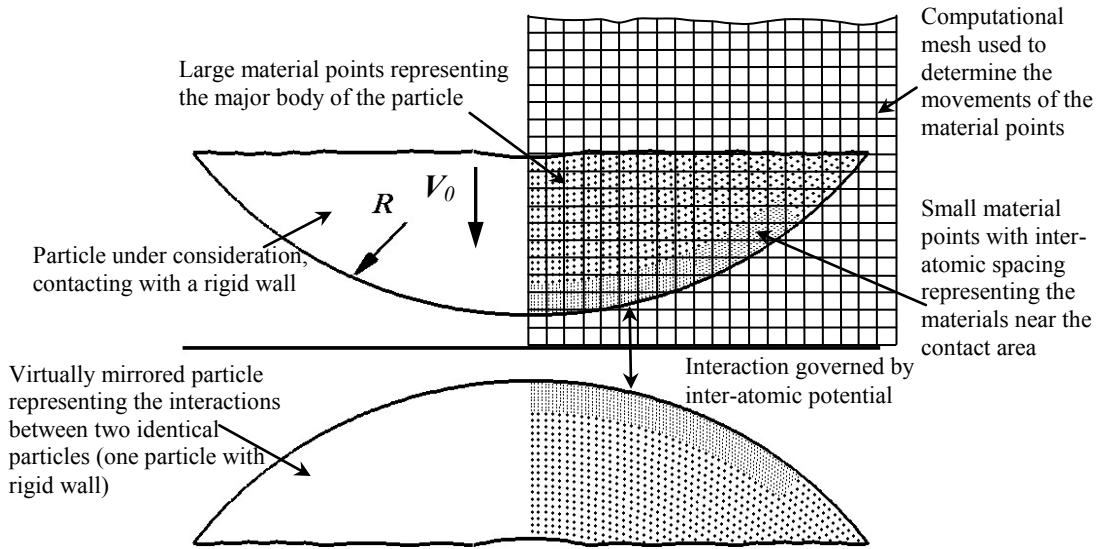
Fig. 5.3 Illustration of the Material Point Method coupling with the inter-atomic forces for adhesive contact problem.

5.2.3 Inter-atomic forces and Molecular Dynamics

The Molecular Dynamics (MD) method is introduced in section 1.5.2. The adhesive contact between fine particles was studied using MD in the publication of Kendall *et al.* (2004), which assumed that there is an inter-atomic potential between any two atoms. The force between two atoms depends on the distance between them, s_{ij}, and is expressed through a potential function $U(s_{ij})$, where i, j represent the atom indices. By taking the spatial derivation of the potential function, the inter-atomic force $\mathbf{f}_{ij}$ between each pair of atoms can be obtained:

$$\mathbf{f}_{ij} = -\nabla U(s_{ij}).$$ (5.31)

Similar to the Lennard-Jones potential in Eq. (5.25), the inter-atomic force $\mathbf{f}_{ij}$ in Eq. (5.31) is attractive if the distance between the two atoms is larger than the equilibrium distance. This attraction decreases when s_{ij} is increased further, and is often considered small enough to be ignored when the distance between two atoms is larger

than the cut-off distance, i.e., when $s_{ij} > \varepsilon_c$. If the distance between two atoms is smaller than the equilibrium distance, there is a strong repelling force increasing rapidly to stop s_{ij} from decreasing further. If a material body is constructed by an array of atoms representing a realistic atomic structure, then the force between each two atoms can be computed from the inter-atomic distance s_{ij} by Eq. (5.31). The acceleration $\dot{\mathbf{v}}_i$ of the i th atom is calculated by

$$m_i \dot{\mathbf{v}}_i = \mathbf{f}_i = \sum_{\substack{j=1 \\ (j \neq i)}}^{Nm} \mathbf{f}_{ij} \tag{5.32}$$

where Nm is the number of atoms, $\mathbf{f}_i$ is the sum of the force produced by the other $Nm-1$ atoms and m_i is the mass of the i th atom. Unfortunately, due to computational limitations, only a small number of atoms can be simulated.

5.2.4 Inter-atomic potential functions

The core of MD simulations is the potential function, which defines the way atoms interact with each other. The precision of MD simulations depends on whether the potential function is able to accurately describe the inter-atomic interactions. Potential functions based on quantum mechanics can be employed if details of the inter-atomic potential are required. However, the most frequently used potential functions in the simulation of materials are empirical potential functions. By abstracting atoms into mechanical dots with mass, these empirical potential functions contain free material explicit parameters, such as atomic charge, Van der Waals parameters, the equilibrium bond length between atoms, angles between atomic bonds, etc. These parameters are obtained by fitting against either the results of quantum mechanics or experimental material properties such as elastic constants.

The simplest and most straightforward idea is to use pair potential functions, which assumes that the total potential of a collection of atoms can be represented by the summation of the potential between each pair of atoms. The Lennard-Jones potential function of Eq. (5.25) is a typical pair potential function, which is often used to

calculate Van der Waals forces. The interactions between a group of three atoms (three body interactions) become important when the number of covalent bonds in the material increases. Erkoc (1997) reviewed 35 three body potential functions, in which the angle between atomic bonds is an important parameter. Another type of empirical potential functions is obtained by using the embedded atom method (EAM). By considering the potential when embedding an atom into a background electron field, the EAM potentials contain the parameters of electron densities and are often used to simulate metallic systems (e.g. Foiles *et al.*, 1986).

5.2.5 Incorporating inter-atomic forces into MPM

A typical adhesive contact between spherical particles is illustrated in Fig. 5.3. A particle of radius R contacting with a rigid wall is given an initial normal velocity V_0 towards the wall. As shown in Fig. 5.3, the problem is analysed using an axisymmetric formulation. Therefore, only half of the sphere is discretized into material points. The 'MD' zone is defined in the area covering the possible contact area, with the thickness of $8\varepsilon_0$. The material points inside the 'MD' zone are refined to the level of atom spacing, the distances between the atoms are set as being equal to or smaller than the equilibrium distance ε_0. A square computational mesh is employed to cover the domain of motion of the particle during the contact. Ideally, the spherical particle can be of any size but in the present research only particles of relatively small size are considered given the interest for simulating fine particle behaviours. The size range used in the present research is between 100 nm to 1 μm in diameter, which is far beyond the maximum scale of any full MD model.

In order to correctly represent the adhesive contact between two identical spherical particles, a mirror image of the particle is used. As shown in Fig. 5.3, at each time step, the material points in the mirror image particle are obtained by considering symmetrical material points to the original particle with respect to the rigid wall. For convenience, the original particle is named as body I and the mirror image is named as body II. A pair potential function is employed to represent the inter-atomic

interactions between the two particles. In the present research, we use the Erkoc potential function (Erkoc, 1993). The potential function between two atoms is expressed by

$$U(s_{ij}) = D_{21}U^{21}(s_{ij}) + D_{22}U^{22}(s_{ij}) \tag{5.33}$$

where

$$U^{2k}(s_{ij}) = A_k s_{ij}^{-\hat{\lambda}_k} \exp\left[-\alpha_k s_{ij}^2\right], \quad k = 1,2. \tag{5.34}$$

Similar to the Lennard-Jones potential, the Erkoc potential function in Eqs. (5.33) and (5.34) depends on the distance between two atoms s_{ij}. U^{21} represents the repulsive part and U^{22} represents the attractive part. D_{21} and D_{22} are the coefficients of the linear combination of U^{21} and U^{22}. A_k, λ_k, and α_k are material explicit parameters determined from experimental data. Parameters used to simulate copper by Eqs. (5.33) and (5.34) are shown in Table 5.1. The Lamé constants λ and μ, consistent with the Erkoc potential function, the density ρ, as well as specific surface energy γ (obtained from the publication of Foiles *et al.*, 1986) are also shown in Table 5.1.

Table 5.1 Parameters of copper for the Erkoc potential function. The distances are in $\overset{\circ}{A}$ and the energies are in eV.

Parameter	Value	Parameter	Value
A_1	110.766008	A_2	−46.1649783
$\hat{\lambda}_1$	2.09045946	$\hat{\lambda}_2$	1.49853083
α_1	0.394142248	α_2	0.2072255507
D_{21}	0.436092895	D_{22}	0.245082238
λ (GPa)	134.7	μ (GPa)	25.3
γ (J/m^2)	1.17	ρ (kg/m^3)	8900

The requirement of using the Erkoc potential function Eqs. (5.33) and (5.34) is to use the distance between two atoms s_{ij} in the unit of $\overset{\circ}{A}$, and the resulting potential energy in the unit of eV . As shown in Fig. 5.3, the 'MD' zone covers the regions near the contact between the two particles. In the full MD simulation, the inter-atomic potential inside one particle should lead to the continuum constitutive law, which is already available in the atom-sized material points. Therefore, the inter-atomic potential in the present model is only used to account for the adhesion between the two different particles, i.e. the inter-atomic potential only applies between the material points on different particles (one from body I and another from the mirror image body II). The force acting on one atom-sized material point is calculated as

$$
\underset{(i \in \text{body I})}{\mathbf{f}_i} = \sum_{\substack{j=1 \\ (j \in \text{body II})}}^{Nm} \mathbf{f}_{ij} = \sum_{\substack{j=1 \\ (j \in \text{body II})}}^{Nm} \left(\frac{\partial U(s_{ij})}{\partial s_{ij}} \right) \frac{\mathbf{s}_{ij}}{s_{ij}} , \tag{5.35}
$$

where $\mathbf{s}_{ij}$ is the vector from the ith atom-sized material point to the jth atom-sized material point. The use of a cut-off distance can greatly reduce the computational time. The resulting force from Eq. (5.35) is then considered as applied external forces of the MPM formula Eq. (2.10) and treated as body force in Eq. (2.9). Due to the property of the inter-atomic potential function, this external force behaves as a large repulsion if two atom-sized material points belonging to different particles get very close to each other, i.e. when the particle is contacting with the rigid wall. The vertical velocity and acceleration of the contacting material points will reduce to zero. The frictionless boundary condition is automatically achieved. Zero velocity and acceleration boundary conditions at the bottom nodes on the background mesh are also applied in the present model. In fact, such boundary condition is also proved to be useful in smoothing the numerical oscillations generated by the huge inter-atomic force.

'Axisymmetric' approximation of the atom-sized material points is employed. As shown in Fig. 5.4, each material point represents an axisymmetric ring of material. Therefore, a ring-to-ring interaction has to be obtained in the present model instead of the atom-to-atom interaction used in a full MD models. The approximation is to treat the rings consisted by infinitely thin 'atoms', which are continuous within each ring.

Those infinitely thin 'atoms' are represented in Fig. 5.4 as di and dj, which are governed by the distance dependent inter-atomic potential. The ring-to-ring force can then be calculated by integrating the force between all pairs of infinitely thin 'atoms'. As shown in Fig. 5.4, the distance between two arbitrary points di and dj on the two rings is represented by s_{didj}. Obviously, s_{didj} is a function of the angles $\hat{\theta}_i$ and $\hat{\theta}_j$, the radii of the two rings R_i^0 and R_j^0, and the vertical distance $\hat{h}_{ij}$ that

$$s_{didj} = \left((R_i^0)^2 + (R_j^0)^2 - 2R_i^0 R_j^0 \cos\hat{\theta}_j + \hat{h}_{ij}^2 \right)^{1/2}. \tag{5.36}$$

The force applied on the ring of atom i produced by the ring of atom j is give by

$$\mathbf{f}_{ij}^{\text{axisymmetric}} = \int_0^{2\pi} R_i^0 \int_0^{2\pi} R_j^0 \left(\frac{\partial U(s_{didj})}{\partial s_{didj}} \right) \frac{\mathbf{s}_{ij}}{s_{ij}} d\hat{\theta}_i d\hat{\theta}_j, \tag{5.37}$$

where $\mathbf{f}^{\text{axisymmetric}}$ denotes the 'axisymmetric inter-atomic force' used in the present axisymmetric model. The total force applied on the i th atom-sized material point is therefore
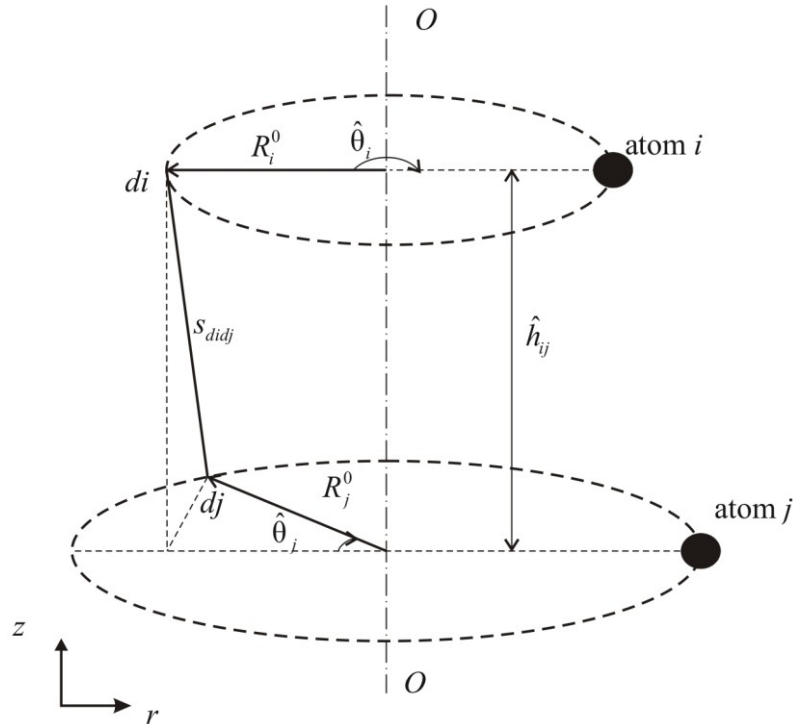

Fig. 5.4 The integration scheme used to calculate the ring-to-ring interaction force.

$$\mathbf{f}_i^{\text{axisymmetric}} \atop (i \in \text{body I}) = \sum_{\substack{j=1 \\ (j \in \text{body II})}}^{Nm} \mathbf{f}_{ij}^{\text{axisymmetric}} \qquad (5.38)$$

Equations (5.36)-(5.38) are explicit functions of the spatial coordinates and therefore Eq. (5.37) can be integrated. This axisymmetric approximation has greatly reduced the computational time of the model. However, it requires a modification to the potential function in Eqs. (5.33) and (5.34), because neither the sizes nor the structures of the atom-sized material points used in the present axisymmetric formula are as realistic as those used in full MD simulations. Comparing to the full MD simulation, the present model has no problem in simulating material properties since the material responses are governed by the continuum constitutive law in the MPM formulation. The simulation of adhesion is aided by a pre-test of the specific surface energy. By definition, the specific surface energy γ is pre-tested by putting two surfaces into the equilibrium position using the present axisymmetric approximation. Alternatively, for each case, the pre-test of putting two surfaces together is performed to obtain the surface energy parameters A_k in Eq. (5.34). Practically, only one pre-test is required when dealing with one new MPM discretization. With an arbitrary set of surface energy parameters A_1 and A_2, a trial specific surface energy value γ^{trial} is obtained. In the subsequent simulations, A_1 and A_2 are multiplied by a same factor $\gamma / \gamma^{\text{trial}}$ in order to obtain the required specific surface energy values. In the present research, the radius of the particle R varies between 50 nm to 500 nm. Different particle sizes may require different discretization of atom-sized material points. Before the simulation, a series of pre-tests is performed in order to obtain the input values of the surface energy parameter A_1 and A_2, for different particle sizes. Characteristic values of A_1 and A_2 for $\gamma^{\text{trial}} = 1$ J/m^2 are listed in Table 5.2. The advantage of the pre-test is that the atom-sized material points do not necessarily to conform to the actual atomic structure (nor is this possible in the axisymmetric formula) to be accurate enough to capture the specific surface energy between particles. However, the pre-test is not accurate enough to capture the change of the specific surface energy due to the change of the atomic structures. Although the change of specific surface energy after the change of atomic structures is small and

always ignored in most simulations, if this detail is required, then a three dimensional model using realistic atomic structures has to be used.

The procedure of incorporating the inter-atomic forces into the MPM in order to model the adhesive contact problems is summarized below. The material points in the 'MD' zone covering the contact area are refined to become atom-sized material points. At each time step, a mirror image body is used to determine the adhesion force between the particles. This adhesion force is calculated by considering the inter-atomic forces produced by each atom pair, one of which must come from the particle while another one must come from the mirror image. The inter-atomic forces are calculated using the axisymmetric approximation. Then the forces acting on each atom-sized material point are incorporated into the standard MPM formula as the body force. The standard MPM time step is performed and the adhesive contact between fine particles is simulated.

Table 5.2 Characteristic values of the specific surface energy parameters under a pre-test, for different kinds of mesh statuses.

	Different MPM discretizations for different particle sizes		
	$R = 500$ nm	$R = 250$ nm	$R = 50$ nm
Number of atom-size material points	11980	11910	18800
A_1 for $\gamma^{\text{trial}} = 1$ J/m^2	89.753	47.443	0.660
A_2 for $\gamma^{\text{trial}} = 1$ J/m^2	-37.407	-19.773	-0.275

5.2.6 Model validation

An elastic spherical particle in normal adhesive contact against a rigid wall, is simulated for model validation. The radius of the particle is set as $R = 0.5$ μm. As

analysed in section 5.1, such a small size would possibly lead to break down of the analytical solutions. A conservative choice is to use a small Tabor's parameter $\bar{\mu}$ in Eq. (5.12) for the particle so that the surface energy will not significantly change the profile of the particle, i.e. a DMT-like particle. The surface energy parameters A_k in Eq. (5.34) are therefore artificially set as small, with $A_1 = 0.727$, and $A_2 = -0.303$. Other parameters in the inter-atomic potential function are chosen as the same as those of the potential function for copper given in Table 1. The typical inter-atomic distance is found to be $\varepsilon_0 = 2.253$ nm. By the pre-test of putting two surfaces together into equilibrium position, the specific surface energy value is found to be $\gamma = 0.0081$ J/m^2. Other parameters are: Young's modulus $E = 71.9$ GPa, Poisson's ratio $\nu = 0.42$, and density $\rho = 8900$ kg/m^3. The elastic constants of the material are obtained from the publication of Erkoc (1993) to ensure that they are consistent with the Erkoc potential function. Initial velocity is chosen to be $V_0 = 1$ m/s under which the scope of small deformation is met. The Tabor's parameter $\bar{\mu}$ in Eq. (5.12) is calculated as *c.a.* 0.0722, which is small enough for the case to fall into the scope of the analytical solution.

As demonstrated in CHAPTER 3, the convergence of the MPM 2D axisymmetric model requires at least 94 material points per unit cell of the computational mesh on average. Therefore, the same mesh is employed to represent the main body of the fine particle. The material points which fall inside the 'MD' zone (with the thickness of 2 nm) are refined to reach the inter-atomic distance. A total of 358301 material points, including 11980 atom-sized material points, are used to represent the whole particle. A uniform square computational mesh is employed. The same computational mesh is used at every time step throughout the simulation in order to reduce the numerical errors.

Other numerical details include the numerical integration in Eq. (5.37). It was found that five-Gauss quadrature points are sufficiently accurate. The net force applied to the particle is obtained by the sum of the total nodal forces of the computational mesh excluding the nodes on contact boundary at each time step. As introduced in section

5.1, the particle undergoes elongation, i.e. negative displacement, before the contact. Such negative displacement is not captured by the displacement of the mass centre. Therefore, the displacement before the particles are in contact is measured by the change in the distance between the top and bottom material points on the particle. When the particle is in contact, the traditional displacement measure, i.e., the displacement of the mass centre of the particle is used. In the present model, Jaumann stress rate (introduced in CHAPTER 1) is used as the stress measurement in order to simulate large deformation problems. Typical MD cell subdivision techniques are used to determine the atom pairs in interactions. The cut-off distance of the inter-atomic force is chosen as $\varepsilon_c = 0.7$ nm. The time step is about 10 fs and the explicit Verlet leapfrog scheme (introduced in CHAPTER 1) is used for the time integration. The simulation of the full contact law (after the full rebound of the particle) takes about 40000 time steps running for about 10 cpu hours, which is much faster than any known MD simulation.

The model is validated by comparing the contact law obtained from the validating example with the Maugis theory. The results are normalized as in Eqs. (5.19)-(5.24). The early stage of the contact law is plotted in Fig. 5.5 in order to highlight the detailed tensile force. The solid line in Fig. 5.5 is the analytical prediction by the Maugis theory described by Eqs. (5.19)-(5.24). The numerical result is shown as discrete symbols in Fig. 5.5. Negative force denotes the tensile force due to adhesion, which produces negative displacement to elongate the particle. Despite small differences from either dynamic effect or the simplified adhesive surface traction employed by Maugis, the two solutions agree reasonably well with each other. It is also shown in Fig. 5.5 that the numerical model captures the force-displacement contact law before the contact area has been formed. The maximum tensile force (pull-off force) is found to be -2.4656×10^{-8} N by the present model, while -2.4504×10^{-8} N by the Maugis theory and $F_{\mathrm{DMT}}^c = 2\pi\gamma R = -2.5447 \times 10^{-8}$ N is the DMT pull-off force. The displacement obtained by the numerical model is always slightly larger than the analytical prediction. This is consistent with our expectations. As pointed out by Greenwood (1997), the maximum tensile pressure on the surface

lies slightly outside the contact area, at $r = a'$, where $a' > a$. In contrast, the analytical solutions always assume that the maximum tensile pressure lies on the edge of the contact area. i.e. $F = F(a')$, indicating the analytically predicted displacement is $\delta = \delta(a')$. While the true profile of the surface is $\delta = \delta(a)$, the analytically predicted displacement should be always slightly larger than the numerical results. Similar findings were also published by Attard and Parker (1992). The present model is therefore confidently validated.
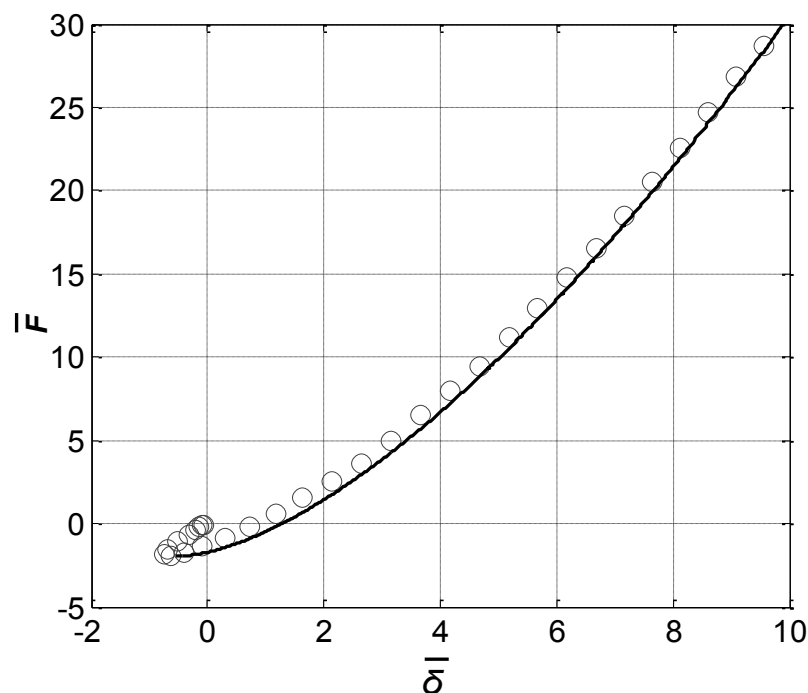
Fig. 5.5 The comparison of the normalized contact law between the Maugis theory (solid line) with the numerical results (circular symbols), in order to validate the present model. Only the early stage of the loading curve is shown to highlight the details of the tensile force.

5.3 SIZE EFFECT DURING ADHESIVE CONTACT BETWEEN ELASTIC SPHERICAL PARTICLES WITH SMOOTH SURFACES

The adhesive contact law is dependent on the particle size. In this section we consider particles that are spherical, pure elastic, and have atomically smooth surfaces. The specific surface energy is assigned as $\gamma = 0.11$ J/m^2, which is much larger than that

used in the validation example. Other material parameters are chosen as those corresponding to copper as used in the validation. The radius of the particles is varied from $R = 500$ nm, $R = 250$ nm, to $R = 50$ nm. The aim is to explore if the classical solutions are still valid for such small particles. It is expected that the effect of adhesion becomes more and more significant as the size of the particle get smaller and smaller. The contact laws of such particles are plotted in Fig. 5.6. All particles have the same initial normal velocity of $V_0 = 1$ m/s. The results presented are normalized into non-dimensional formats. Specifically, the force and displacement are normalised following Eqs. (5.21) and (5.22) as

$$\bar{F} = F/(\pi R \gamma) \tag{5.39}$$

and

$$\bar{\delta} = \delta \left(\frac{16E^{*2}}{9\pi^2 \gamma^2 R} \right)^{\frac{1}{3}}. \tag{5.40}$$

The contact time t is normalised by the total contact time of the Hertz contact such that

$$\bar{t} = t / \left[2.87(m^2 / RE^{*2}V_0)^{1/5} \right] \tag{5.41}$$

where m is the mass of the particle. Consequently the normalized total time of an adhesionless elastic contact is always equal to 1.

In Fig. 5.6(a), the column on the left hand side shows the normalized force-displacement curves for particles with different sizes. Analytical solutions are superimposed in the figure using the dash lines. The column on the right hand side shows the curves of the normalized force, which is the controlling variable in the contact law, against the normalized contact time. The normalized force-time curves for adhesionless particles are also superimposed. Figure 5.6(a) shows the contact curves for the particle of the largest size considered, $R = 500$ nm. Here the compressive force and displacement are taken as positive while tensile force and

displacement are taken as negative. It can be seen from Fig. 5.6(a) that the analytical solution is generally valid for large particles such as in the case of $R = 500$ nm. However, for a transient contact problem there is no analytical solution for the maximum contact force, which is one of the most important characteristics of the contact law. At the beginning of the contact, when the particle has not yet in contact with the wall, there is a tensile force trying to attract the particle to the wall. The tensile force increases as the elongation increases. In Fig. 5.6(a), the elongation reaches its maximum value before the tensile force does, indicating the beginning of the actual contact. Afterwards the tensile force continues to increase. From the right hand side of Fig. 5.6(a), it can be seen that the tensile force increases very slowly at the beginning and suddenly jumps to a maximum value. The value of the maximum tensile force is $-1.81\pi R\gamma$, which is consistent with the analytical prediction in the interval of $-1.5\pi R\gamma$ to $-2\pi R\gamma$. After the maximum tensile force is reached, the contact force starts to increase and the curve starts to ascend. Zero displacement is reached before zero force does, when the particle is compressed with a displacement value of $\delta = \left(16E^{*2}/9\pi^2\gamma^2 R\right)^{-1/3}$. After the force and displacement all become compressive, the contact law behaves similarly to the elastic Hertz contact law. It can be also observed that the maximum force value of the adhesion contact is slightly larger than that of the elastic Hertz contact (recalling that the specific surface energy is set as $\gamma = 0.11$). The unloading curve is almost the same as the loading curve, except for a slightly larger maximum elongation when the particle is pulled off the wall. The major difference between the numerical contact law and the analytical one is their deviations on both tensile and compressive sides of the force curve. These sudden changes result from the unstable increase in the contact area during loading and unstable decrease in contact area during unloading. As introduced in section 5.1, the adhesion contact jumps-into and jumps-off contact within an infinitesimal time period in an unstable manner. As shown in Fig. 5.6(a), the gain and reduction in the contact area are also unstable. Each turning point represents a sudden drop or increase in the force, within an infinitesimal time period. Therefore, the jump-to-gain and jump-to-lose contact have been captured by the present numerical model for fine particles.
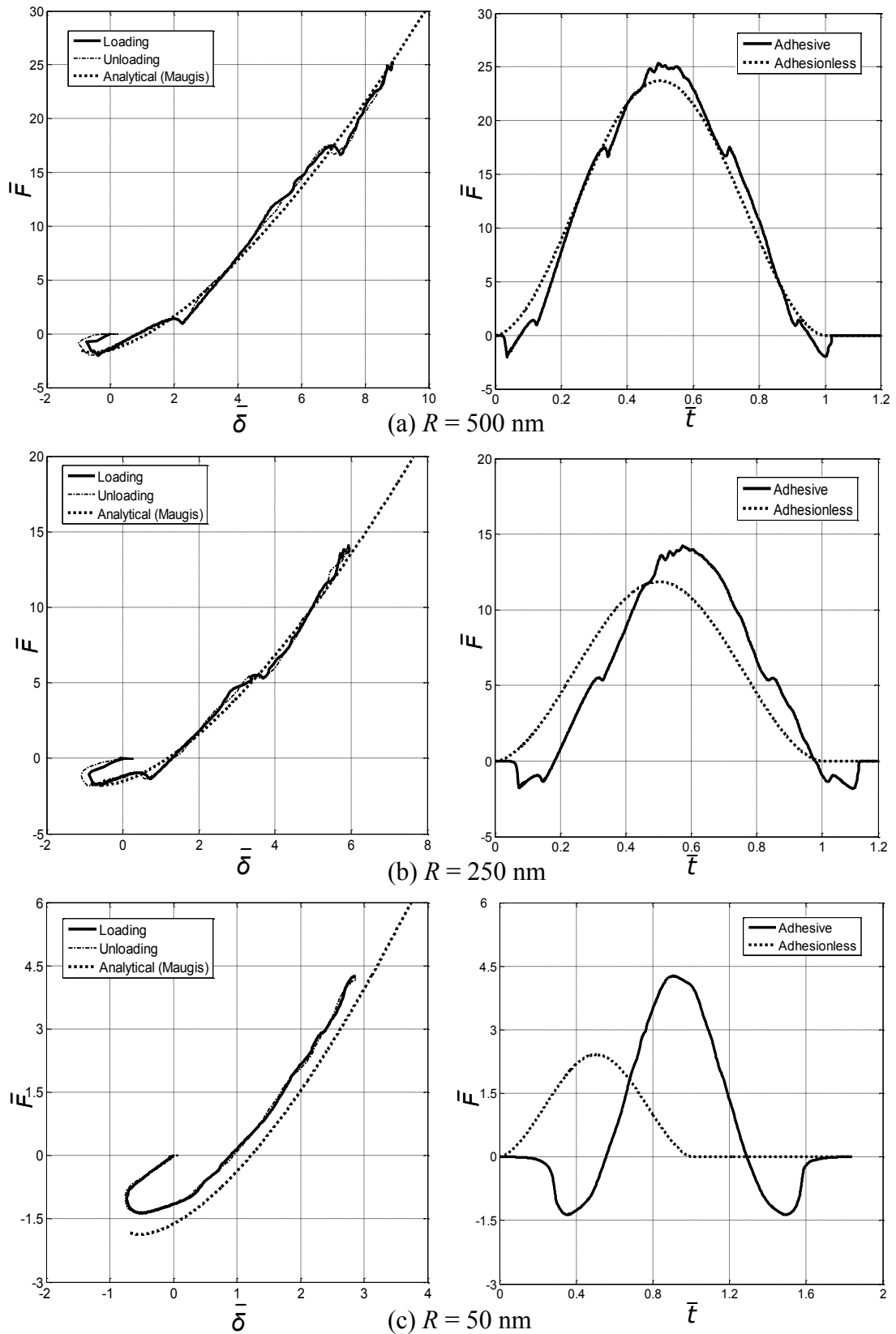
Fig. 5.6 Normalized contact curves for elastic spherical particles with specific surface energy $\gamma = 0.11$ J/m^2, and initial velocity $V_0 = 1$ m/s. (a) $R = 500$ nm, (b) $R = 250$ nm, and (c) $R = 50$ nm. Left column: force-displacement curves comparing to analytical solutions. Right column: force-time curves comparing to adhesionless contacts.

Figure 5.6(b) shows the contact curves for the particle size of $R = 250$ nm. The curves are similar to the curves in Fig. 5.6(a) and the analytical prediction is relatively accurate. Analytically, a small particle has a small Tabor's parameter, defined as $\bar{\mu} = (R\gamma^2 / E^{*2}\varepsilon^3)^{1/3}$, and should be more DMT like, i.e., the value of the maximum tensile force should be closer to $-2\pi R\gamma$ for the particle of $R = 250$ nm than that for the particle of $R = 500$ nm. However, the maximum tensile force is $-1.69\pi R\gamma$ and is more JKR like than in Fig. 5.6(a). The numerical results therefore reflect the limitations of the analytical solution for small particles. The gap between the contacting surfaces is compressed and results in a repelling force, in opposite direction to the tensile force. Therefore, the maximum tensile force is always smaller than that predicted by the analytical solution. As the size of particle decreases, the effect of the compression on the gap becomes more significant and cannot be ignored. That is why in Fig. 5.6(b) shows a more JKR like behaviour for a more DMT like particle. As seen on the right hand side of Fig. 5.6(b), the maximum compression force is much larger than that for adhesionless contact, indicating an increase in the contact area when adhesion is present. The ratio between the maximum tensile force and the maximum compressive force is larger than that in Fig. 5.6(a), indicating a more significant effect of adhesion as the size of particle decreases. Unstable jumps are also observed in the contact curves of the particle of $R = 250$ nm.

Figure 5.6(c) shows the contact curves for the particle size of $R = 50$ nm. It can be seen that the contact law has shifted upwards from the analytical predictions but still follow a similar trend. This is because the compression of the gap between contacting surfaces plays a more important role for a smaller particle size. The maximum tensile force is $-1.46\pi R\gamma$, which is even smaller than the JKR extreme of $-1.5\pi R\gamma$. The ratio between the maximum tensile force and the maximum compressive force is large. The maximum force is also much larger than that of the adhesionless contact. The effect of adhesion is therefore very significant at such a small scale, even the specific surface energy has been set as much smaller than most real materials. Unlike the contact curves shown in Fig. 5.6(a) and Fig. 5.6(b), there is only one jump on the loading and unloading curve each representing the jumps-into and jumps-off contact.

The processes of further gaining and losing contact are stable. This is because it is easier for a smaller particle to maintain its shape against the adhesive surface traction.

According to the above results and analyses, it may conclude that the classical approaches introduced in section 5.1 may be still useful for fine particles, except for some inaccuracies. However, for most metals such as copper, the value of specific surface energy is about $\gamma = 1$ J/m^2, which is much larger than the specific surface energy in the present section, that $\gamma = 0.11$ J/m^2. Moreover, plastic deformation and surface roughness are two important factors in the contact between fine particles. In order to simulate more realistic fine particles and obtain more representative contact laws, the next section focuses on particles of $R = 50$ nm, with surface roughness and plastic deformation. The adhesion contact for elastic spherical particle with realistic specific surface energy is studied in Fig. 5.7; the adhesion contact for elastoplastic spherical particle with realistic specific surface energy is studied in Figs. 5.8 and 5.9; the contact profiles at the maximum compression of different particles are plotted in Fig. 5.10, which also contains the profiles of the surface for a small specific surface energy particle ($\gamma = 0.11$ J/m^2) and an adhesionless contacting particle. Comparing to the $\gamma = 0.11$ J/m^2 particle studied in the present section with the adhesionless particle, it can be observed from Fig. 5.10 that the contact area has been increased by the existing of adhesion. The shape near the contact area is not changed significantly comparing to that of the adhesionless particle. This is possibly why the analytical solutions are roughly applicable for a fine particle with small specific surface energy, as shown in Fig. 5.6.

5.4 ADHESIVE CONTACT BETWEEN PARTICLES WITH REALISTIC FACTORS

5.4.1 Elastic spherical particles

Firstly, an elastic spherical particle with realistic specific surface energy is studied. The value of the specific surface energy is set as $\gamma = 1.17$ J/m^2 as for copper. The

normalized force-displacement curves and force-time curves are shown on the left hand side and right hand side in Fig. 5.7 respectively. The numerical oscillation is smoothened by taking an average of contact force value out of every 100 time steps. It can be immediately observed in Fig. 5.7 that the unstable jumps are prevailing and more intensive than those in Fig. 5.6. These jumps are represented by spikes on the curves heading downwards during loading and upwards during unloading. These spikes represent the intensive jump-to-gain and jump-to-lose contact and therefore, the adhesive contact at this 50 nm scale is a rather discontinuous process. Moreover, the displacement curves correspond to the deformation of the central axis of the particle, while the intensive instabilities are taking place at the edge of the contact area. The displacement-time curves are much smoother than the force-time curves. This is the reason why only normalized force-time curves are shown on the right hand side of Fig. 5.7.

Compared to the particle studied on the left hand side of Fig. 5.6(c), the difference between the particle studied on the left hand side of Fig. 5.7(a) is that the specific surface energy is increased by about 10 times. A common sense is that a particle of such a small size and large specific surface energy should be further away from the analytical solutions than the particle shown in Fig. 5.6(c) does. Interestingly, despite the unstable spikes, the loading curve of the contact law is consistent with the analytical solutions, except that the maximum elongation is only about half of the analytical solution. The maximum tensile force lies between the JKR extreme $-1.5\pi R\gamma$ and the DMT extreme $-2\pi R\gamma$, however the exact value is difficult to determine due to the instabilities. The reason why the large specific surface energy reduces the results back to the analytical solution can be explained as following. As the specific surface energy is 10 times larger, the gap between the contact surfaces is 10 times stiffer due to the properties of the inter-atomic potential function of Eqs. (5.33) and (5.34). It is more difficult to close the gap and the resulting repulsion to the maximum tensile force is relatively weakened. Figure 5.7(a) also shows that the unloading curve is no longer identical to the loading curve. At the same displacement, the force on the unloading curve is smaller than that on the loading curve,

representing a noticeable value of energy dissipation during adhesive elastic contact. As pointed out by Greenwood and Johnson (1998), this energy dissipation is due to the unstable jumps to gain or lose contact area during the loading and unloading. On the right hand side of Fig. 5.7(a), the maximum compressive force is much larger than the corresponding adhesionless contact. The contribution of the adhesion is so significant that the maximum tensile force is almost equal to the maximum compressive force.
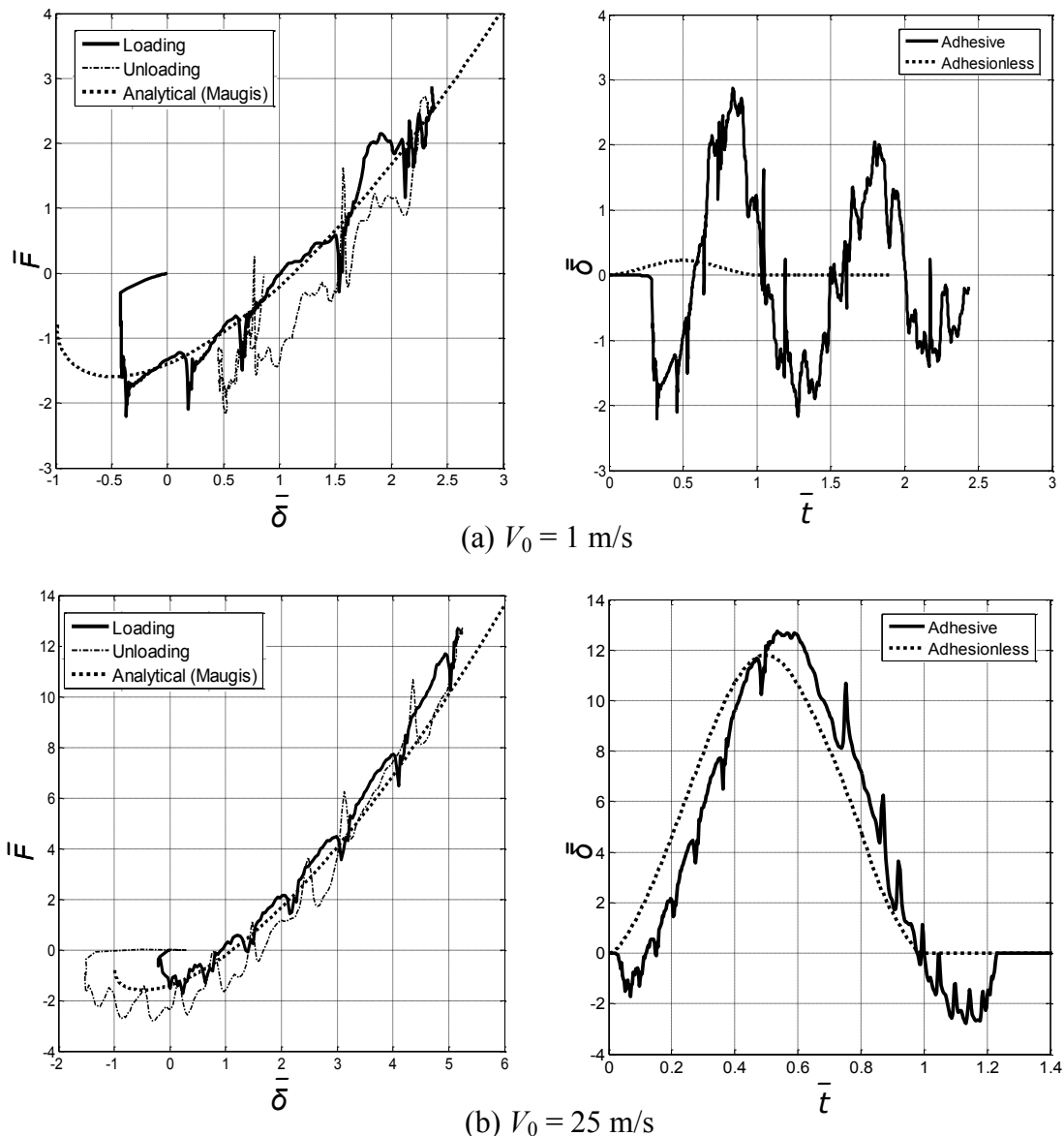
(a) $V_0 = 1$ m/s

(b) $V_0 = 25$ m/s

Fig. 5.7 Normalized contact curves for elastic spherical particles of size $R = 50$ nm ($\bar{R} = 630$) and realistic specific surface energy $\gamma = 1.17$ J/m^2, with different initial velocities. (a) Initial velocity $V_0 = 1$ m/s, (b) initial velocity $V_0 = 25$ m/s. Left column: force-displacement curves comparing to analytical solutions. Right column: force-time curves comparing to adhesionless contacts.

It is then instructive to study Fig. 5.10 for the profile of the particle which is discussed in Fig. 5.7(a). At the maximum compression, the profile of the particle is flattened due to adhesion. The profile of the particle is much steeper if the contact area is increased due to an increasing adhesion force. The shape of the profile near the contact area is more like a straight line rather than a parabola. The classical approach is unable to capture such a change in the shape of the profile. However, it is noted that the analytical solution still roughly predicts the contact law under a situation which severely violates the underlying assumptions.

One of the most important features of the contact curves shown Fig. 5.7(a) is that the particle does not rebound but sticks to the wall. As shown on the right hand side of Fig. 5.7(a), after the unloading, the maximum tensile unloading force is not strong enough to separate the particle from the wall. Reloading takes place due to the elastic vibrations of the particle. The force oscillates periodically about zero while unstable jumps are still taking place. The displacement oscillates smoothly about a compressive value, $\delta = 0.8\left(16E^{*2}/9\pi^2\gamma^2R\right)^{-1/3}$ as shown in Fig. 5.7(a). For clarity, the unloading curve on the left hand side of Fig. 5.7(a) has been cut off when the force is zero on reloading. Despite the unstable spikes, the following periodical reloading and subsequent unloading will be along the unloading curve. This phenomenon of particle sticking has a direct consequence to the flowability of particulate systems which is dramatically reduced when then size of the particles is decreased. The increase in the contact area releases a large amount of surface energy which cancels the effect of the initial kinetic energy. This is demonstrated by increasing the initial velocity to $V_0 = 25$ m/s, as shown in Fig. 5.7(b). In this case, the effect of initial kinetic energy becomes dominant and the adhesive particle rebounds from the wall. Comparing with the analytical solution, the contact law shown on the left hand side of Fig. 5.7(b) is similar but slightly stiffer. A significant difference from the analytical prediction is that the maximum elongation is much smaller during loading while much larger during unloading. As one can observe from the right hand side of Fig. 5.7(b) where the particle is subjected to a high initial velocity, the maximum tensile force during loading is of the same value for low velocity in Fig. 5.7(a). However, the

maximum tensile force during unloading is about 1.5 times of that during loading and exceeds the DMT extreme $-2\pi R\gamma$. Comparing to the force-time curves shown in Fig 5.7(a) and Fig. 5.6(c), the maximum tensile force is independent of the initial velocity during loading but dependent on the initial velocity during unloading. This is because the particle pull-off takes place at a finite contact area, which is much larger than the jump-in contact area during loading. When the particle is pulled off, this larger contact area releases larger surface energy, which increases the curvature near the contact area. The maximum elongation is therefore larger during unloading, indicating that the particle is stretched more with a larger tensile force, which can exceed the DMT extreme $-2\pi R\gamma$. The force-time curve on the right hand side of Fig. 5.7(b) is very similar to that of the corresponding adhesionless particle. Elastic deformation dominates during high velocity impact, which allows the particle to rebound at the end of the contact process.

5.4.2 Elastoplastic spherical particles

A unique advantage for the present model is that it is able to simulate large deformation plasticity as the stress is traced at the material points including the atom-sized material points. In the present research, an elastic perfectly plastic material is assumed. The yield strength Y is the only additional parameter. The details of the elastoplastic model using MPM has been presented in CHAPTER 3. In a pure MD model, the yield strength Y of the material is an outcome of the model prediction. However, the yield strength also strongly depends on the microstructure of the material, for example grain-size, second phase inclusions and etc. In our present model, the yield strength is an input parameter to the constitutive law. The classical plastic flow rule in conjunction with von Mises yield function is used despite that the nano-sized particles may have limited number of dislocation lines. By keeping other parameters the same as in section 5.4.1, particles of different yield strengths are studied in the present section. Plastic adhesive contact curves are shown in Fig. 5.8. Firstly, the particle is assigned a relatively high yield strength of $Y = 2$ GPa and an initial velocity of $V_0 = 1$ m/s. The contact curves are shown in Fig 5.8(a). Johnson

(1985) showed that for an adhesionless particle, the velocity required for plastic deformation, V_y, is given by

$$\frac{\rho V_y^2}{Y} = 26(Y/E^*)^4 \tag{5.49}$$

(a) $Y = 2\text{GPa}$, $V_0 = 1$ m/s
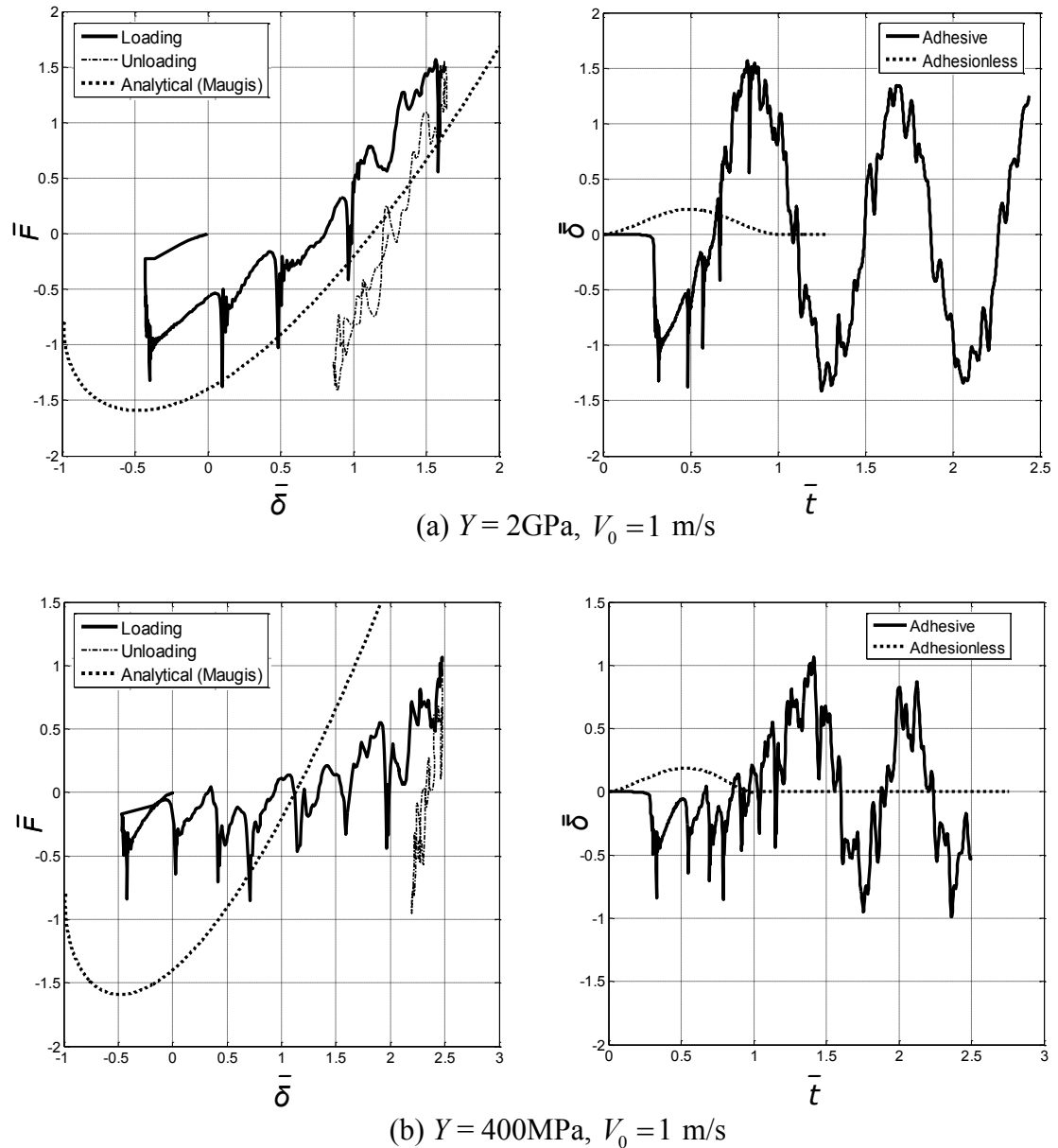
(b) $Y = 400\text{MPa}$, $V_0 = 1$ m/s

Fig. 5.8 Normalized contact curves for elastoplastic spherical particles of size $R = 50\,\text{nm}$ ($\bar{R} = 630$), realistic specific surface energy $\gamma = 1.17$ J/m^2, and small initial velocity $V_0 = 1$ m/s. (a) Yield strength $Y = 2$ GPa, and (b) yield strength $Y = 400$ MPa. Left column: force-displacement curves comparing to analytical solution. Right column: force-time curves comparing to elastoplastic adhesionless contacts.

The material constants for copper are used and shown in Table 5.1. A yield strength of $Y = 2$ GPa requires V_y = 1.27 m/s according to Eq. (5.42). If no adhesion exists, the particle with an initial velocity of $V_0 = 1$ m/s will not produce any plasticity during the contact, i.e. the contact curves of an elastoplastic particle shown Fig. 5.8(a) should be the same as the contact curves of pure elastic particle shown in 5.7(a). However, plasticity has taken place because of adhesion. Comparing the left hand side of Fig. 5.8(a) to that of Fig. 5.7(a), the spikes representing instabilities are more intensive in the presence of plasticity. Both the tensile force and the compressive force are reduced remarkably by plastic deformation. The loading curve deviates from the analytical prediction but still have roughly the same stiffness. The maximum tensile force is between $-\pi R\gamma$ and $-1.5\pi R\gamma$, which is much smaller than any analytical prediction. This result is consistent with the argument by Kogut and Etsion (2003) that the existence of plasticity diminishes the adhesion force. Unloading takes place after the maximum compressive force is reached. The maximum compressive displacement is smaller than that of the corresponding pure elastic particle shown in Fig. 5.7(a). The unloading curve is completely different from the loading curve. It is stiffer than the loading curve and finally oscillates elastically. The area between the loading curve and the unloading curve corresponds to dissipated energy, a large part of which is the plastic deformation energy. Also, the unloading curve is smoother than the loading curve, indicating that the unloading is continuous rather than unstable. Similar to the elastic particle shown in Fig. 5.7(a), the elastoplastic particle shown in Fig. 5.8(a) sticks to the wall. This is represented by the periodical force oscillation shown in the right hand side of Fig. 5.8(a). Comparing to the elastic adhesive contact shown in Fig. 5.7(a), although the tensile force is reduced, the compressive force is reduced even more. The particle is therefore 'stickier' and requires more initial kinetic energy to rebound. This is consistent to the experimental discoveries by Rimai *et al*. (2000). In addition, it can be observed in Fig. 5.8(a) that when the particle is still elongated under the tensile force, the contact law is already different from that in Fig. 5.7(a). This suggests that plastic deformation had already taken place before the particle is compressed. Because the elongation during loading is independent to the initial velocity, it can be stated that plasticity can be initialized by adhesion alone.

Next we study a case of a particle with more realistic yield strength of $Y = 400$ MPa as shown in Fig. 5.8(b). The maximum tensile force and the maximum compressive force are significantly reduced by plasticity. The particle undergoes large plastic deformation at the beginning of the contact process under the tensile force. The more extensive spikes during the loading represent more unstable jumps-to-gain contact area. The stiffness of the loading curve is different from the analytical prediction. The unloading curve descends smoothly and rapidly, leaving a large area between the loading curve and the unloading curve. Due to the low yield strength, the particle undergoes much larger compressive deformation than that in Fig. 5.8(a). More surface energy is therefore released. While the lower yield strength results in more plastic energy dissipation, the particle sticks on the wall at the end of the contact. From the right hand side of Fig. 5.8 it can be seen that the plastic adhesive contact is dissimilar to either plastic adhesionless contact or elastic adhesive contact. Numerical contact law is therefore necessary as no analytical predictions can be used for such complicated cases.

Figure 5.10 shows the surface profiles of the particles at the maximum compression discussed in Fig. 5.8. For the particle of yield strength of $Y = 2$ GPa, the contact area is smaller than the elastic particle with the same specific surface energy. This is because the adhesion force is diminished by the existence of plasticity. The contact area is therefore diminished. For the particle of yield strength $Y = 400$ MPa, the contact area is much larger than the elastic particle. The surface energy released from such a large contact area consumes much more kinetic energy of the particle. The particle is therefore much 'stickier' than that in the elastic contact. For the particle shapes shown in Fig. 5.10, the largest contact area is obtained under the plastic adhesive contact, where the curvature near the contact area is almost negative.

The 'stickier' elastoplastic adhesive contact can be demonstrated clearly by the fact that an elastic adhesive particle rebounds while the corresponding elastoplastic particle does not, as shown in Fig. 5.9(a). For the particle discussed in Fig. 5.9(a), all parameters are the same as those for the particle discussed in 5.7(b) except for the

elastoplasticity. The elastoplastic particle with an initial velocity $V_0 = 25$ m/s and a yield strength $Y = 2$ GPa sticks on the wall after the contact. Compared with the elastic adhesive contact in Fig. 5.7(b), the maximum tensile force during unloading is increased rather than diminished by the plasticity. An interpretation is due to effect of permanent plastic deformation, which makes the curvature near the contact area much larger than that shown in Fig. 5.7(b). Therefore, it is the much larger unloading curvature that increases the adhesion during unloading.

(a) $Y = 2$GPa, $V_0 = 25$ m/s

(b) $Y = 5$GPa, $V_0 = 25$ m/s
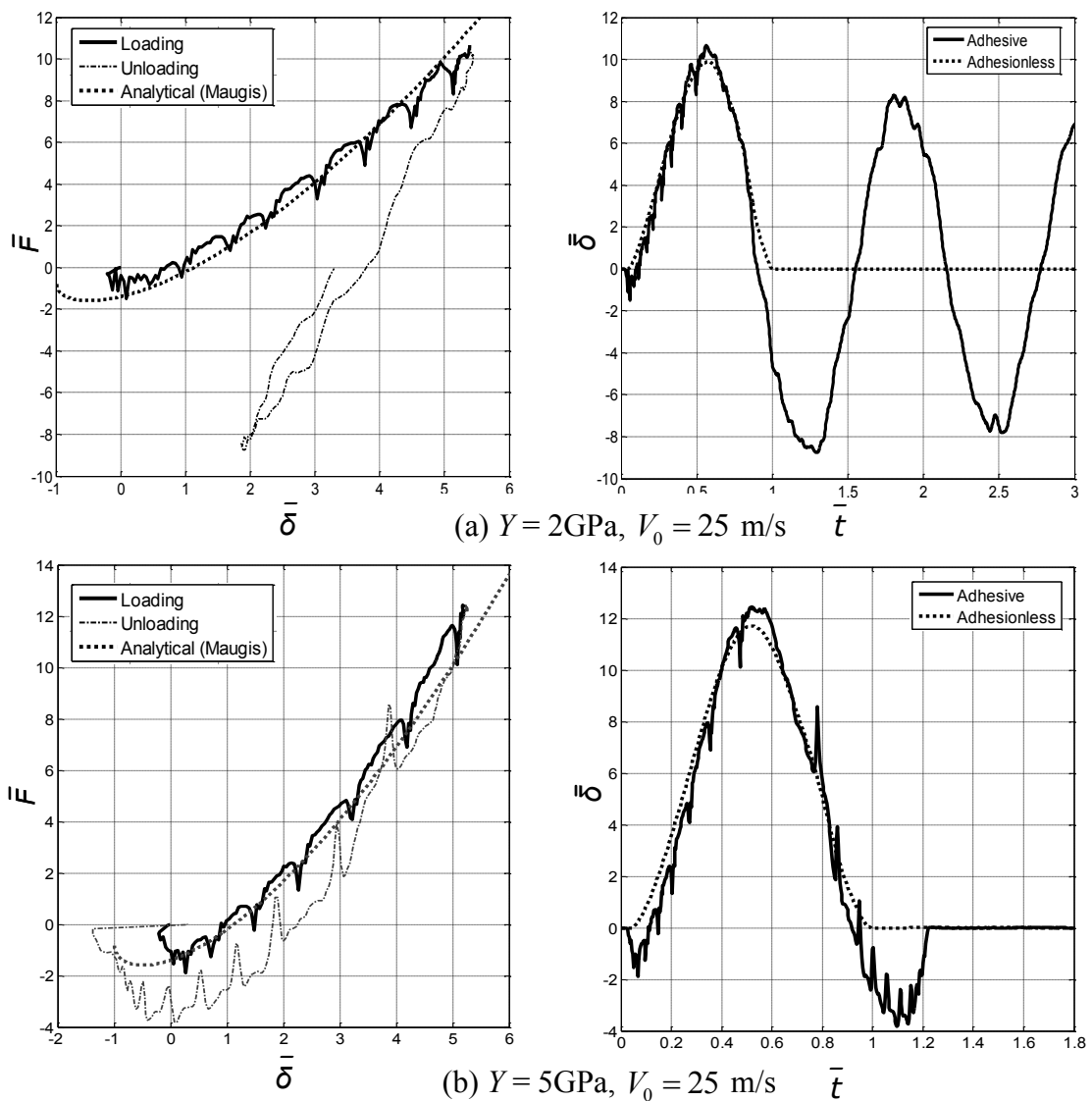
Fig. 5.9 Normalized contact curves for elastoplastic spherical particles of size $R = 50$ nm ($\bar{R} = 630$), realistic specific surface energy $\gamma = 1.17$ J/m^2, and large initial velocity $V_0 = 25$ m/s. (a) Yield strength $Y = 2$ GPa, and (b) yield strength $Y = 5$ GPa. Left column: force-displacement curves comparing to analytical solution. Right column: force-time curves comparing to elastoplastic adhesionless contacts.
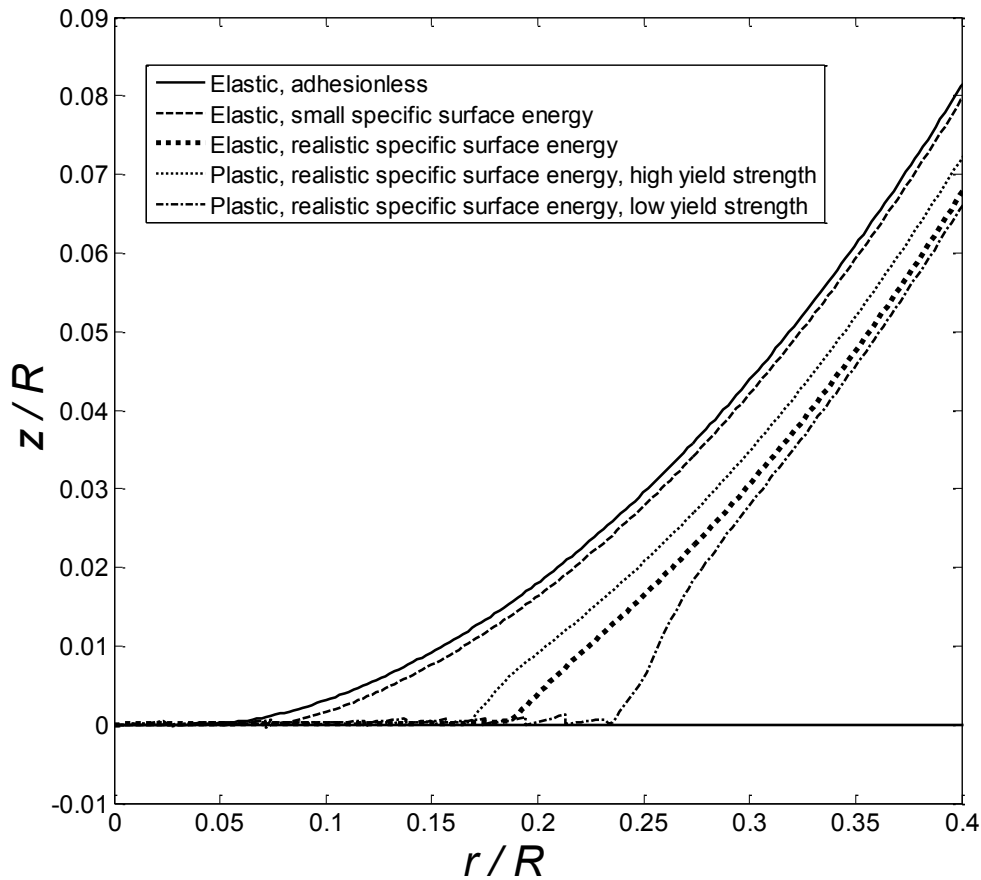
Fig. 5.10 Normalized surface profiles near the contact area, for the adhesive contact of spherical particles. All particles are of radius $R = 50$ nm and initial velocity $V_0 = 1$ m/s. Terms shown in the legend: small specific surface energy: $\gamma = 0.11$ J/m^2, realistic specific surface energy: $\gamma = 1.17$ J/m^2, high yield strength: $Y = 2$ GPa, low yield strength: $Y = 400$ MPa.

A way to reduce sticking is to further increase the yield strength of the elastoplastic particle. As shown in Fig. 5.9(b), if the yield strength is increased to $Y = 5$ GPa, the particle will behaves more elastically and rebounds. The contact curves in Fig. 5.9(b) are rather similar to the particle discussed in Fig. 5.7(b). The effect of plasticity is so minor in the contact shown in Fig. 5.9(b) that elastic deformation dominates over plastic deformation and adhesion. Only small plastic energy dissipation is observed and the particle rebounds with a small permanent plastic deformation. During loading, the maximum tensile force and the maximum compressive force are similar to those in

Fig. 5.7(b). The analytical elastic prediction is also relatively accurate. The maximum tensile force during unloading is increased by the increase in the curvature due to permanent plastic deformation. This larger maximum tensile force during unloading is further evidence that the elastoplastic adhesive contact is 'stickier' than the pure elastic contact.

To summarize, for nano-sized particles plastic deformation is universal. Plastic deformation intensifies the instability during the inbound as the contact area increases but reduces the instability during rebound as the contact area decreases. Plastic deformation reduces both the compressive and tensile forces during loading while either increase or decrease the tensile force during unloading. Plastic deformation diminished the effect of adhesion but requires less compressive force to achieve a large contact area. The deformation of the particle can be therefore either decreased by the diminished adhesive tensile force or increased by the less requirement for the compressive force. The plastic adhesive contact is always 'stickier' than elastic contact due to the energy dissipation during the plastic deformation.

5.4.3 Elastic particles with surface roughness

Particle surface is never atomically smooth. It is therefore questionable to use a contact law derived assuming ideal smooth surface to simulate a real particulate system. In fact, the existence of surface roughness on the surface of a fine particle is ubiquitous and always considered as a key factor in the adhesive contact. Contact between rough surfaces is actually the contact between asperities of the rough surfaces. These asperities are of much smaller sizes than the particle and the effect of adhesion is more significant for each individual asperity. Due to the random nature of the surface roughness, only simple profile of a rough surface is considered in the present research. As suggested by Manners (1998), the profile of the particle can be characterized by periodic sinusoidal waves. The rough surface only occupies a very small part of the particle therefore the particle can still be considered as roughly spherical. The largest distance from the particle centre to the rough surface is set as 50 nm, representing a 50 nm radius for a spherical particle with a characteristic rough

surface. Only elastic particles are considered in the present section. Elastoplastic particles will be studied in the next section.

The contact curves of particles with two different surface roughnesses are plotted in Fig. 5.11. The material constants used here are the same as the smooth elastic particle discussed in Fig. 5.8(a), and the same initial velocity of $V_0 = 1$ m/s is used. Figure 5.11(a) shows the contact curves for a particle with a less rough surface comparing to that shown in Fig. 5.11(b). It can be observed that a rougher surface reduces both the maximum compressive force and the maximum tensile force during the contact. The maximum compressive displacement and maximum elongation are also reduced. The analytical solutions are not shown here because they are significantly different from the numerical results. As shown on the left hand of Fig. 5.11(a), there are several intensive jumps during loading. Each jump is associated with the jump-into contact of one asperity of the surface shown in the middle inset of Fig. 5.11(a). In fact, as shown in Fig. 5.11(a), the behaviour of the contact force can be further complicated by the randomly distributed surface roughness.

Although the effect of adhesion is significant for each individual asperity, the surface roughness makes the particles less 'sticky' globally. This is demonstrated by Fig. 5.11(b). The particle with a rougher surface behaves rather similar to a particle with small specific surface energy shown in Fig. 5.6. The loading curve and unloading curve are indiscernible and the particle can fully rebound after the contact. Only small unstable turnings are observed in the contact curve shown in Fig. 5.11(b). Almost no energy is dissipated. Generally, the universal existence of surface roughness of a fine particle is so important that the contact law may be fundamentally changed. The effect of surface roughness is to reduce the effect of surface energy, in all aspects. However, due to the random nature of surface roughness, it is difficult to predict the dependence of the contact law on surface roughness analytically. A numerical contact law is therefore necessary.
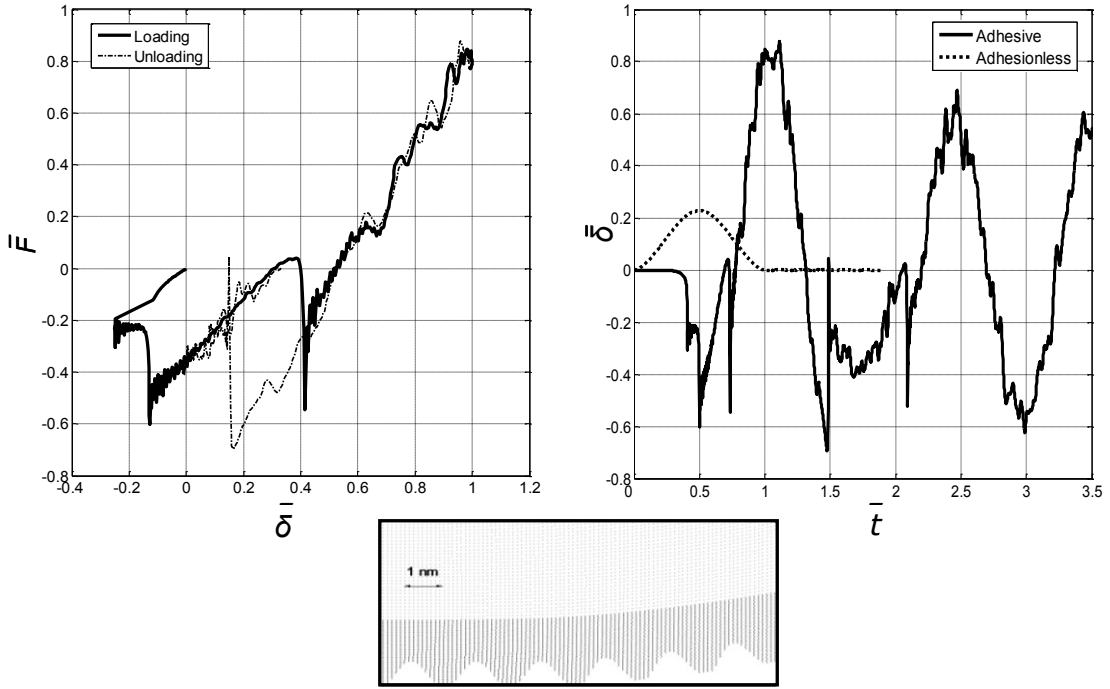
(a) Profile $= -5\cos(120\pi)/12$
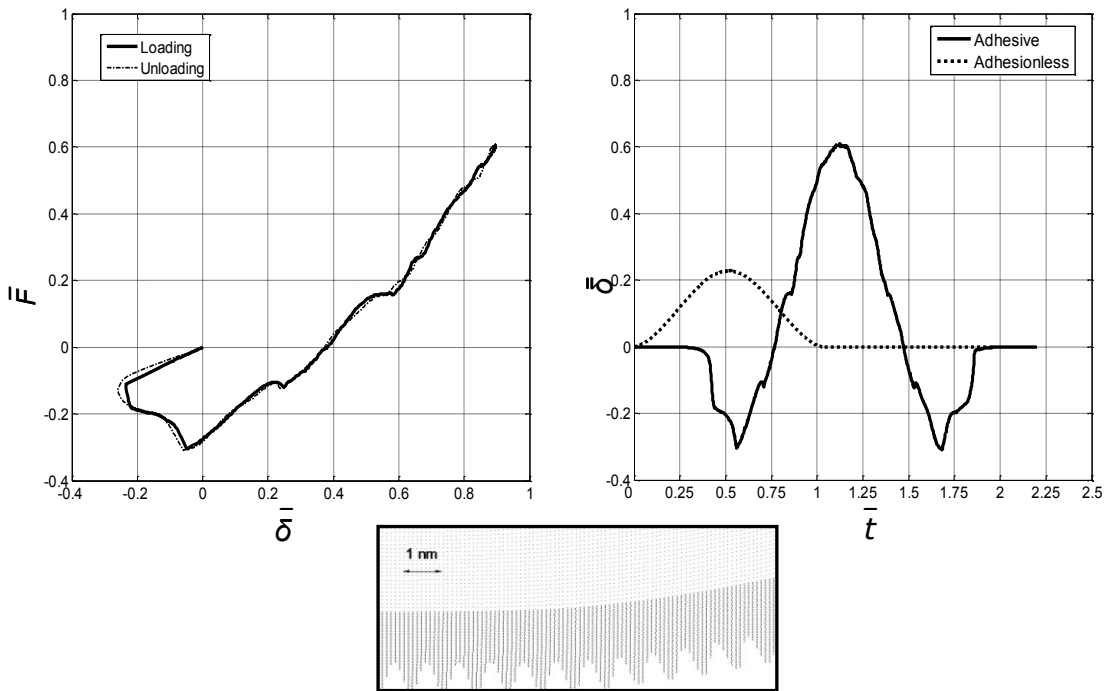
(b) Profile $= -5\cos(240\pi)/12$

Fig. 5.11 Normalized contact curves for elastic particles of size $R = 50\,\text{nm}$ ($\bar{R} = 648$), and specific surface energy $\gamma = 1.17$ J/m^2, with rough surface and small initial velocity $V_0 = 1$ m/s. Profile: (a) $-5\cos(120\pi)/12$, and (b) $-5\cos(240\pi)/12$, where lengths are in the unit of nm. Left column: force-displacement curves. Right column: force-time curves comparing to adhesionless contacts of smooth surface. Middle insets: profiles of the contact areas at the configuration of the maximum compression.

5.4.4 Elastoplastic particles with surface roughness

The above studies have considered all the key factors during particle contact. The effect of adhesion, the interplay between plasticity and adhesion, and the effect of surface roughness have all been investigated separately. This section brings all the three factors together to obtain a more 'realistic' contact law for fine particles. A numerical example of such a 'realistic' contact law is shown in Fig. 5.12. The difference between the particle discussed in Fig. 5.12 and the particle discussed in Fig. 5.11(b) is the yield strength of the former particle is set at a more realistic value of $Y = 400$ MPa. Comparing to the contact law shown in Fig. 5.11(b), the elastic particle which can rebound now sticks to the wall because of plasticity. The existence of plasticity reduces both the tensile force and the compressive force. The maximum displacement is almost the same as the corresponding elastic particle, which means most of the plastic deformation occurs on the asperities of the rough surface. There is little plasticity found in the main body of the particle. The unstable jumps during the loading are significant and difficult to ignore. The maximum tensile force during unloading is much larger than the maximum tensile force during loading. All such complexities make the analytical solutions questionable to use in predicting the interactions between fine particles.

5.5 CONCLUDING REMARKS

The effect of adhesion on contact laws between fine particles is significant. In the present chapter, a new model for the adhesive contact is proposed by incorporating the inter-atomic forces into the Material Point Method. The model is used to study the interplay between surface adhesion, large deformation plasticity and surface roughness during particle contact. The size effect revealed numerically is consistent with the analytical solution for large particles. However the analytical solutions are shown to be less appropriate if the size of particles is small. It is shown that unstable jumps occur frequently during the loading and unloading of the contact. The smooth particles are found to stick especially when plasticity is considered. It is found that

plastic deformation can be initiated by adhesion under zero initial velocity (zero external loading).
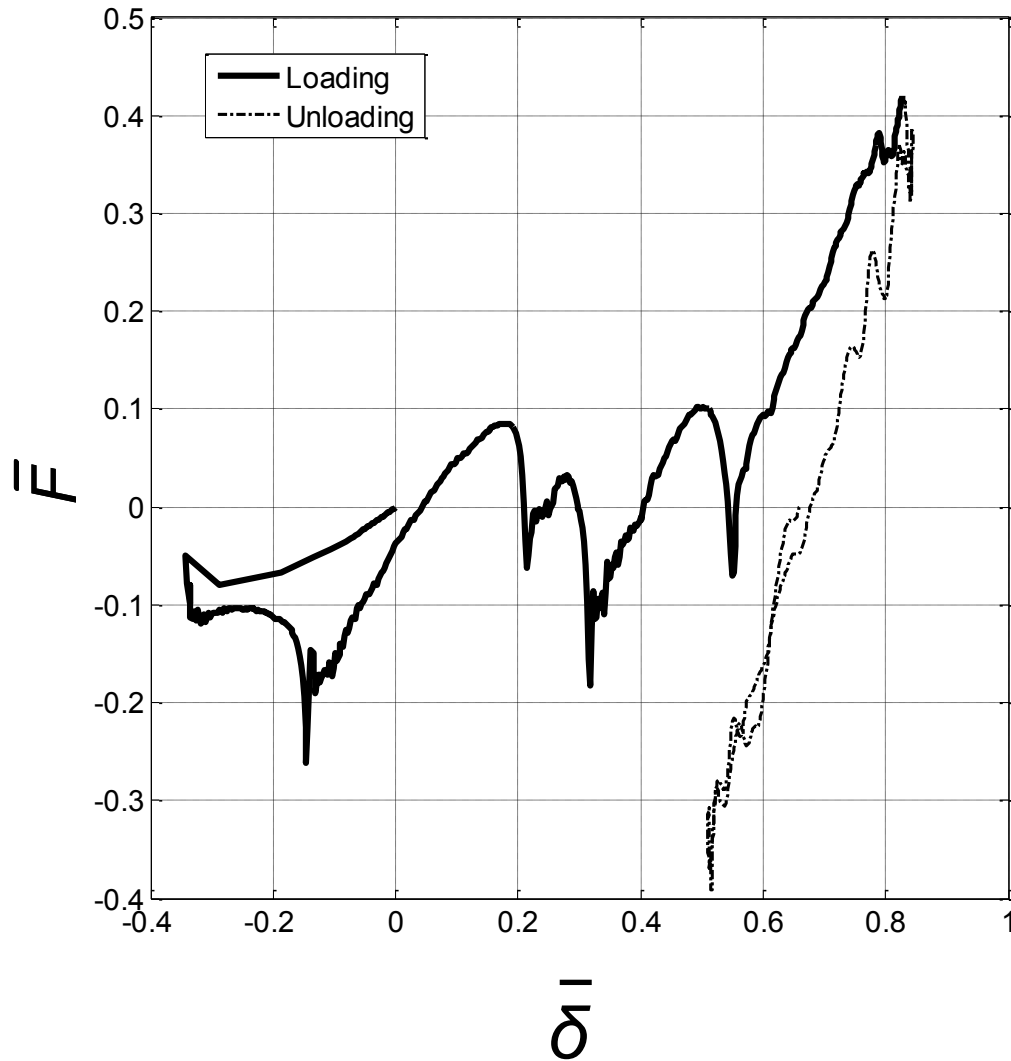
Fig. 5.12 A relatively 'realistic' contact law between fine copper particles with specific surface energy $\gamma = 1.17\,\text{J/m}^2$, yield strength $Y = 400\,\text{MPa}$, and a rough surface with profile $-5\cos(240\pi)/12$ (units in nm).

The existence of surface roughness has a profound effect on the contact law, making analytical solutions far from adequate in realistic problems. It is found that the classical analytical solutions can predict the adhesive contact law only in some ideal

cases. The classical solutions are unable to accurately predict the maximum forces and capture the inability of the unstable jump-to-gain and jump-to-lose contact areas. The assumptions in 'ideal particle' by the analytical solutions are far less appropriate for fine particles than for large particles. The adhesion plays an important role in the contact between fine particles, making the plasticity and the surface roughness key factors. It is shown that the contact law can be completely different from the classical solutions if either plasticity or surface roughness exists. All these leads to that a numerical contact law is highly desirable for fine particles. It has been shown that the present model developed in this study is capable of obtaining numerical contact laws between fine particles. An illustration of what a numerical contact law looks like is given in Fig 5.12.

The numerical results also call for re-examination of some of the classical concepts frequently used when studying contact laws. For example, it is shown that a more DMT like fine particle actually behaves more JKR like. The pull-off force for fine particles depends on the initial velocity rather than only on the specific surface energy and particle size. Sticking is a common phenomenon during the contact between fine particles which has to be considered when simulating the behaviour of a particulate system.

CHAPTER 6

MAIN CONCLUSION OF THE THESIS

The numerical studies presented in this thesis provide a comprehensive understanding on how fine particles interact with each other. The Material Point Method (MPM) is further developed to model particle fragmentation and adhesion. The newly developed numerical technique then enables us to study particle interactions taking into account the effects of particle size, shape, surface roughness, brittleness, adhesion and large deformation. It is shown that these factors have a profound influence on the particle interactions which have been largely ignored previously when studying powder flow or compaction using the discrete element simulations.

It is shown that the MPM has two major advantages over the conventional finite element method:

1. The MPM requires neither remeshing nor iterative contact algorithms when solving problems involving (a) contact boundary conditions, (b) large deformation, and (c) multi-cracking;
2. The inter-atomic forces can be easily incorporated into the scheme so that the continuum model can have an atomistic input.

Throughout this thesis, the Material Point Method is validated using analytical solutions when it is applied to a new class of problems. The reliability of the method is therefore solidly demonstrated and the numerical results are of high confidence. An appealing feature of the MPM is its robustness and simplicity. The computer programme seldom crashes due to numerical problems and the computer implementation of the MPM is relatively simple because the method does not require remeshing or iterative schemes. The requirement on computational resource is also

reasonable. All these advantages make the method a powerful tool in solving problems far beyond the scope of particle contact studied here.

The focus of this thesis is, however, on the contact laws between a pair of particles in the context of the Discrete Element simulations. CHAPTER 3 presents studies on relatively large particles, for which mechanical response dominates the contact law. It is shown that an analytical framework is possible for the elastoplastic contact law if the particle is spherical and elastic perfectly plastic. It is also shown that such contact laws are sensitive to the impact velocity, details of material properties, as well as the shapes of the particles. The applicability of the analytical contact laws is therefore limited.

In CHAPTER 5 the inter-atomic forces are incorporated into the Material Point Method in order to study contact laws for nano-sized particles. The effect of surface energy is important for such contact laws (referred to as adhesive contact laws). The validity of the existing analytical solutions is examined. It is shown that the adhesive contact laws are complicated by the particle size, surface roughness, and plasticity, which show a sophisticated interplay. The analytical solutions are based on over-simplistic assumptions and invalid for most practical circumstances. Some new understandings on behaviour of nano-particles are also revealed.

Brittle failure is another important phenomenon during the impact between particles, which is studied in CHAPTER 4. Weibull's theory is incorporated into the MPM. It is shown that such a MPM scheme can conveniently simulate the initiation and propagation of multi-cracks during the brittle failure of particles. The experimentally observed failure patterns and threshold velocities are reproduced by the MPM simulations.

There are certainly some aspects of the work that can be improved immediately if extra time is available to the project. For examples, all the current models assume either plane stress or axisymmetric conditions while a full 3 dimensional model is

desirable for particles of irregular shape; the tangent contact law has been ignored in the current study; for nano-particles the plasticity theory for limited slide planes should be used.

Contact laws between fine particles are the vital input to discrete element simulations. At present, most DEM simulations are still using the over-simplest analytical contact laws, such as the Hertz contact law (e. g. Johnson, 1985) for adhesionless particles and the JKR theory (Johnson *et al*., 1971) for adhesive contact laws. The DEM can readily use numerical contact laws as its input. The reliability and the robustness of the MPM make it a routine task to obtain the contact laws numerically. The studies presented in this thesis have laid a solid foundation for further research on incorporating the Material Point Method directly into the discrete element simulations for a wide range of applications in material and chemical processing.

Part of the work was presented at the 9th U.S. National Congress on Computational Mechanics, San Francisco, USA. The following papers have been accepted or submitted:

- The contact law between solid particles, accepted by Journal of the Mechanics and Physics of Solids.

- The impact induced brittle failure, submitted to International Journal of Solids and Structures.

Details, other conference presentations and Journal papers related to this work are listed in APPENDICES.

REFERENCES

Adams M. J., Lawrence C. J., Urso M. E. D., and Rance J., 2004. Modelling collisions of soft agglomerates at the continuum length scale. Powder Technology. Vol. 140. 268-279.

Andrews E. W., and Kim K. S., 1998. Threshold conditions for dynamic fragmentation of ceramic particles. Mechanics of Materials. Vol. 29. 161-180.

Attard P., and Parker J. L., 1992. Deformation and adhesion of elastic bodies in contact. Physical Review A. Vol. 46. 7959-7971.

Arbiter, N., Harris, C. C., and Stamboltzis G. A., 1969. Single fracture of brittle spheres. Transactions of the AIME. Vol. 244. 118-133.

Argento C., Jagota A., and Carter W. C., 1997. Surface formulation for molecular interactions of macroscopic bodies. Journal of the Mechanics and Physics of Solids. Vol. 45. 1161-83

Ashby M. F., and H Jones D. R., 1986. Engineering Materials 2. PERGAMON Press Chapter 15-18.

Bardenhagen S. G., and Brackbill J. U., 1998. Dynamic stress bridging in granular material. Journal of Applied Physics. Vol. 83. 5732-5740.

Bardenhagen S. G., and Brackbillb J. U., 2000. The material-point method for granular materials. Computer Methods in Applied Mechanics and Engineering. Vol. 187. 529-541.

Bardenhagen S. G., Brackbill J. U., and Sulsky D., 2000. Numerical study of stress distribution in sheared granular material in two dimensions. Physical Review E. Vol. 62. 3882-3890.

Barthel E., 1997. On the description of the adhesive contact of spheres with arbitrary interaction potentials. Journal Colloid and Interface Science. Vol. 200. 7-18.

Batra R. C., and Lear M. H., 2004. Simulation of brittle and ductile fracture in an impact loaded prenotched plate. International Journal of Fracture. Vol. 126. 179-203.

Behera B., Kun F., McNamara S., and Herrmann H. J., 2005. Fragmentation of a circular disc by impact on a frictionless plate. Journal of Physics: Condensed Matter. Vol. 17. S2439-S2456.

Belytschko T., Liu W. K., 1985. Computer methods for transient fluid-structure analysis of nuclear reactors. Nuclear Safety. Vol. 26. 14-31.

Belytschko T., Liu W. K., and Moran B., 2000. Nonlinear Finite Elements for Continua and Structures. WILEY.

Bradley R. S., 1932. The cohesive energy between solid surfaces and the surface energy of solids. Philosophical Magazine. Vol. 13. 853-862.

Burgess D., Sulsky D., and Brackbill J. U., 1992. Mass matrix formulation of the FLIP particle-in-cell method. Journal of Computational Physics. Vol. 103. 1-15.

Camacho G. T., and Ortiz M., 1996. Computational modelling of impact damage in brittle materials. International Journal of Solids and Structures. Vol. 33. 2899-2938.

Chaudhri M. M., Hutchings I. M., and Makin P. L., 1984. Plastic compression of spheres. Philosophical Magazine A: Physics of Condensed Matter, Defects and Mechanical Properties. Vol. 49. 493-503.

Cheong Y. S., Salman A. D., and Hounslow M. J., 2003. Effect of impact angle and velocity on the fragment size distribution of glass spheres. Powder Technology. Vol. 138. 189-200.

Cheong Y. S., Reynolds G. K., Salman A. D., and Hounslow M. J., 2004. Modelling fragment size distribution using two-parameter Weibull equation. International Journal of Mineral Processing. Vol. 74. S227-S237.

Cundall P. A., 1971. A computer model for simulating progressive large scale movements in blocky rock systems. Proceedings of the ISRM symposium, Nancy, France. Vol. 2. 129-136.

Derjaguin B. V., Muller V. M., and Toporov Y. P., 1975. Journal of Colloid and Interface Science. Vol. 53. 314-326.

Erkoc S., 1993. An empirical many-body potential energy function constructed from pair-interactions. Zeitschrift fur Physik D: Atoms Molecules and Clusters. Vol. 32. 257-260.

Erkoc S., 1997. Empirical many-body potential energy functions used in computer simulations of condensed matter properties. Physics Reports. Vol. 278. 79-105.

Espinosa H. D., Zvattieri P. D., and Dwivedi S. K., 1998. A finite deformation continuum/discrete model for the description of fragmentation and damage in brittle materials. Journal of the Mechanics and Physics of Solids. Vol. 46. 1909-1942.

Feng, J. Q., 2000. Contact behaviour of spherical elastic particles: a computational study of particle adhesion and deformations. Colloid and Surfaces A: Physicochemical and Engineering aspects. Vol. 172. No. 175-198.

Foiles S. M., Baskes M. I., and Daw M.S., 1986. Embedded-atom-method functions for the fcc metals Cu, Ag, Au, Ni, Pd, Pt, and their alloys. Physical Review B. Vol. 33. 7983-7991.

German R. M., 2003. Strength Evolution in Debinding and Sintering, Proceedings Sintering 2003.

Greenwood J. A., 1997. Adhesion of elastic spheres. Proceedings: Mathematical, Physical and Engineering Sciences. Vol. 453. 1277-1297.

Greenwood J. A., and Johnson K. L., 1998. An alternative to the Maugis model of adhesion between elastic spheres. Journal of Physics D: Applied Physics. Vol. 31. 3279-3290.

Gu J., and Li L., 2008. Adhesive contacts of a rigid sphere and an elastic-perfectly plastic half-space. Submitted to Philosophical Magazine & Philosophical Magazine Letters.

Guo T., 1995. Brittle-damage analysis of cracks under conditions of plane-strain tensile loading. Acta Mechanica Solida Sinica. Vol. 16. 132-139.

Harlow F. H., 1964. The particle-in-cell computing method for fluid dynamics, in Adler B., Fernbach S., and Rotenberg M., Methods for Computational Physics. Vol. 3. Academic Press, New York, 319-343.

Hettich T., and Ramm E., 2006. Interface material failure modelled by the extended finite-element method and level sets. Computer Methods in Applied Mechanics and Engineering. Vol. 195. 4753-4767.

Hoomans B. P. B., 2000. Granular dynamics of gas-solids two phase flows. Ph.D. Thesis. Universiteit Twente.

Hughes T. J. R., Taylor R. L., and Sackman J. L., 1974. Finite element formulation and solution of contact-impact problems in continuum mechanics. SESM Report. No. 74-78.

Hughes T. J. R., Taylor R. L., Sackman J. L., Curnier A., and Kanoknukulchai W., 1976. A finite element method for a class of contact-impact problems. Computer technique in Applied Mech. and Engineering (CMAME). Vol. 8. 249-276.

Hunter S. C., 1957. Energy absorbed by waves during impact. Journal of the Mechanics and Physics of Solids. Vol. 8. 162-171.

Hutchings I. M., 1979. Energy absorbed by elastic waves during plastic impact. Journal of Physics D: Applied Physics. Vol. 12. 1819-1824.

Johnson K. L., 1985. Contact Mechanics. Cambridge: Cambridge University Press.

Johnson K. L., and Greenwoord J. A., 1997. An adhesion map for the contact of elastic spheres. Journal of Colloid and Interface Science. Vol. 192, 326-333.
Johnson K. L., Kendall K., and Roberts A. D., 1971. Surface energy and the contact of elastic solids. Proceedings of the royal society of London. Series A, Mathematical and Physical Sciences. Vol. 324. 301-313.

Kadono T., and Arakawa M., 2002. Crack propagation in thin glass plates caused by high velocity impact. Physical Review E. Vol. 65. 035107/1-4.

Kendall K., 2001, Molecular Adhesion and Its Applications - The Sticky Universe, The University of Birmingham, Kluwer Academic, Birmingham, England.

Kendall K., Yong C. W., and Smith W., 2004. Particle adhesion at the nanoscale. The Journal of Adhesion. Vol. 80. 21-36.

Kogut L, and Etsion I., 2003. Adhesion in elastic–plastic spherical microcontact Journal of Colloid and Interface Science. Vol. 261. 372-378.

Kohlhoff S., Gumbsch P., and Fischmeister H., 1991. Crack propagation in BCC crystals studied with a combined finite-element and atomistic model. Philosophical Magazine A: Physics of Condensed Matter, Defects and Mechanical Properties. Vol. 64. 851-78.

Li F., Pan J., and Sinka C. 2008. The interaction of solid particles. Accepted by Journal of the Mechanics and Physics of Solids.

Li F., Pan J., and Sinka, C., 2008. Modelling Impact induced Brittle Failure Using the Material Point Method. Submitted to: International Journal of Solid and Structures.

Li L-Y, Thornton C., and Wu C-Y., 2000. Impact behaviour of elastoplastic spheres with a rigid wall. Proceedings of the Institution of Mechanical Engineers, Part C: Journal of Mechanical Engineering Science. Vol. 214. 1107-1114.

Li L-Y, Wu C-Y, and Thornton C., 2002. A theoretical model for the contact of elastoplastic bodies. Proceedings of the Institution of Mechanical Engineers, Part C: Journal of Mechanical Engineering Science. Vol. 216. 421-31

Liu W. K., Change H., and Belytschko T., 1988. Arbitrary Lagrangian and Eulerian Petrov-Galerkin finite elements for nonlinear continua. Computer Methods in Applied Mechanics and Engineering. Vol. 68. 259-310.

LU H., Daphalapurkar N. P., Wang B., Roy S., and Komanduri R., 2006. Multiscale simulation from atomistic to continuum - coupling molecular dynamics (MD) with the material point method (MPM). Philosophical Magazine. Vol. 86. 2971-2994.

Mahato A., Sachdev A. K., and Biswas S. K., 2007. Effect of particle morphology on resistance to permanent sinking by normal loading of silicon particle in aluminium matrix of a cast aluminium silicon alloy. Wear. Vol. 265. 849-855.

Mangwandi C., Cheong Y. S., Adams M. J., Hounslow M. J., and Salman A. D., 2007. The coefficient of restitution of different representative types of granules. Chemical Engineering Science. Vol. 62. 437-450.

Manners W., 1998. Partial contact between elastic surfaces with periodic profiles. Proceedings of the Royal Society of London, Series A: Mathematical and Physical Sciences. Vol. 454. 3203-3221.

Maugis, D. J., 1992. Journal of Colloid and Interface Science. Vol. 150. 243-269.

Mesarovic S. D., and Fleck N. A., 2000. Frictionless indentation of dissimilar elastic-plastic spheres. International Journal of Solid and Structures. Vol. 37. 7071-7091.

Moreno. R., Ghadiri. M., and Anton S. J., 2003. Effect of the impact angle on the breakage of agglomerates: a numerical study using DEM. Powder Technology. Vol. 130. 132-137.

Needleman A., and Tvergaard V., 1987. An analysis of ductile rupture modes at a crack tip. Journal of the Mechanics and Physics of Solids. Vol. 35. 151-183.

Ochoa, J. G. D., Binder K., and Paul W., 2006. Molecular dynamics simulations of the embedding of a nano-particle into a polymer film. Journal of Physics: Condensed Matter. Vol. 18. 2777-2787.

Parker J. L., and Attard P., 1992. Deformation of surfaces due to surface forces. Journal of Physical Chemistry. Vol. 96. 10398-10403.

Sahoo P., and Banerjee A., 2005. Asperity interaction in adhesive contact of metallic rough surfaces. Journal of Physics. D: Applied Physics. Vol.28. 4096-4103.

Potapov A. V., and Campbell C. S., 1994. Computer simulation of impact-induced particle breakage. Powder Technology. Vol.81. 207-216.

Potapov A. V., and Campbell C. S., 1997. The two mechanisms of particle impact breakage and the velocity effect. Powder Technology. Vol.93. 13-21.

Potapov A. V., and Campbell C. S., 2001. Parametric dependence of particle breakage mechanisms. Powder Technology. Vol. 120. 164-174.

Rajiv A., Ashok K., and Narendra D., 2006. Materials Processing and Manufacturing Science. Butterworth-Heinemann, Chapter: 3.

Rapaport D. C., 1995. The art of molecular dynamics simulation. Cambridge University Press. Chapter 1-3.

Rimai D. S., Quesnel D. J., and Busnaina A. A., 2000. The adhesion of dry particles in the nanometer to micrometer-size range. Colloid and Surfaces A: Physicochemical and Engineering aspects. Vol. 165. 3-10.

Salman, A. D., and Gorham, D. A., 2000. The fracture of glass spheres. Powder Technology. Vol. 107. 179-185.

Schwarz U. D., 2003. A generalized analytical model for the elastic deformation of an adhesive contact between a sphere and a flat surface. Journal of Colloid Interface and Science. Vol. 261. 99-106.

Shipway P.H., and Hutchings I. M., 1993. Fracture of brittle spheres under compression and impact loading: I. Elastic stress distribution. Philosophical Magazine A: Physics of Condensed Matter, Defects and Mechanical Properties. Vol. 67. 1389-1404.

Sitharam T. G., 2000. Numerical Simulation of Particulate Materials Using Discrete Element Modeling. Current science. Vol. 78. 876-886.

Smith R. W., and Srolovitz D. J., 1994. Simulation of dynamic fracture of an impact-loaded brittle solid. Modelling and Simulation in Materials Science and Engineering. Vol. 2. 1153-1170.

Smith R. W., and Srolovitz D. J., 1995. Simulation of dynamic fracture of an impact-loaded brittle solid: microcracked and polycrystalline solids. Modelling and Simulation in Materials Science and Engineering. Vol. 3. 665-588.

Storakers, B., 1997. Local contact behaviour of viscoplastic particles. Proceedings of the IUTAM Symposium on Mechanics of Granular Flow and Powder Compaction, Kluwer Academic Publishers, Amsterdam, The Netherlands (1997).

Sulsky D., and Schreyer H. L., 2004. MPM simulation of dynamic material failure with a decohesion constitutive model. European Journal of Mechanics A/Solids. Vol. 23. 423-445.

Sulsky, D., Chen Z., and Schreyer H. L., 1994. A particle method for history-dependent materials, Computational Methods in Applied Mechanics and Engineering. Vol. 118. 179-196.

Sulsky D., Zhou S., and Schreyer H. L., 1995. Application of a particle-in-cell method to solid mechanics. Computer Physics Communications. Vol. 87. 236-252.

Sulsky D., and Schreyer H. L., 1996. Axisymmetric form of the material point method with applications to upsetting and Taylor impact problems. Computer Methods in Applied Mechanics and Engineering. Vol. 139. 409-429.

Sulsky D., and Schreyer H. L., 2004. MPM simulation of dynamic material failure with a decohesion constitutive model. European Journal of Mechanics A/Solids. Vol. 23. 423-445.

Tabor D. 1977. Surface forces and surface interactions. Journal of Colloid and Interface Science. Vol. 58. 2-13.

Thornton C., 1997. Coefficient of restitution for collinear collisions of elastic-perfectly plastic spheres. Transactions of the ASME. Journal of Applied Mechanics. Vol. 64. 383-386.

Thornton C., Yin K. K., and Adams M. J., 1996. Numerical simulation of the impact fracture and fragmentation of agglomerates. Journal of Physics D: Applied Physics. Vol. 29. 424-435.

Timothy S. P., Pearspm J. M., and Hutchings I. M., 1987. The contact pressure distribution during plastic compression of lead spheres. International Journal of Mechanical Sciences. Vol. 29. 713-719.

Tvergaard V., 1982. Influence of void nucleation on ductile shear fracture at a free surface. Journal of the Mechanics and Physics of Solids. Vol. 34. 399-425.

Vu-Quoc L., and Zhang X., 1999. An elastoplastic contact force-displacement model in the normal direction: displacement-driven version. Proceedings of the Royal Society of London, Series A: Mathematical, Physical and Engineering Sciences. Vol. 455. 4013-4039.

Wagner, N. J., Holian B. L., and Voter A. F., 1992. Molecular-dynamics simulation of two-dimensional materials at high strain rates. Physical Review A. Vol. 45. 8457-8470.

Wiezckowski Z., Youn S., and Yeon J., 1999. A particle-in-cell solution to the silo discharging problem. International Journal for Numerical Methods in Engineering. Vol. 45. 1203-1225.

Wiezckowski Z., 2004. The material point method in large strain engineering problems Computational Methods in Applied Mechanics and Engineering. Vol. 193. 4417-4438.

Wu C-Y., Li L-Y., and Thornton C., 2003. Rebound behaviour of spheres for plastic impacts. International Journal of Impact Engineering. Vol. 28. 929-946.

Wu C-Y., Li L-Y., and Thornton C., 2005. Energy dissipation during normal impact of elastic and elastic-plastic spheres. International Journal of Impact Engineering. Vol. 32. 503-604.

Wu S. Z, Chau K. T., and Yu T. X., 2004. Crushing and fragmentation of brittle spheres under double impact test. Powder Technology. Vol. 143-144. 41-55.

Xu X., and Needleman A., 1994. Numerical simulations of fast crack growth in brittle solids. Journal of the Mechanics and Physics of Solids. Vol. 42. 1397-1434.

APPENDICES

PUBLICATIONS

Fan Li, Jingzhe Pan, Csaba Sinka, 2008. The interaction of solid particles. Accepted by Journal of the Mechanics and Phyics of Solid, subjected to minor revisions.

Fan Li, Jingzhe Pan, Csaba Sinka, 2008. Modeling Impact Induced Brittle Failure Using the Material Point Method. Submitted to International Jounal of Solid and Structures.

Fan Li, Jingzhe Pan, Csaba Sinka, 2008. Adhesive contact laws between fine particles, 1st draft, to be submitted to Physics Review.

CONFERENCE PRESENTATIONS

Fan Li, *et al*., 2008. Modelling brittle cracking in particle impact. One day meeting on cracking in powder compacts. University of Leicester, 24, Jun. 2008.

Fan Li, *et al*., 2008. Contact laws of solid particles during impact. Workshop on mechanics of materials, run by the Oxford and Leicester group. University of Leicester, 06, Feb. 2008.

Fan Li, *et al*., 2007. Modelling brittle fracture using material point method. The 9th U.S. National Congress on Computational Mechanics, 23-26, Jul. 2007, San Francisco, USA.

APPENDIX I

Reynold's theorem of material time derivative

Define a material deformation gradient that

$$\tilde{\mathbf{F}} = \frac{\partial \mathbf{u}(\mathbf{x},t)}{\partial \mathbf{x}} = \frac{\partial u_i}{\partial x_j} \tag{A1.1}$$

where $\mathbf{u}$ is the displacement, $\mathbf{x}$ is the coordinate system. The determinant of the deformation gradient is

$$J = \det(\tilde{\mathbf{F}}). \tag{A1.2}$$

Equation (A.12) can be used to link the current deformation with the initial configuration that

$$\int_{\Omega} f(\mathbf{x},t) d\Omega = \int_{\Omega_0} f(\mathbf{x},t) J d\Omega_0 \tag{A1.3}$$

in which f is an arbitrary function, Ω is the deformed material domain and Ω_0 is the initial material domain. The time derivative of Eq. (A1.2) gives

$$\frac{dJ}{dt} = J \frac{\partial v_i}{\partial x_i} = J \nabla \cdot (\mathbf{v}) \tag{A1.4}$$

where $\mathbf{v}$ is the velocity vector and Einstein summation is used. Now apply the material time derivative on the current deformed configuration (Eq. (A1.3)) such that

$$\frac{d}{dt} \int_{\Omega} f(\mathbf{x},t) d\Omega = \frac{d}{dt} \int_{\Omega_0} f(\mathbf{x},t) J d\Omega_0. \tag{A1.5}$$

Because the initial configuration is time independent, Eq. (A1.5) implies

$$\frac{d}{dt} \int_{\Omega_0} f(\mathbf{x},t) J d\Omega_0 = \int_{\Omega_0} \frac{d(f(\mathbf{x},t)J)}{\partial t} d\Omega_0 = \int_{\Omega_0} \left[\frac{df(\mathbf{x},t)}{dt} J + \frac{dJ}{dt} f(\mathbf{x},t) \right] d\Omega_0$$

$$= \int_{\Omega_0} \left[\frac{df(\mathbf{x},t)}{dt} J + div(\mathbf{v}) J f(\mathbf{x},t) \right] d\Omega_0 = \int_{\Omega_0} J \left[\frac{df(\mathbf{x},t)}{dt} + div(\mathbf{v}) f(\mathbf{x},t) \right] d\Omega_0$$

$$= \int_{\Omega} \left[\frac{df(\mathbf{x},t)}{dt} + div(\mathbf{v}) f(\mathbf{x},t) \right] d\Omega. \tag{A1.6}$$

APPENDIX II

Flow char of Material Point Method
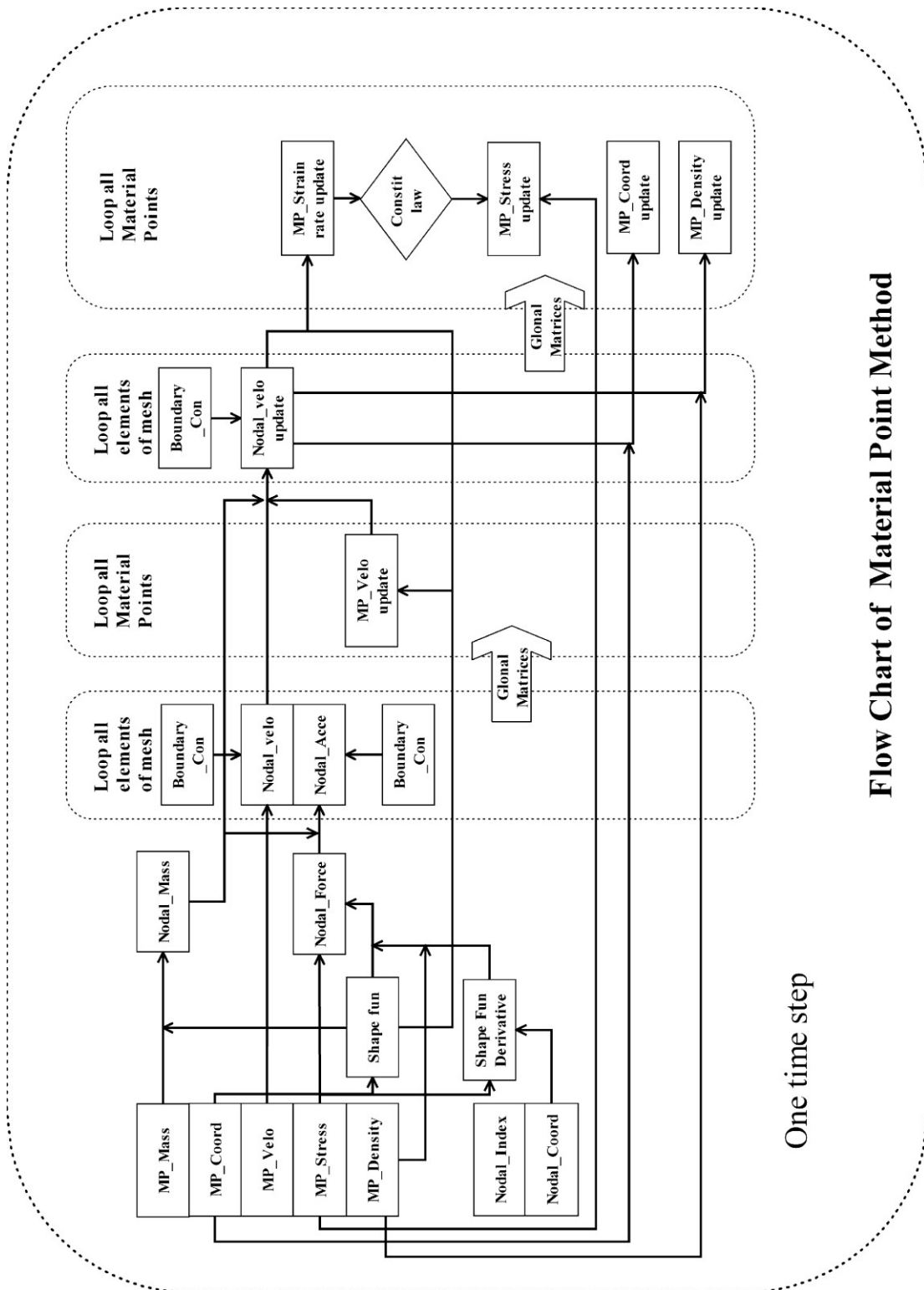
Flow Chart of Material Point Method

APPENDIX III

Radial return mapping Algorithm

Within one time step, define the index of return mapping step k, the effective strain $\tilde{\varepsilon}$, the plasticity parameter $\Delta\lambda$, the increment of the plasticity parameter $\delta\lambda$, the function of yield surface $\overline{f}$. The radial return mapping algorithm is described below.

1. Initialization

$$k = 0, \ \tilde{\varepsilon}^{(0)} = \tilde{\varepsilon}^{t}, \ \Delta\lambda^{(0)} = 0, \ \boldsymbol{\sigma}^{(0)} = (\boldsymbol{\sigma}^{t+\Delta t})^{(0)} \tag{A3.1}$$

where $\tilde{\varepsilon}^{t}$ is the effective strain at the present time step.

2. Calculate the function of yield surface

$$\overline{f}^{(k)} = \overline{\sigma}^{(k)} - \tilde{\sigma}(\tilde{\varepsilon}^{(k)}) = (\overline{\sigma}^{(0)} - 3\mu\Delta\lambda^{(k)}) - \tilde{\sigma}(\tilde{\varepsilon}^{(k)}) \tag{A3.2}$$

where $\overline{\sigma}^{(0)}$ is the uniaxial effective stress calculated from $\boldsymbol{\sigma}^{(0)}$, $\tilde{\sigma}$ is the uniaxial effective stress calculated from $\tilde{\sigma} = Y + H\tilde{\varepsilon}$. H is the hardening modulus, μ is shear modulus and given by

$$\mu = \frac{E}{2(1+\upsilon)}, \tag{A3.3}$$

where E is the unixial elastic modulus and υ is the Poisson's ratio.

If: $\overline{f}^{(k)} < TOL_1$ then converged, where TOL_1 is a small number.
Else, go to step 3.

3. Compute increment in plasticity parameter

$$\delta\lambda^{(k)} = \frac{(\bar{\sigma}^{(0)} - 3\mu\Delta\lambda^{(k)}) - \tilde{\sigma}(\tilde{\varepsilon}^{(k)})}{3\mu + H} \tag{A3.4}$$

4. Update plastic strain and internal variables

$$\boldsymbol{\sigma}^{(k+1)} = \boldsymbol{\sigma}^k - 2\mu\delta\lambda^{(k)}\sqrt{\frac{3}{2}}\hat{\mathbf{n}} \tag{A3.5}$$

$$\tilde{\varepsilon}^{(k+1)} = \tilde{\varepsilon}^{(k)} + \delta\lambda^{(k)} \tag{A3.6}$$

$$\Delta\lambda^{(k+1)} = \Delta\lambda^{(k)} + \delta\lambda^{(k)} \tag{A3.7}$$

$$k = k + 1 \tag{A3.8}$$

Go to step 2.

After the condition of convergence in step 2 is met, the stress tensor $\boldsymbol{\sigma}^{(k+1)}$ is the correctly updated stress tensor $\boldsymbol{\sigma}^{t+\Delta t}$.

Remark: Eq. (3.16) is the matrix exponent and is difficult to calculate. However, for the axisymmtric formula, the problem is much simplified since there is only one rotation axis and the skew-symmetric matrix $\mathbf{W}$ has the form of

$$\begin{bmatrix} 0 & w \\ -w & 0 \end{bmatrix}, \tag{A3.9}$$

and $\mathbf{Q}$ is therefore calculated to be orthogonal that

$$\begin{bmatrix} \cos(w\Delta t) & \sin(w\Delta t) \\ -\sin(w\Delta t) & \cos(w\Delta t) \end{bmatrix}. \tag{A3.10}$$

APPENDIX IV

*The decisions of the failure pattern under different levels of mesh status.*

level 1
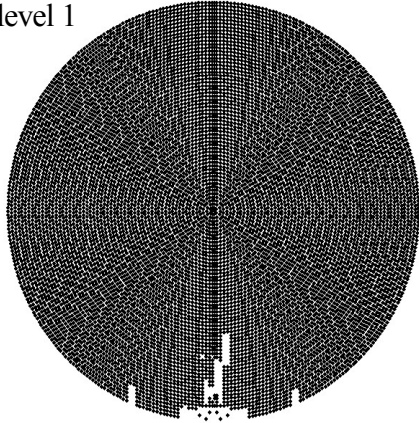
level 2
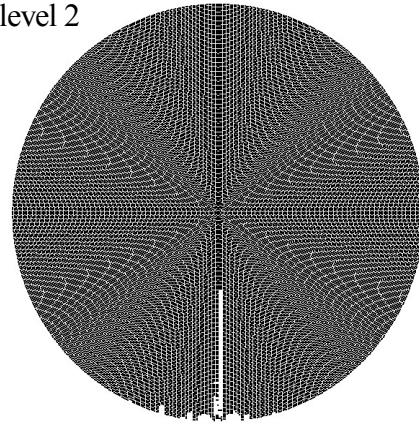
level 3
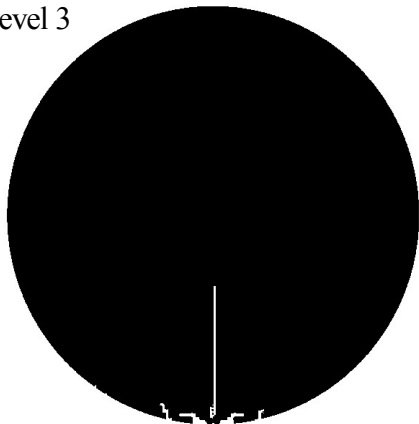
level 4
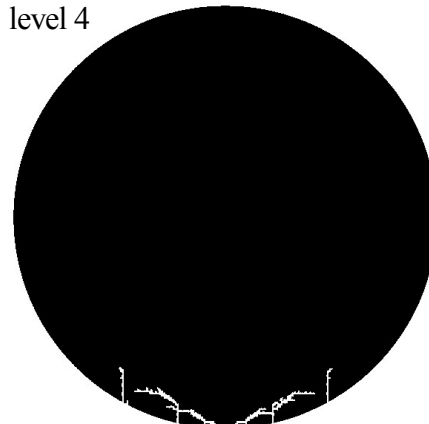
level 5
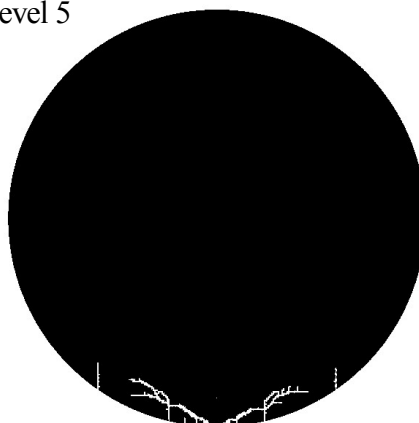
level 6
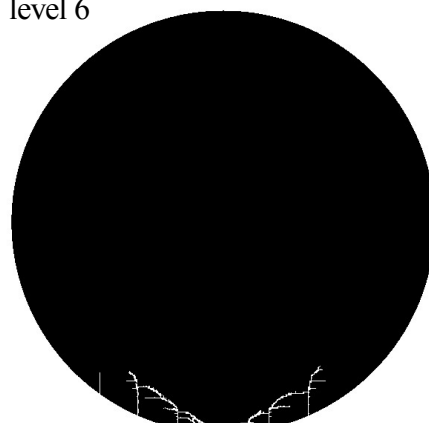
The failure pattern at a time instance during the impact of a circular disc on a rigid wall, for difference levels of mesh status in Table. 4.1. The simple failure patterns are found at the same time, 0.602 μs after the initial contact between the particle and the wall, while before the particle starts to rebound and the complicated failure patterns are formed.

APPENDIX V

The deriving of Eq. (5.31) and Eq. (5.32)

Starting from the inter-atomic potential of the power-law form that

$$U_{L-J}(s) = 4\tilde{e}\left[\left(\frac{\varepsilon_0}{s}\right)^{12} - \left(\frac{\varepsilon_0}{s}\right)^{6}\right]. \tag{A5.1}$$

Consider two planar infinite surfaces as shown in a 2D formula in the figure below, when surface 1 ($S1$) is approaching surface 2 ($S2$).
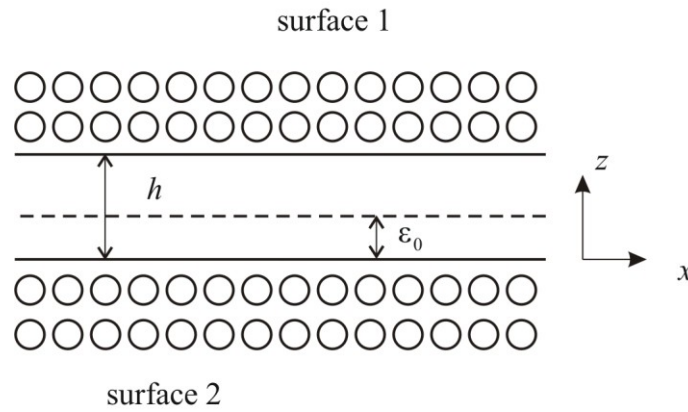
For one atom on surface 2, the inter-atomic potential created by surface 1 is the volume integration of the pairs consisted of the atom in surface 2 and every atom in surface 1 that

$$u(s) = \rho_1 \int_{S1} U_{L-J}(s)dS1 \tag{A5.2}$$

where ρ_1 is the number of atoms in the domain $S1$ per unit volume. By using the formula

$$s = \sqrt{x^2 + z^2}. \tag{A5.3}$$

The volume integration Eq. (A5.2) over surface 1 is therefore

$$u = \rho_1 \int_{S1} U_{L-J}(s)\,dS1 = 4\tilde{e}\rho_1 \int_{S1}\left[\left(\frac{\varepsilon_0}{s}\right)^{12} - \left(\frac{\varepsilon_0}{s}\right)^{6}\right]dS1$$

$$= 4\tilde{e}\rho_1 \int_{-\pi/2}^{\pi/2} d\theta \int_{h}^{+\infty}\left[\left(\frac{\varepsilon_0}{s}\right)^{12} - \left(\frac{\varepsilon_0}{s}\right)^{6}\right]sd$$

$$= 8\pi\tilde{e}\rho_1 \int_{h}^{+\infty} dz \int_{0}^{1}\left[\left(\frac{\varepsilon_0}{\sqrt{x^2+z^2}}\right)^{12} - \left(\frac{\varepsilon_0}{\sqrt{x^2+z^2}}\right)^{6}\right]x\,dx$$

$$= 8\pi\tilde{e}\rho_1 \varepsilon_0^{12} \int_{h}^{+\infty} \frac{dz}{10z^{10}} - 8\tilde{e}\rho_1 \varepsilon_0^{6} \int_{h}^{+\infty} \frac{dz}{4z^{4}}$$

$$= -\frac{8\pi\tilde{e}\varepsilon_0^{12}\rho_1}{90h^9} + \frac{8\pi\tilde{e}\varepsilon_0^{6}\rho_1}{12h^3}. \tag{A5.4}$$

Integrating u over surface 2 will obtain the specific surface energy produced by the two surfaces that

$$U = \rho_2 \int_{S2} u\,dS2 = \rho_2 \int_{S2}\left(-\frac{8\pi\tilde{e}\varepsilon_0^{12}\rho_1}{90h^9} + \frac{8\pi\tilde{e}\varepsilon_0^{6}\rho_1}{12h^3}\right)dS2$$

$$= \rho_2 \int_{-\infty}^{0} dz \int_{0}^{1}\left(-\frac{8\pi\tilde{e}\varepsilon_0^{12}\rho_1}{90h^9} + \frac{8\pi\tilde{e}\varepsilon_0^{6}\rho_1}{12h^3}\right)dx = -\frac{8\pi\tilde{e}\varepsilon_0^{12}\rho_1\rho_2}{720h^8} + \frac{8\pi\tilde{e}\varepsilon_0^{6}\rho_1\rho_2}{24h^2} \tag{A5.5}$$

where ρ_2 is the number of atoms in the domain $S2$ per unit volume. The adhesive surface traction between two planar surfaces σ_a is the spatial derivative of the specific surface energy such that

$$\sigma_a = \frac{\partial U}{\partial h} = \partial\left(-\frac{8\pi\tilde{e}\varepsilon_0^{12}\rho_1\rho_2}{720h^8} + \frac{8\pi\tilde{e}\varepsilon_0^{6}\rho_1\rho_2}{24h^2}\right)/\partial h$$

$$= \frac{8\pi\tilde{e}\varepsilon_0^{12}\rho_1\rho_2}{90h^9} - \frac{8\pi\tilde{e}\varepsilon_0^{6}\rho_1\rho_2}{12h^3}. \tag{A5.6}$$

Introducing the Hamaker constant

$$H_A = 4\tilde{e}\varepsilon_0{}^6 \pi^2 \rho_1 \rho_2 .$$
(A5.7)

in Eq. (A5.6) gives

$$\sigma_a = \frac{8\pi\tilde{e}\varepsilon_0{}^{12}\rho_1\rho_2}{90h^9} - \frac{8\pi\tilde{e}\varepsilon_0{}^6\rho_1\rho_2}{12h^3} = \frac{2H_A\varepsilon_0{}^6}{90\pi h^9} - \frac{2H_A}{12\pi h^3} = \frac{H_A(2/15)\varepsilon_0{}^6}{6\pi h^9} - \frac{H_A}{6\pi h^3} .$$
(A5.8)

Introducing $\varepsilon_1 = (2/15)^{1/6}\varepsilon_0$ which is Eq. (5.29), the adhesive surface traction σ_a in Eq. (A5.8) becomes

$$\sigma_a = \frac{H_A(2/15)\varepsilon_0{}^6}{6\pi h^9} - \frac{H_A}{6\pi h^3} = \frac{H_A}{6\pi h^3}\left[\left(\frac{\varepsilon_1}{h}\right)^6 - 1\right].$$
(A5.9)

The specific surface energy can be represented by the Harmaker constant that

$$\gamma = \frac{H_A}{16\pi\varepsilon_1^2} .$$
(A5.10)

Substituting Eq. (A5.10) into Eq. (A5.9), the adhesive surface traction between two planar surfaces is

$$\sigma_a = -\frac{8\gamma}{3\varepsilon_1}\left[\left(\frac{\varepsilon_1}{h}\right)^3 - \left(\frac{\varepsilon_1}{h}\right)^9\right] ,$$
(A5.11)

which is Eq. (5.30).